MONTANUNIVERSITÄT LEOBEN

PhD Thesis

Advanced Nanoindentation Techniques for the Extraction of Material Flow Curves

Alexander LEITNER

This work was financially supported by the Styrian and the Tyrolean Provincial Government, represented by Steirische Wirtschaftsförderungsgesellschaft mbH and Standortagentur Tirol, within the framework of the COMET Funding Programme (837900, MPPE A7.19).

Department of Materials Physics

Montanuniversität Leoben

Jahnstraße 12

8700 Leoben, Austria

Affidavit

I declare in lieu of oath, that I wrote this thesis and performed the associated research myself, using only literature cited in this volume.

Leoben, November 2017 Alexander LEITNER

Danksagung

Der Entschluss eine Doktorarbeit zu schreiben lässt anfänglich noch nicht erahnen, welche Herausforderungen diese Zeit bergen werden. Diese wären ohne Zweifel nicht alleine zu bewältigen, daher sei hier an erster Stelle meinem Doktorvater Assoz. Prof. Dr. Daniel Kiener gedankt. Die weitgehend reibungslose Durchführung des Projektes, in Zuge dessen diese Arbeit entstand, ist zu einem großen Teil seiner weitsichtigen und gut durchdachten Planung geschuldet. Ein großes Dankeschön gilt auch Verena Maier-Kiener, meiner Anlaufstelle Nr. 1 bei allen technischen Belangen des Nanoindentierens. Abgesehen von den zahlreichen produktiven Diskussionen hinsichtlich wissenschaftlicher Themen und Arbeitsweisen, möchte ich mich auch für die Flexibilität und das nette Beisammensein abseits der Arbeit bedanken.

Meinen Gruppen- und Bürokollegen Markus Alfreider, Reinhard Fritz, Ruth Konetschnik, Jinming Guo, Pradipta Ghosh, Karoline Kormout, Manuel Pfeifenberger & Michael Reisinger möchte ich für die zahlreichen vielseitigen und lustigen Unterhaltungen über Gott und die Welt danken. Danke an Andreas Kleinbichler und Megan J. Cordill für die Unterstützung am LEXT.

Ein Dankeschön gilt Silke Modritsch für die perfekten Probenpräparationen, Peter Kutlesa für die Hilfe mit den HPT Proben. Danke an Franz Hubner und Robin Neubauer für die Umsetzung meiner technischen Zeichnung. Danke auch an Sabine Wilfling und Daniela Brunner für die vielen Erledigung im administrativen Bereich.

Der gesamten ESI-Belegschaft möchte ich auch noch für die zahlreichen lustigen Abende in der Werkstatt danken, die immer wieder für eine willkommene Abwechslung sorgten.

Ein großes Dankeschön geht an meinen Freundeskreis, vor allem an meine Kommilitonen die mich seit Studienbeginn begleiten und unentwegt für „kreative“ Diskussionen zur Verfügung stehen: Raphael Esterl, Manuel Gruber, Thomas Kaltenbrunner, Manuel Petersmann, Josef Pörnbacher & Markus Tauscher.

An dieser Stelle möchte ich auch meiner ganzen Familie für den Rückhalt und ihre grenzenlose Unterstützung in jeder Hinsicht danken, ohne diese die Arbeit in dieser Form zweifelsohne nicht geschafft hätte.

Nicht zuletzt möchte ich mich bei meiner Frau Kathrin bedanken, für das schier unermüdliche Vermögen mich zu motivieren und hundertprozentigen Verlässlichkeit in allen Lebenslagen. Ebenso möchte ich meiner Tochter Anna Katharina danken, dein Anblick lässt so manche Sorgen in Vergessenheit geraten. Außerdem bot sie mir die einzigartige Gelegenheit auch regelmäßig nachts über meine Arbeit nachzudenken.

Kurzfassung

Seit Jahrzehnten suchen Materialwissenschafter nach einer effizienten Testmethode zur umfangreichen mechanischen Charakterisierung von Werkstoffen auf kleinster Ebene, anwendbar für einen breiten Temperaturbereich. Nanoindentierung hat das Potential diesen Anforderungen gerecht zu werden, multiaxiale Spannungs- und Dehnungszustände während der Prüfung erschweren aber den direkten Vergleich zu uniaxialen Tests.

Am Beispiel von nanoporösem Gold wird anfänglich gezeigt, dass moderne Nanoindentierungsmethoden die Bestimmung von thermo-mechanischen Eigenschaften auf Proben im Labormaßstab ermöglicht. Der untersuchte Schaum zeigt dabei eine durch Glühen verursachte Aufhärtung und weist Grenzflächen/Versetzungswechselwirkungen als dominierenden Verformungsmechanismus auf. Immer öfter kommen dynamische Indentierungsmethoden zum Einsatz, die einerseits die Datendichte erhöhen, andererseits aber zu abweichenden Härtewerten im Vergleich zu statischen Prüfprotokollen aufweisen können. Dieser Unterschied konnte im Zuge dieser Arbeit mit dem Haltesegment bei Maximalkraft in statischen Tests in Verbindung gebracht werden. Die drastische Verringerung der Dehnrate äußert sich bei ratensensitiven Materialen durch eine sinkende Härte. Der mittlere Fehler konnte durch die Einführung eines physikalischen Modells auf durchschnittlich 2.5% reduziert werden.

Unter Rücksichtnahme dieses Effekts und durch Verwendung von Indenterspitzen mit verschiedenen Öffnungswinkeln können dehnungsabhängige Charakteristiken von Materialien ermittelt werden. Untersuchungen auf W und Ni Proben mit verschiedenen Mikrostrukturen erlaubten die Bestimmung von Hall-Petch Parametern. Nach Berücksichtigung von Größeneffekten und einer Umrechnung von Härte zu mechanischer Spannung können letztendlich Fließkurven der untersuchten Materialien gewonnen werden.

Zur Erhöhung der lokalen Auflösung können Indenterspitzen mit sphärischer und damit nicht-selbstähnlicher Geometrie verwendet werden. Die Herstellung solcher Spitzen ist problematisch, daher muss eine präzise Kalibrierung sichergestellt werden. Innerhalb dieser Arbeit wurde eine neue Kalibrierungsmethode entwickelt, die in Kombination mit Versuchen bei konstanten Dehnraten den Grundstein für die Ermittlung eines material- und dehnungsabhängigen Umrechnungsfaktors zwischen Härte und Spannung ermöglicht. Nach Anwendung der erwähnten Verbesserungen konnten Fließkurven von kubisch-flächenzentrierten (Cu, Ni) und kubisch-raumzentrierten (W, Cr) Metallen gemessen werden, die durch Mikrodruckversuche derselben Proben verifiziert wurden.

Die vorliegende Arbeit trägt wesentlich dazu bei bestehende Testprotokolle zu erweitern, um einen wichtigen Schritt in Richtung Implementierung von Nanoindentierung als Standardmethode zur Bestimmung von Fließkurven zu setzen.

Abstract

For decades material scientists long for an efficient testing tool to characterize materials with respect to mechanical, but also rate-dependent properties and the possibility to conduct experiments in a broad temperature range. Nanoindentation turns out to meet these demands, but there remain uncertainties in the analysis, especially in the comparability to uniaxial data.

On the example of nanoporous Au, it is demonstrated that modern nanoindentation approaches allow to comprehensively characterize the thermo-mechanical behavior of bench scale materials. The examined foam exhibits a distinct hardening-by-annealing behavior and dislocation/interface interactions as dominating deformation mechanism in the tested temperature range from ambient temperatures to 300 °C. This is followed by investigations of the impact of dynamic measurement methods on the obtained mechanical properties. Thereby it is verified that differences in hardness between static and dynamic testing protocols mainly originate from strain-rate discrepancies owed to the hold segment used in static tests. Identification of this effect allowed to introduce a predictive model which reduces the error from up to 17% down to an average of 2.5%.

Accounting for this effect allows to subsequently exploit sharp tip nanoindentation by using four tips with varying apex angle equivalent to different representative strains. Testing various Ni and W samples with microstructures ranging from single crystalline to nanocrystalline enables to compare nanoindentation to Vickers hardness tests and to identify Hall-Petch parameters in dependence of the strain. Finally, flow curves are constructed using the obtained modulus and by converting hardness to equivalent stresses. Uniaxial literature data are in good accordance with obtained numbers if the indentation size effect is considered adequately.

To further increase the local resolution and to maximize the output, finally spherical tip geometries are thoroughly investigated as this geometry combined with dynamic measurement techniques enables the extraction of flow curves from individual impressions. Improved calibrations of tips based on spherical geometries and the introduction of strain-rate controlled tests enable a reliable determination of the conversion factor between hardness and stress. The accuracy of the material dependent constraint factor verified on body-centered cubic (W, Cr) and face-centered cubic materials (Cu, Ni) with refined microstructures.

The present thesis closely investigates modern nanoindentation approaches to identify restrictions and required parameters necessary for the comparison with other testing techniques. Occurrent challenges in terms of flow curve extraction are faced by novel advancements and moves the technique on step further towards its feasibility to extract material flow curves.

Contents

CHAPTER 2

Abbreviations

$\dot{h}$	Time-derivative of displacement
$\dot{H}$	Time-derivative of hardness
$\dot{P}$	Time-derivative of load
$\dot{\varepsilon}$	Strain-rate
ε_r	Representative strain
ε_u	Uniaxial strain
σ_r	Representative stress
a_c	Contact radius
A_c	Contact area
aR	As received
b	Burgers vector
B	Fitting parameter for area function
c	Plastic zone size
C^*	Constraint factor
cBN	Cubic boron nitride
CG	Coarse grained
CSM	Continuous stiffness measurement
cSR	Constant strain-rate
E	Young's modulus
E^*	Reduced modulus
EBSD	Electron backscatter diffraction
ED	Electrodeposition
FEM	Finite element method
FG	Fine grained
FIB	Focused Ion Beam
GS	Grain size
H	Hardness
$H_{0,HP}$	Hardness in the absence of grain-boundaries
h_c	Contact displacement
HP	Hall-Petch
HPT	High pressure torsion
h_s	Sink-in displacement
HT	High temperature
ISE	Indentation size effect
k_B	Boltzmann constant
$k_{H,HP}$	Material dependent Hall-Petch parameter for hardness
m	Strain-rate sensitivity
N	Number of HPT rotations
NC	Nanocrystalline
n_L	Loading slope
NP	Nanoporous
P	Load
r	Radial position on HPT disk
R_{eff}	Effective radius
R_{spec}	Specified radius
RT	Room temperature
S	Contact stiffness
SEM	Scanning electron microscope
SPD	Severe plastic deformation
SRJ	Strain-rate jump tests
SX	Single crystalline
t	HPT disk thickness
T_a	Absolute temperature
V^*	Activation volume
α	Half apex angle of the representative cone
β	Geometry constant
γ	Shear strain
ϵ	Geometry constant
θ	Strain-decisive opening angle
ν	Poisson's ratio
σ_y	Yield stress

CHAPTER 1

1. Motivation

Nowadays, the repertoire of experimental techniques for the mechanical characterization of materials has reached an unprecedented level. Instrumented indentation is highly competitive among materials testing methods due to its outstanding features in terms of precision, automation and versatility. The number of accessible mechanical and material-physical properties rose surpassingly in the past decades, still the enormous potential is far from exhausted. Beside the conventional determination of a sample's hardness H and Young's modulus E, present-day nanoindentation methods allow to draw conclusions about dominating deformation mechanisms, tribological properties, interface strengths or defect distributions accompanied by an eminent local resolution at a nanometer scale, thereby only consuming minimal sample volumes. Moreover, all properties are potentially obtainable at low, room (RT) and high temperatures (HT).

However, the rapid development in the past years, including the deployment of dynamic techniques and various tip shapes, left behind open questions and uncertainties. The impact of a superimposed marginal oscillating force, used for a continuous determination of the material's stiffness, on the obtained hardness has frequently been a matter of debate. Interestingly, the effect is noticeable at shallow depths, where the resulting displacement amplitude is significant compared to the total indentation depth, but also at large displacements. Furthermore, the hardness deviation in comparison to static tests is explicitly material-specific.

Understanding and considering this effect opens the opportunity to extract mechanical flow curves from nanoindentation experiments. In principle, the possible approaches can be classified in testing protocols with self-similar indenter tips, such as pyramids or cones, and tests with non-self-similar tip geometries, such as spheres. Both have been in the center of attention of the small-scale testing community in the past years, still comprehensive experimental studies on model-materials are lacking in literature. Even though the use of sharp tips allows a comparison to conventional Vickers hardness testing, follows a straightforward analysis and enables accounting for size-effects, only discrete points on a stress-strain curve can be obtained. Spherical tips can conceptionally deliver continuous flow curves, but are critical in terms of tip imperfections, strain-rate effects and the challenging conversion from hardness to a representative strain in the elastic-plastic regime.

Hence, following gaps in the knowledge of indentation experiments are identified:

I. Explanation of hardness differences between static and dynamic nanoindentation techniques
II. Comprehensive experimental studies on the applicability of a multiple sharp tip approach
III. Adequate calibration procedures for spherical tips
IV. Deriving strain-rate controlled test protocols for non-self-similar tip geometries
V. Conversion of hardness to representative stress in elastic-plastic deformation regimes

2. Aim of the thesis

The focus of the present work is the extraction of mechanical flow curves by utilizing instrumented nanoindentation. At first, the study will get to the bottom of discrepancies occurring between static and dynamic nanoindentation experiments. Understanding the role of indentation strain-rate in this respect will allow to predict hardness differences and consequently enable physically defined experiments. This will be decisive to develop the technique one step further towards its implementation as an equivalent alternative to conventional uniaxial tests for the extraction of stress-strain curves. For this purpose, comprehensive investigations of sharp and spherical tip approaches on a broad range of materials with different crystal systems and microstructures will be subject of experimental studies. Utilizing sharp tips will additionally shed light on the comparability of nanoindentation and classical Vickers hardness tests as well as on the feasibility to obtain Hall-Petch (HP) parameters for Ni and W in dependence of the indentation strain or the tip opening angle, respectively. In addition, essential refinements of spherical tip calibrations and strain-rate controlled experiments will be introduced, the usability of which will be substantiated by comparison to Berkovich reference measurements and literature data. Finally, spherical indentation flow curves will be bridged to uniaxial stress-strain curves by linking the conversion factor of hardness and representative stress to the dimensionless parameter of contact loading versus unloading slope sustained from indentation load-displacement curves. Examined materials with small internal length scales finally shall demonstrate the feasibility of nanoindentation as a technique for a thorough mechanical characterization of modern micro- and nanostructured materials.

3. Retrospect

Hardness is one of the eldest parameters to mechanically characterize materials, as it is highly intuitive that harder materials can penetrate softer materials but not vice versa. All the same, there is hardly any other mechanical property which definition is as physically controversial. Owed to the long history of hardness testing, fundamentally different may hide characteristics behind the term “hardness”.

The provable documented of systematic hardness testing goes far back in time, starting in the age of reason. In 1722 natural scientist René-Antoine Ferchault de Réaumur introduced a scratch test by utilizing a quenched steel bar with a hardness gradient [1]. The bar was scratched with the specimens to be investigated. The position where the scratch could not be identified anymore was used to deduce the sample’s hardness. For an entire century, no noteworthy developments emerged until the Austrian-German mineralogist Friedrich Mohs established a relative hardness scale by determining whether a mineral can scratch another or not [2]. This resulted in a ten-grade hardness scale referring to talcum with the lowest hardness of 1 Mohs and diamond as the hardest material (10 Mohs). During the advancing industrial revolution, the demand of material testing techniques vastly increased and pushed the development of hardness tests.

First reported attempts of point-indentation tests are ascribed to Johnson and Calvert in 1859 [3] who also determined a relative hardness scale and already stated that a testing protocol which obtains an absolute number for a material’s hardness would be vital for the global success of hardness testing. Martens finally defined the hardness as the maximum load of an indentation experiment divided by surface area of the residual imprint created by a sphere [4], which was also adopted by the Swedish engineer Brinell whose experimental concept is still used nowadays [5]. In the war-torn world of the first half of the 20th century evolution of military armament, especially aeronautics, contributed to a recurring interest of various hardness testing techniques. Rockwell firstly used the indentation depth as a parameter for hardness and accounted for elastic deformation with a pre-loading sequence [6]. The Vickers method uses a quadratic pyramidal diamond tip and hence differs from the Brinell hardness as the deformation is induced by a self-similar tip geometry [7]. Step by step scientist started to deal with the characterization of the stress and strain field under a loaded indenter, trying to link H to mechanical properties such as yield stress or Young’s modulus. Hertz’s contact mechanics lay the foundation for elastic contact problems [8], while Prandtl committed his work to analytic solutions using slip-line theory of plastic deformation introduced by conical tips [9].

After one of the most extensive and outstanding studies on the hardness of metals by Tabor in 1951 [10], the advancements, modifications and knowledge of hardness testing became too comprehensive to be entirely addressed within this thesis. Only developments substantial for the focus of this work will be covered in the following sections. However, further details of the historical development of indentation testing are given in an excellent review by Walley [11].

4. State-of-the-art nanoindentation

Common hardness testing in all its facets is common practice in almost any quality testing lab for conventional materials. Most of them still rely on the measurement principles derived in the early 20th century and are primarily used for qualitative comparison. Hardness values of those techniques are only restrictively comparable among each other. However, instrumented indentation provides the opportunity to conduct physically defined experiments which allow to separate the mechanical characteristics in plastic and elastic regimes. Following sections will clarify the significance and progresses in hardness testing achieved by nanoindentation.

4.1. Conventional nanoindentation analysis

Generally, the hardness and Young's modulus, determined following the analysis introduced by Oliver and Pharr [12], is the usual output of standard nanoindentations routines. Fundamentals shall briefly be outlined at this point, for details the reader is referred to references [12–14]. Three parameters can be obtained from the load-displacement output to calculate H and the reduced modulus E*: the maximum load P_{max}, the maximum displacement h_{max} and the contact stiffness S at the point of unloading (=h_{max}). Using these parameters, the elastic recovery h_s around an impression can be assessed and separated from the total displacement to obtain the contact depth h_c (see Figure 1):

$$h_c = h_{max} - h_s = h_{max} - \epsilon \cdot \frac{P_{max}}{S} \qquad \text{equation (I)}$$

with ϵ as a geometrical factor with a value of 0.75 for Berkovich and spherical tips.

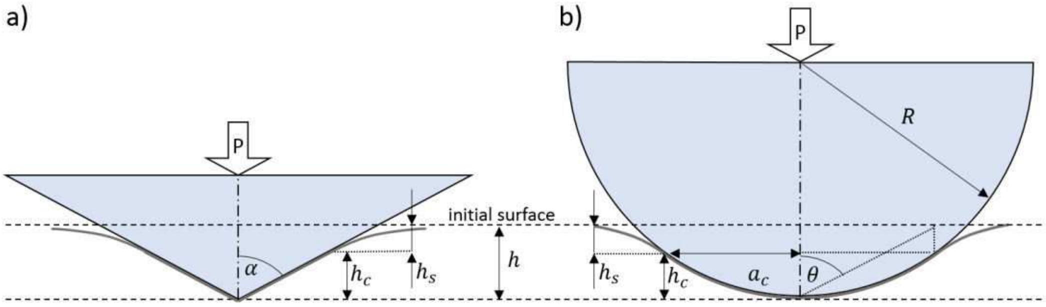

Figure 1. Schematic showing loaded indenter tips and occurring elastic deformation around the imprint for a) sharp and b) spherical indenter geometries.

The contact area A_c in dependence of h_c can be obtained from calibration measurements on an elastic isotropic sample, conventionally fused quartz (E=72 GPa). For sharp tips, a series expansion is used, with B_i as fitting parameters [12], while for spherical tips the specified radius R_{spec} or effective radius R_{eff} can be used [10,15–17]:

$$A_c(h_c) = \sum_{i=0}^{i} B_i \cdot h_c^{1/2^{i-1}} \qquad \text{equation (II)}$$

$$A_c(h_c) = \pi \cdot h_c \cdot \left(2 \cdot R_{spec\,(eff)} - h_c\right) \qquad \text{equation (III)}$$

Ultimately, H and the E* can be obtained by [12,18,19]:

$$H(h_c) = \frac{P_{max}}{A_c(h_c)} \qquad \text{equation (IV)}$$

$$E^*(h_c) = \frac{\sqrt{\pi}}{2 \cdot \beta} \cdot \frac{S}{\sqrt{A_c(h_c)}} \qquad \text{equation (V)}$$

with β=1 for spherical and pyramidal tips.

4.1.1 Dynamic nanoindentation testing

In fact, for static tests the mechanical properties can only be obtained at the point of unloading since the stiffness is dependent of the displacement itself which is in turn required for equation (I) (see Figure 2a). Two approaches can be used to increase the data output. Quasi-static experiments with multiple unloading segments (Figure 2b) or the use of a superimposed sinusoidal force signal with marginal amplitude, sometimes referred to as continuous stiffness measurement (CSM) technique (Figure 2c). The latter one facilitates a maximum exploitation of data. Additionally, hold segments required for static and quasi-static tests can be avoided. For CSM tests, the phase shift between load and resulting displacement amplitude allows to assess the harmonic contact stiffness during the test [12,20–24] instead of determining the slope of unloading curves. Several studies dealt with the impact of CSM parameters such as frequency or amplitude [24–30]. A frequency of 45 Hz and displacement amplitude of 2 nm are recommended to minimize discrepancies originating from the integrated lock-in amplifier for materials with high values of E/H [31]. Still, for shallow indents, where the amplitude is significant compared to the actual displacement, there is a controversial debate whether the force oscillation influences the determined mechanical properties [27,29,30]. This problem is irrelevant for the present work as the analysis is performed in regimes where this effect diminishes. However, for some materials substantial hardness differences can be noted at large displacements. This behavior will be addressed in Publication C.

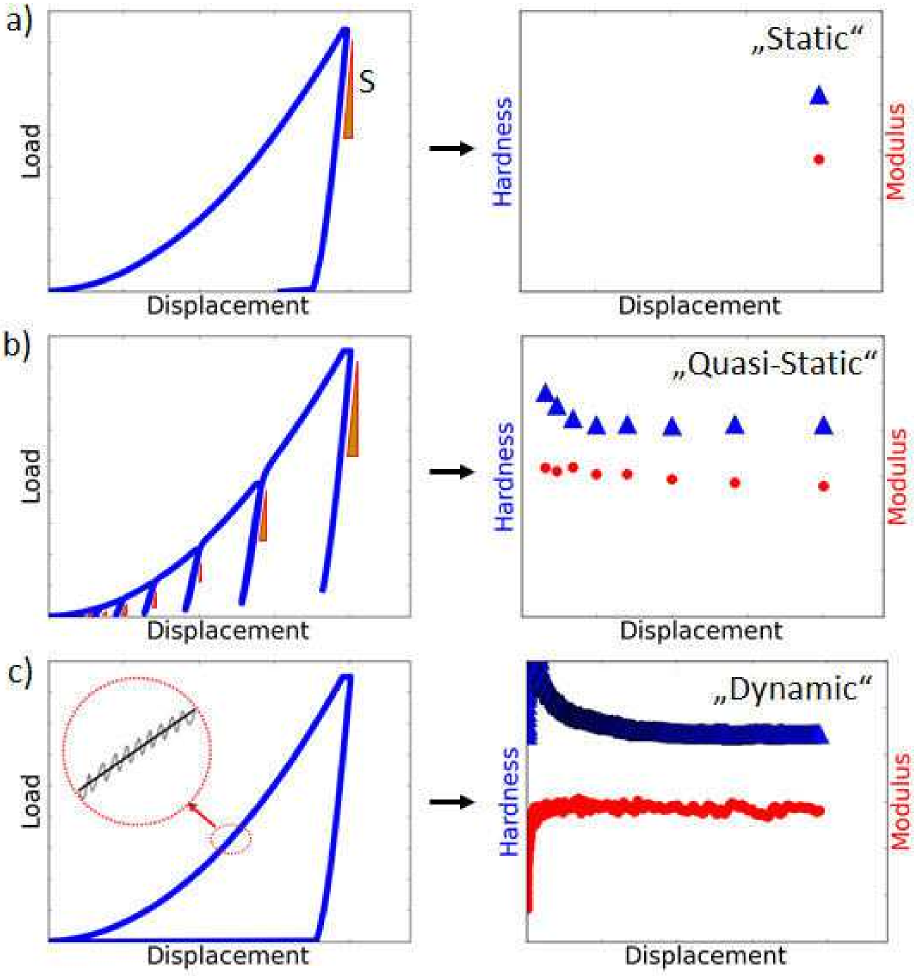

Figure 2. Schematic indentation load-displacement curves with obtainable depth-dependent mechanical properties for a) static, b) quasi-static and c) dynamic testing mode.

4.1.2 Pile-up and sink-in

Indentation of a material induces high stresses and strains. In dependence of the mechanical properties such as H, E, the work hardening exponent n and the induced strain, this causes effects such as a material pile-up or a sink-in at the edges of the residual impression [13,32–34]. Indeed, there is no guarantee that a pile-up proportionally carries the load as there is laterally no supporting bulk material behind. Nevertheless, the influence can be assessed by examining the depth profile of the Young's modulus. For dynamic indentation tests and elastic isotropic materials, this must be a horizontal line and comply with the theoretic bulk modulus. If this is the case, the effect of pile-up and sink-in can be considered negligible. Hence, profiles of E will be used within this study to validate conducted measurements.

4.1.3 Consideration of tested volumes

In general, an additional experimental parameter comes into play for small-scale tests since the sampled volumes may not correspond to a representative volume. In terms of nanoindentation, size effects for materials with comparably large internal length scales occur which are attributed to strain-gradients at low depths, where the generation of geometric necessary dislocations is decisive [35,36]. For materials with few defects, stresses close to the theoretical strength are measured if the tested volume does not contain any flaws. This is likely the case for many materials under shallow indents as the tested volume is considerably small. Once the extending stress-field can activate a dislocation source, the stress level drops to lower levels, marked by a rapid pop-in event [37].

Certainly, testing of representative volumes is a prerequisite for the extraction of reliable flow curves. Thus, either samples with small microstructural dimensions, such as nanocrystalline (NC, grain-size (GS) <100 nm) or ultra-fine grained (UFG, GS < 1 µm) will be used throughout this study, or appropriate extrapolations will be used to ensure correct data [35,38].

4.2. Tip geometries

The geometric character of the indenter tip plays an essential role for the interpretation of nanoindentation results. Typically, self-similar tip geometries are used for conventional instrumented indentation tests, such as pyramidal tips. As visualized in Figure 3a, self-similarity is given if the proportions of an observed shape do not depend on the magnification, represented by two spectators with equal angle of sight at different positions. This is not the case for a spherical shape as the curvature of the magnified contour changes, see Figure 3b. Consequences of this fact will be discussed in the following section.

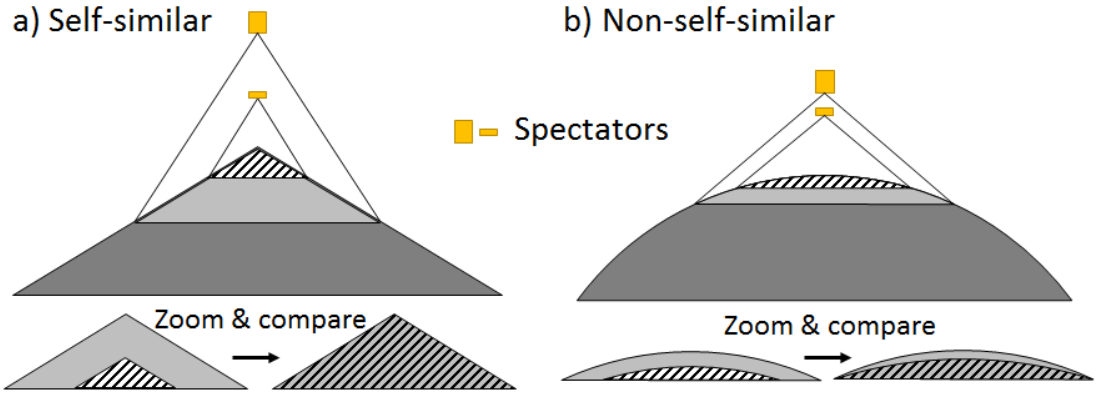

Figure 3. Comparison of shapes obtained by two different spectators synonymous with two different magnifications. While self-similar shapes in a) represent themselves once the shape is proportionally magnified, this is not the case for non-self-similar geometries in b).

4.2.1 Self-similar indenter tip geometries

Pyramidal tip shapes implicate several assets. On the one hand, the manufacturing of three-sided sharp tips is favorable since three faces will necessarily lead to a sharp top and tolerances of the opening angle comply precisely with specifications. On the other hand, the self-similarity imparts on the emerging stress and strain fields under the indenter tip, thus keeping the measured properties independent of the displacement for isotropic samples. This simplifies the analysis of indentation related effects, such as the indentation size effect (ISE) [35]. It is feasible to implement a mechanistic model, as suggested by Nix and Gao for sharp tips [35], which is far more challenging for spherical tips [39,40].

However, the asset of self-similarity may also be considered as a drawback since the induced representative strain cannot be varied with a single tip. This complicates the definition of a strain-rate which can be interpreted as speed of the continuous extension of the plastic zone, rather than the increase of the representative strain ε_r itself. For self-similar pyramidal tips, the indentation strain-rate $\dot{\varepsilon}$ is defined as [41]:

$$\dot{\varepsilon} = \frac{\dot{h}}{h} = \frac{1}{2} \cdot \left(\frac{\dot{P}}{P} - \frac{\dot{H}}{H} \right) \approx \frac{1}{2} \cdot \frac{\dot{P}}{P} \qquad \text{equation (VI)}$$

where $\dot{P}, \dot{H}$ and $\dot{h}$ are time derivatives of the load, hardness and displacement, respectively. ε_r is empirically defined using the half apex angle α of the representative cone of a tip (see Figure 1a), while linear relationship between representative stress σ_r and H was proposed by Tabor with the constraint factor C* as the linking parameter [10]:

$$\varepsilon_r = 0.2 \cdot cot\, \alpha \qquad \text{equation (VII)}$$

$$H(\varepsilon_r) = C^* \cdot \sigma_r(\varepsilon_r) \qquad \text{equation (VIII)}$$

The value of C* has been subject of numerous studies and is still controversially discussed [10,32,38,42–47], for which reason this will be part of the investigations in Publication B and Publication D.

4.2.1.1 Identification of thermally activated deformation mechanisms

Recent developments have significantly extended the number of material properties that can be extracted by nanoindentation techniques. Determination of the strain-rate sensitivity m and the activation volume V* enables to indicate the dominating thermally activated deformation mechanisms. These parameters can be evaluated if H is known for various strain-rates and by considering the absolute temperature T_a and the Boltzmann constant k_B, respectively:

$$m = \frac{d\, ln\, H}{d\, ln\, \dot{\varepsilon}} \qquad \text{equation (IX)}$$

$$V^* = \frac{\sqrt{3} \cdot k_B \cdot T_a \cdot C^*}{m \cdot H} \qquad \text{equation (X)}$$

Mainly two approaches are used for this purpose. On the one hand, strain-rate jump tests (SRJ), where $\dot{\varepsilon}$ abruptly changes after the set displacement limit is reached (Figure 4a) [48]. This has the advantage that the strain-rate levels can be set as an input parameter. On the other hand, the hold segment at maximum load and the related relaxation behavior can be utilized to extract H and $\dot{\varepsilon}$ data pairs for the examination of m and V*, respectively (Figure 4b) [49,50]. The asset of this approach is that tests can be conducted at low displacements, but with the drawback that the resultant $\dot{\varepsilon}$ will be material-specific. Both methods have been used within the present work, details can be obtained in Publication A, C, E, F & G.

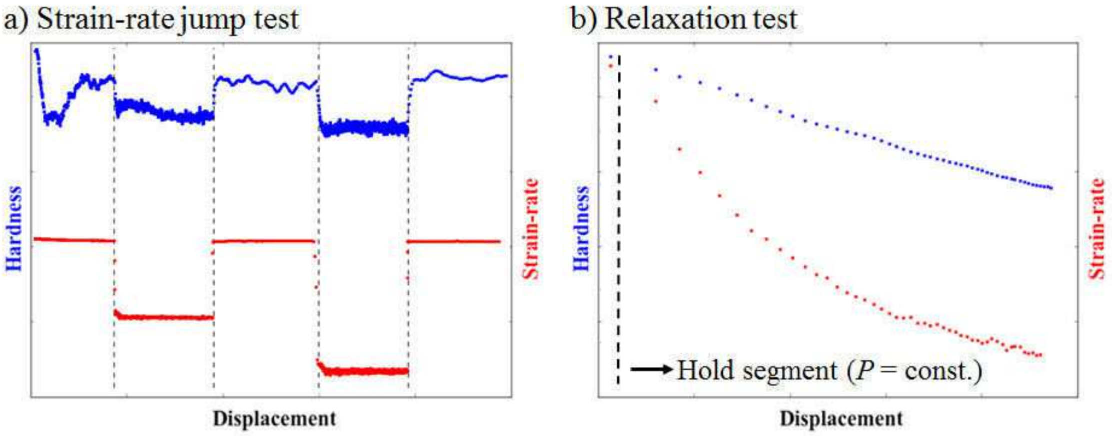

Figure 4. Hardness and strain-rate profiles for a) SRJ and b) relaxation tests used to determine governing thermally activated deformation mechanisms. In b) only the evolution of H and $\dot{\varepsilon}$ in the hold regime of the test is displayed.

4.2.1.2 Comparability of hardness tests

Even though Vickers and nanoindentation Berkovich tests use self-similar pyramidal tips with the same representative cone-angle, the obtained hardness values are not directly convertible [51]. While Vickers tests use the area in contact with the tip geometry, ending up in four pyramidal faces, in instrumented indentation the projected area is used to calculate the mean pressure. By geometrical considerations this difference can be overcome by multiplying the Vickers hardness with a constant of 1.08. Still, a difference remains which originates from the fact that nanoindentation H is determined at the point of maximum load and considers the elastic response of the material. For Vickers hardness tests, this information is lost as the dimensions of the residual indent after unloading do not allow to deduce any elastic behavior. Figure 5 displays uncorrected H-values obtained by Vickers microhardness tests and reference nanoindentation measurements for Ni and W with decreasing grains size from single crystalline (SX) to nanocrystalline (NC) regimes. It is evident, that the differences in H increase with decreasing ratio of E/H, as the elastic deformation becomes more decisive. Correction procedures which facilitates direct comparison between Vickers and Hardness values will be discussed in Publication B.

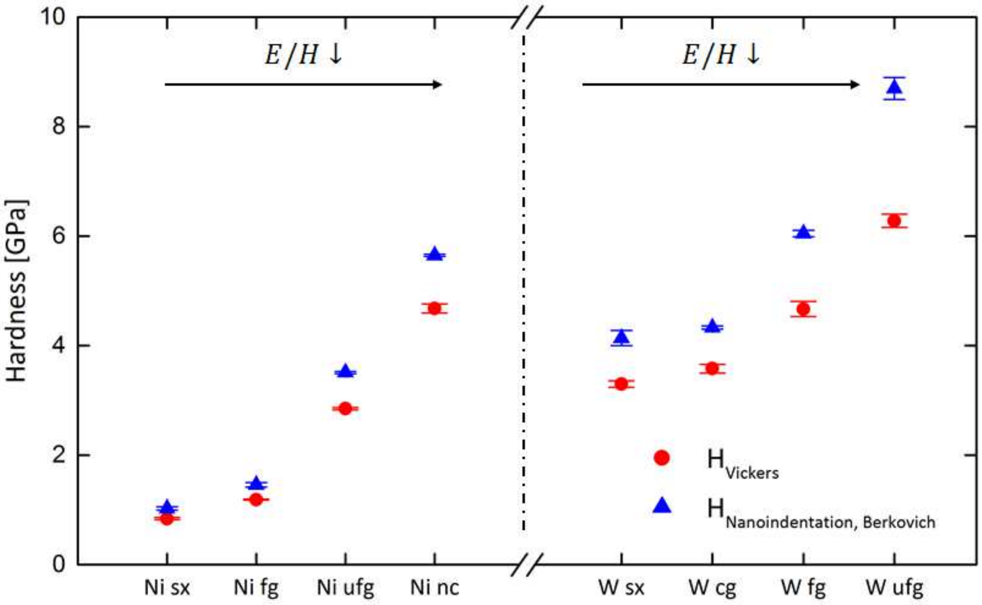

Figure 5. Direct comparison of Vickers and nanoindentation measurements on Ni and W samples with varying microstructure show that with decreasing E/H values differences become more pronounced.

4.3. Non-self-similar indenter tip geometries

Usage of spherical tips opens new possibilities. Unlike self-similar tips, not only discrete points on a flow curve will be available, but a continuous increase of ε_r with increasing displacement will enable to obtain stress-strain curves as in conventional uniaxial tests. This is a highly appealing concept, but various challenges must be faced to succeed which kept research groups busy for decades. Essential aspects that impede a straight-forward analysis will be discussed in the following sections.

4.3.1 Tip shape imperfections

A main reason why the spherical indentation technique is not yet used as a standard testing method is owed to the complexity of tip manufacturing. The material selection is extremely limited for indentation tips since they should be as hard and as stiff as possible to avoid influences of tip deformations. This tremendously reduces the choice of potential candidates and leaves mainly anisotropic materials with strong chemical bonds such as diamond, sapphire, tungsten carbide (WC) or cubic boron nitride (cBN). Thus, the fabrication of precise rotationally symmetric bodies, such as spheres, is restricted by the elastic anisotropy. Investigations of available tips clearly show imperfections [17]. An example is illustrated in Figure 6a showing the topography of a spherical tip with $R_{spec} = 10$ µm, obtained by a confocal laser microscope (Olympus LEXT OLS4100, Tokyo, Japan), while Figure 6b shows a scanning electron microscope (SEM) image of a residual imprint with notable imperfections. Clearly, the calibration of the area function according to equation (III) is considerably affected if the shape is not representing a sphere, alike the obtained mechanical properties. As it is improbable that the fabrication of spherical tips will achieved the required precision while maintaining reasonable prices on near term, Publication D will deal with alternative solutions on tip calibrations and data analysis.

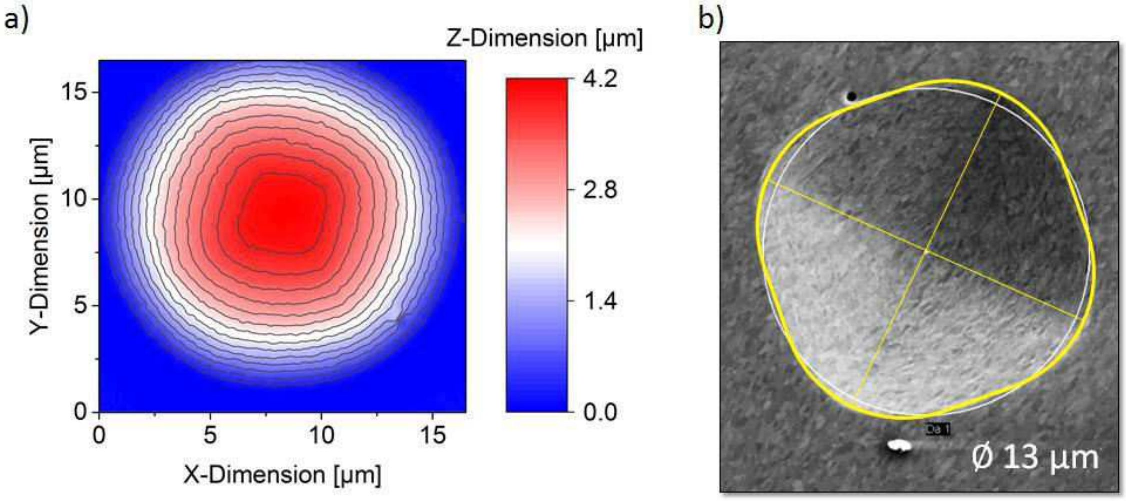

Figure 6. a) 3D profile of a spherical tip (R_{spec}=10 µm) obtained by a confocal laser microscope. b) SEM micrograph of a residual impression on UFG Cr shows the imperfect features of the tip

4.3.2 Representative stress and strain

The complex multiaxial stress-field underneath an indenter tip makes the definitions of representative stress and strain difficult. For a uniaxial test the stress-field is uniform and thus independent of the considered volume increment (Figure 7a). Hence, there is no need to estimate an equivalent stress. On the other hand, the mismatch between H and σ_r in spherical indentation tests (Figure 7b) mainly stems from the fact that only the deviatoric components of the stress-tensor will contribute to plastic deformation. Thus, highly hydrostatic conditions during indentation must be accounted for. Also, the conversion of the 3D-stress-field to an equivalent stress is not straight forward and will depend on the used yield criterion, but also on the mechanical and tribological properties of the sample itself. A simple linear conversion of H to σ_r by C* ≈ 3 (see equation (VIII)), as suggested by Tabor [10], may be alluring but is only applicable in limited cases where the deformation is fully plastic. The dependency of C* has been matter of debate for decades, still no universal conclusion could be drawn on the dependency of C*, unless that there is a strong influence of the elastic-plastic ratio E/σ and the strain-decisive opening angle θ [10,32,38,42–47]. The utility of the combined dimensionless parameter $\frac{E}{\sigma} \cdot \cot\theta$ has been addressed in finite element method (FEM) studies [42,43] and will be examined in detail in Publication D.

The challenges also confer to the definition of ε_r. In conventional compression or tension tests the initial length l_0 of the sample is known and the uniaxial strain ε_u is defined by considering the current length l of the specimen:

$$\varepsilon_u = \frac{l_0 - l}{l_0} \qquad \text{equation (XI)}$$

Since there is no initial length in spherical indentation, empiric definitions are used, where either the tip radius R or the current displacement h represents the reference and is related to the contact radius a_c [10,52–54] (see Figure 1b for details):

$$\varepsilon_r = \frac{a_c}{R} \qquad \text{equation (XII)}$$

$$\varepsilon_r = \frac{4}{3\pi} \cdot \frac{h}{a_c} \qquad \text{equation (XIII)}$$

The definition of ε_r is crucial for the implementation of strain-rate controlled experiments which explicitly increases the utility of nanoindentation experiments. The importance of strain-rate controlled tests with spherical tips has firstly been addressed by Feldner et al. [55] who introduced an approximate solution. Publication D will present further significant improvements on this subject.

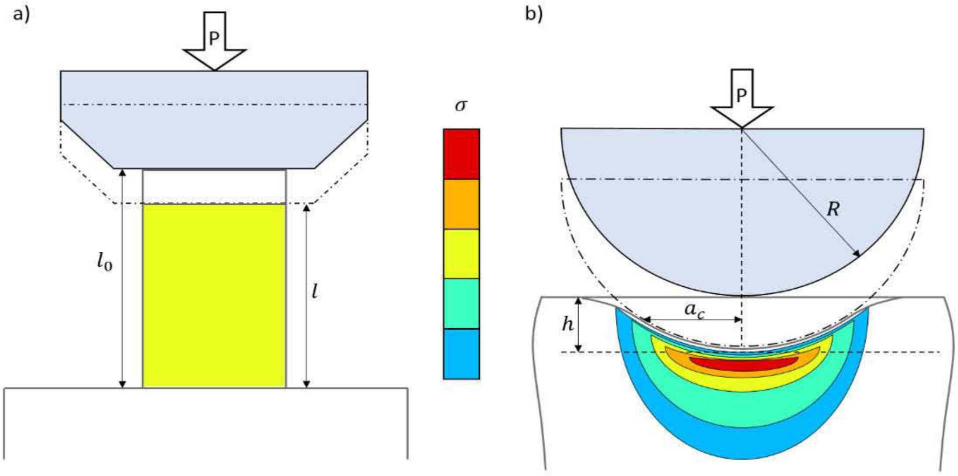

Figure 7. Schematics of a) a loaded uniaxial compression sample and b) a spherical indentation test with occurring stress-fields in the sampled volume.

5. List of publications

5.1. Contributions as main-author

Publication A:
Interface dominated mechanical properties of ultra-fine grained and nanoporous Au at elevated temperatures
A. Leitner, V. Maier-Kiener, J. Jeong, M.D. Abad, P. Hosemann, S.H. Oh, D. Kiener
Acta Materialia 121 (2016) 104-116.

Ultra-fine grained Au was produced via powder compression and subsequent high-pressure torsion deformation, while a nanoporous structure could be achieved by selective etching of AuFe compound samples. High temperature nanoindentation tests allowed to identify the dominating thermally activated mechanisms during deformation, indicating dislocation/interface interactions for both materials. Furthermore, hardening by annealing was noted for nanoporous Au as mobile dislocations leave the foam ligaments, thereby significantly increasing the local yield stress.

Publication B:
Extraction of Flow Behavior and Hall–Petch Parameters Using a Nanoindentation Multiple Sharp Tip Approach
A. Leitner, V. Maier-Kiener, D. Kiener
Advanced Engineering Materials 19:4 (2017) 1-9.

Comparison between Vickers and Berkovich nanoindentation hardness values demonstrated that significant differences occur due to different definitions of hardness and the elastic deformation. Using four self-similar sharp tips with varying opening angle allowed to obtain hardness values for discrete representative strains. By utilizing Ni and W samples with varying microstructure dimensions also Hall-Petch parameters were determined. Finally, after considering the indentation size effect, flow curves were extracted which are in good accordance with uniaxial literature data.

Publication C:
Dynamic nanoindentation testing: is there an influence on a material's hardness?
A. Leitner, V. Maier-Kiener, D. Kiener
Materials Research Letters 5:7 (2017) 486-493.

Hardness values obtained by static and dynamic indentation testing show partly significant deviations depending on the material. Within this study, it was demonstrated that deviations originate from a dropping strain-rate during hold regimes which are part of the measurement protocol in static and quasi-static tests. Hence, strain-rate sensitive materials are prone to errors and dynamic techniques, which guarantee to achieve the anticipated strain-rate, should be favored.

Publication D:
Essential refinements of spherical nanoindentation protocols for the reliable determination of mechanical flow curves
A. Leitner, V. Maier-Kiener, D. Kiener.
Submitted to an SCI journal.

Tip imperfections are a crucial problem for spherical nanoindentation approaches. Novel calibration procedures, introducing a geometrical-based area function, enhance the accuracy of tests significantly. Moreover, strain-rate controlled tests enable to implement methods for the characterization of thermally activated mechanisms by strain-rate jump or constant strain-rate (cSR) tests which are in good agreement with Berkovich reference measurements. A dependency of the linking factor between hardness and representative stress on the ratio between loading slope n_L and stiffness was identified and considered in the analysis of flow curves by spherical indentation. Those were in excellent agreement with flow curves from micro-pillar compression experiments conducted on corresponding samples.

5.2. Contributions as co-author

Publication E:
Thermally Activated Deformation Behavior of ufg-Au: Environmental Issues During Long-Term and High-Temperature Nanoindentation Testing
V. Maier-Kiener, A. Leitner, R. Pippan and D. Kiener
Journal of The Minerals, Metals & Materials Society 67:12 (2015) 2934-2944.

Publication F:
Dominating Deformation Mechanisms in Ultrafine-grained Chromium across Length-Scales and Temperatures
R. Fritz, D. Wimler, A. Leitner, V. Maier-Kiener and D. Kiener
Acta Materialia 140 (2017) 176-187.

Publication G:
Interface-dominated Strength Scaling Behavior in Ultrafine-grained Tungsten Samples
R. Fritz, A. Leitner, V. Maier-Kiener, R. Pippan and D. Kiener
Submitted to an SCI Journal.

Publication H:
Incipient plasticity and surface damage in $LiTaO_3$ and $LiNbO_3$ single crystals
M. Gruber, A. Leitner, D. Kiener, P. Supancic, R. Bermejo,
Submitted to an SCI Journal.

5.3. Remarks

In addition to the following remarks, all co-authors actively contributed to the preparation of the published manuscripts. Ideas and concepts mainly originate from D. Kiener and V. Maier-Kiener.

Publication A
V. Maier-Kiener essentially supported the analysis of the nanoindentation creep experiments. M.D. Abad aided with the high temperature nanoindentation tests, device calibrations and data analysis. P. Hosemann supported the authors by guiding the experiments and sharing his experience in materials testing in harsh environments. J. Jeong and S.H. Oh contributed with their know-how on nanoporous materials.

Publication B
Abundant discussions with V. Maier-Kiener and her experience with occurring indentation size effects vitally enhanced the manuscript.

Publication C
Broad experience on dynamic and static nanoindentation testing of V. Maier-Kiener allowed to identify potential causes of the occurring hardness deviations.

Publication D
V. Maier-Kiener assisted with the implementation of strain-rate controlled tests and data analysis.

6. Summary of publications

Following sections will give a brief overview of the used testing-setups, refinements of methodologies and main results of the published articles. Beside the discussion of experimental parameters and used samples, an exemplary study of the comprehensive mechanical characterization of nanoporous (NP) Au, fabricated at a bench scale, is given. This will be followed by investigations of dynamic testing techniques to identify the origin of hardness differences compared to static tests. Once the occurrent strain-rate effect is understood, the subsequent chapter will illustrate how to exploit data by utilizing sharp tips with varying opening angle. Revisiting spherical nanoindentation approaches will allow to substantially improve current methods by introducing a new calibration procedure as well as strain-rate controlled tests, thereby enabling the determination of rate-dependent properties such as m and V*. Finally, a direct comparison of flow curves from spherical indentation and uniaxial pillar microcompression tests will validate the used refinements.

6.1. Nanoindentation testing setups

Measurements mainly were carried out using a Nanoindenter G200 (Keysight Technologies, USA) with integrated CSM option. Diamond RT tips (Poisson's ratio ν=0.07, E=1140 GPa [56]) were obtained from Synton MDP LTD, Nidau, Switzerland. A laser heating stage (SurfaceTec, Hückelhoven, Germany) combined with sapphire high temperature tips (ν=0.23, E=440 GPa [12,56]) enabled measurements at elevated temperatures up to 500 °C. Local reducing protective gas flow at the tip and sample avoided oxidation of the sample. A frequency of 45 Hz and displacement amplitudes of 2 nm were used as CSM parameters to reduce possible artefacts from the integrated lock-in amplifier for all executed dynamic measurements [31]. The thermal drift was determined in a post-indentation segment at 10% of the maximum load and a holding time of 60 s. Any test exceeding drift values of 0.3 nm/s was not considered in the analysis.

Nanoindentation tests in Publication A were mainly performed using a Micro Materials NanoTest Platform 3 (Micro Materials, UK) with an adapted HT option. Diamond Berkovich tips were used for RT testing, while cBN (ν=0.12, E=833 GPa [57]) Berkovich tips were utilized for HT measurements. For this purpose, a heated stage allowed to reach testing temperatures up to 400 °C. The indenter cabinet was purged with a hydrogen/argon-gas to prevent oxidation effects. Further details of testing schedules and experimental parameters can be found in the corresponding publications.

6.2. Selected materials

The focus of this work are micromechanical investigations of novel high-strength materials which owe their outstanding mechanical properties their diminutive internal length scales. Reducing the grain size in metals goes along with an increase of the yield strength, while ductility is mostly maintained [58–60]. Severe plastic deformation (SPD) can serve as fabrication technique for modern materials that aim to exploit the HP-effect, ending up in UFG or NC microstructures. Most materials were fabricated by high pressure torsion (HPT), where samples are deformed by two rotating anvils in a quasi-constrained setup under simultaneous compression [61–65]. Likewise, accumulative roll bonding (ARB), where multiple metal sheets are repetitively rolled, can be utilized as SPD technique [66]. An example to create NC metals by bottom-up techniques is electrodeposition (ED) [67]. Beside high strength materials, in some publications also SX coarse grained (CG) and fine grained (FG) materials have been subject of examinations to evaluate the impact of grain boundaries. Table 1 gives an overview of tested materials with appendant obtained mechanical properties at room temperature performing Berkovich nanoindentation tests. Hardness values for materials prone to ISE refer to extrapolated bulk values [35]. All quantities of m and V* have been determined by strain-rate jump tests [48]. V* is normalized by the cubed Burgers vector b^3 of the respective material.

6.3. Application of advanced nanoindentation techniques on bench scale materials

Efficient modern material design is inconceivable without fabrication methods producing samples at a laboratory bench-scale. For instance, nanoporous materials can be well probed at small scales to avoid high costs of macro samples. NP materials are reckoned to possess self-healing features, making them particularly interesting for applications in harsh environments. For instance, NP samples exposed to ionizing radiation exhibit an exceptional radiation tolerance [68,69]. Additionally, ligaments of these nanofoams endure stresses close to their theoretical strengths [70–76] owed to their microstructure and its limited potential for dislocation plasticity. Alternatively, nanostructured metallic compounds with incoherent interfaces such as Cu/Nb are also considered as potential material for this application area [77–79]. Within this section, a prime example of the convenience of nanoindentation with its vast possibilities to comprehensively characterize materials using minimal volumes will be given.

Table 1. Materials tested within the present thesis with basic mechanical (H, E) and rate-dependent (m, V*) properties obtained by Berkovich nanoindentation experiments.

Material	GS or orientation	Fabric.	E [GPa]	H [GPa]	m [-]	V* $[b^3]$	Publication
Al 6014 FG	1.05 ± 0.25 µm	ARB	76 ± 1	1.24 ± 0.03	0.024 ± 0.004	30 ± 3	D
Au SX	(1 0 0)	aR	75 ± 1	0.54 ± 0.01	0.008 ± 0.001	140 ± 25	C
Au UFG	250 ± 100 nm	HPT	83 ± 4	2.60 ± 0.30	0.017 ± 0.002	20 ± 4	A, C, E
Au NP	70 ± 20 nm	HPT	30 ± 4	0.53 ± 0.14	0.029 ± 0.005	18 ± 1	A
$Au_{50}Fe_{50}$ NC	70 ± 20 nm	HPT	123 ± 4	5.59 ± 0.30	0.012 ± 0.002	18 ± 4	unpubl.
Cr SX	(1 0 0)	aR	293 ± 5	1.84 ± 0.04	0.050 ± 0.003	11 ± 2	C, F
Cr UFG	300 ± 100 nm	HPT	291 ± 2	5.49 ± 0.10	0.013 ± 0.001	17 ± 2	C, D, F
Cu SX	(1 1 0)	aR	121 ± 2	0.67 ± 0.06	0.005 ± 0.001	247 ± 36	C
Cu FG	2.7 ± 0.5 µm	ED	119 ± 4	0.77 ± 0.02	0.010 ± 0.002	140 ± 34	unpubl.
Cu UFG	280 ± 140 nm	HPT	127 ± 2	2.31 ± 0.02	0.047 ± 0.005	11 ± 2	D
$Cu_{50}Fe_{50}$	200 ± 100 nm	HPT	172 ± 2	4.06 ± 0.09	0.020 ± 0.005	15 ± 3	unpubl.
Fe CG	100 µm	aR	195 ± 2	1.10 ± 0.02	0.015 ± 0.001	85 ± 5	C
Fe UFG	200 ± 60 nm	HPT	207 ± 4	4.24 ± 0.07	0.014 ± 0.003	20 ± 3	unpubl.
FQ	amorphous	aR	72 ± 1	9.29 ± 0.04	0.010 ± 0.001	-	C, D
GaAs SX	(1 0 0)	aR	114 ± 1	7.48 ± 0.04	0.043 ± 0.003	-	C, D
GC	amorphous	aR	34 ± 1	5.00 ± 0.05	0.014 ± 0.002	-	C, D
$LiNbO_3$ SX	(0 -1 1 4)	aR	195 ± 1	6.57 ± 0.19	-	-	H
$LiTaO_3$ SX	(0 1 -1 2.8)	aR	248 ± 1	9.72 ± 0.14	-	-	H
Nb UFG	< 100 nm	HPT	106 ± 1	3.38 ± 0.02	0.018 ± 0.003	18 ± 4	unpubl.
Ni SX	(1 0 0)	aR	196 ± 2	1.03 ± 0.03	0.003 ± 0.002	449 ± 194	B, C
Ni FG	3.9 ± 1.4 µm	aR	208 ± 3	1.72 ± 0.04	0.009 ± 0.002	100 ± 22	B
Ni UFG	480 ± 200 nm	HPT	210 ± 3	3.36 ± 0.02	0.018 ± 0.002	21 ± 3	B
Ni NC	30 nm	ED	205 ± 2	5.89 ± 0.08	0.021 ± 0.001	11 ± 1	B, C, D
NiTi CG	40 µm	aR	75 ± 2	3.14 ± 0.19	0.008 ± 0.003	52 ± 17	unpubl.
NiTi UFG	unknown	HPT	69 ± 2	3.27 ± 0.10	0.008 ± 0.003	50 ± 21	unpubl.
Ta SX	(1 0 0)	aR	169 ± 1	1.05 ± 0.04	0.045 ± 0.005	14 ± 1	C
Ti CG	55 µm	aR	125 ± 1	1.90 ± 0.07	0.025 ± 0.003	15 ± 2	C
Ti UFG	unknown	HPT	192 ± 3	6.13 ± 0.14	0.014 ± 0.002	10 ± 1	C
W SX	(1 1 0)	aR	397 ± 7	4.13 ± 0.15	0.030 ± 0.002	6 ± 1	B, C, G
W CG	87 ± 33 µm	aR	404 ± 2	4.54 ± 0.01	0.029 ± 0.002	7 ± 1	B
W FG	3.3 ± 1.1 µm	HPT	415 ± 1	6.64 ± 0.04	0.026 ± 0.002	5 ± 1	B
W UFG	890 ± 510 nm	HPT	407 ± 9	8.70 ± 0.26	0.024 ± 0.002	5 ± 1	B, C, D, G
Zr CG	45 µm	aR	109 ± 1	1.97 ± 0.07	0.026 ± 0.003	12 ± 1	C
Zr UFG	unknown	HPT	127 ± 2	4.86 ± 0.21	0.024 ± 0.002	5 ± 1	C

6.3.1 Fabrication of bench-scale nanostructured materials

Fabrication by a powder route is an eligible approach to produce nanostructured compound samples [77,80,81]. Powders with average particle sizes < 15 µm were compressed and heavily deformed by two anvils which rotate against each other while maintaining high pressures up to 7.5 GPa. Depending on the radial position r and disk thickness t, enormous shear strains γ can be reached by increasing the numbers of rotations N:

$$\gamma = \frac{2\pi \cdot N}{t} \cdot \mathrm{r} \qquad \text{equation (XIV)}$$

The hardness profile in Figure 8 shows a gradient towards the disk center, as it is expected from equation (XIV), which in turn originates from the stronger refinement of the grains at larger radii, as seen from the depicted electron backscatter diffraction (EBSD) maps. In order to achieve a porous structure, two immiscible metal powders, namely Au and Fe, were mixed, whereupon Fe is selectively etched by hydrochloric acid after the deformation process [81]. Connectivity of both phases must be guaranteed to obtain a foam using this method.

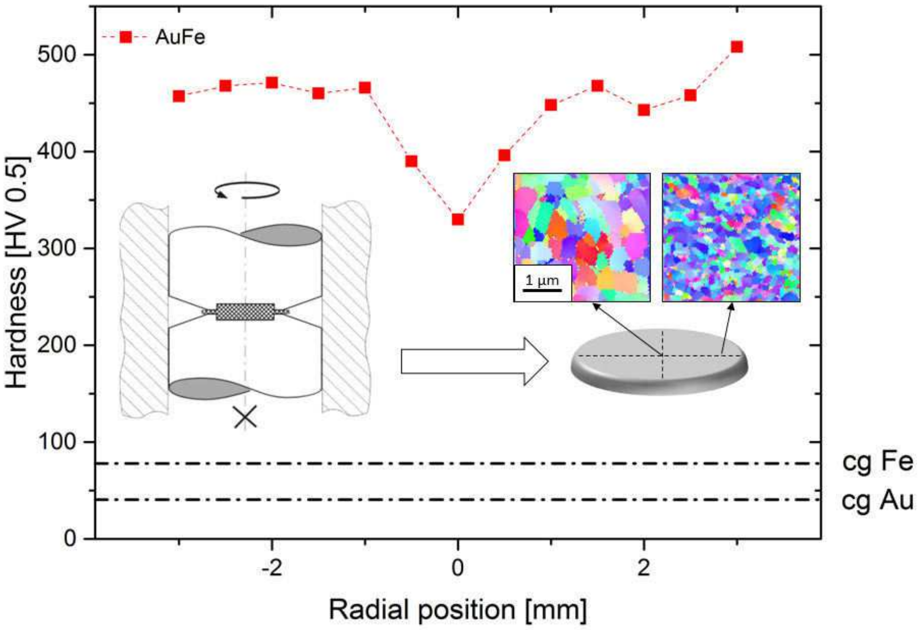

Figure 8.Typical hardness profile of a HPT-processed compound sample showing a gradient towards the specimen's center and a vast increase of hardness compared to the coarse grained raw materials. Insets show the scheme of HPT and the microstructure dependent on the radial position on the disk. Scale bar applies to both EBSD images.

6.3.2 Identification of deformation behavior by nanoindentation

Thermal stability is a limiting factor for NP Au produced by dealloying, where ligaments continuously coarsen if the temperature increases above RT [74]. This is not the case for the present NP Au (porosity ~50%) where remaining Fe drags the grain and ligament growth up to temperatures of 300 °C (see inset of Figure 9). HT nanoindentation allowed to determine the thermo-mechanical behavior which enables to conclude on the dominating deformation mechanism. Testing the as-received (aR) foam, rather low hardness values accompanied by an enhanced rate-sensitivity indicate dislocation/interface interactions as governing mechanism [50,82,83] (Figure 9). Thermal activation at 300 °C eases the movement of mobile dislocations, moreover surface diffusion could play a perceptible role which is also related to an increasing m [84]. Interestingly, m does not noticeably change when the sample is tested again after HT experiments but shows a considerable increase of H, an effect which has been noticed for SPD materials before [85,86]. Still the dominating deformation can be ascribed to dislocation plasticity. Presumably mobile dislocations can easily leave the material at free surfaces and this depletion of defects leads to ligament strengths close to the theoretical strength, if the mechanical models of Gibson and Ashby are used for analysis [87]. Also, E increases which might originate from microplasticity effects, causing a lower compliance of the sample. Reference measurements on UFG Au, fabricated with the same powder, did not show a hardening upon annealing or changing E, hence it can be assumed that the presence of free surface is decisive for the observed deformation behavior of NP Au. Determined values of V* support the observations, details are given in Publication A.

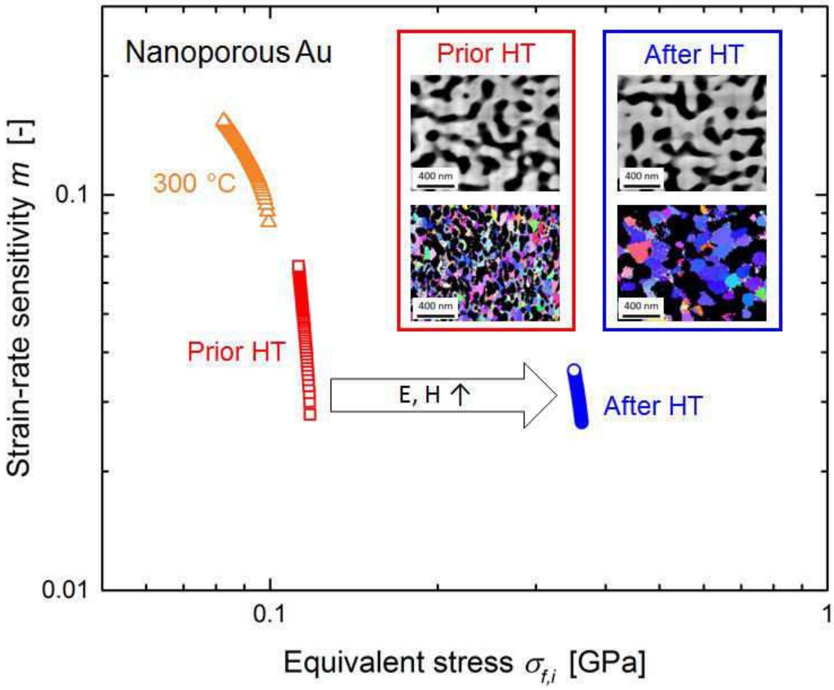

Figure 9. Representative profiles of strain-rate sensitivity of NP Au obtained by nanoindentation relaxation tests show a distinct increase of m at 300 °C. Despite a slight coarsening effect, hardness and modulus significantly increase for samples tested after HT. Nevertheless, there is no indication for a change of the dominating deformation mechanism.

6.3.3 Support of results by local porosity maps

The appearance of the plastic zone gives further insights in the deformation behavior of NP Au as densification can directly be evaluated by the preparation of focused ion beam (FIB) cross-sections of residual impressions. For this purpose, an automatized Python script was implemented which allows to scan obtained SEM micrographs of FIB cross-sections and creates color-coded porosity maps. A detailed description and a parameter study of the introduced procedure is given in Publication A. Figure 10 shows porosity maps of indentations made prior and after HT, showing distinct differences. While densification is clearly visible for the as received structure in Figure 10a this holds not true for the annealed material in Figure 10b.

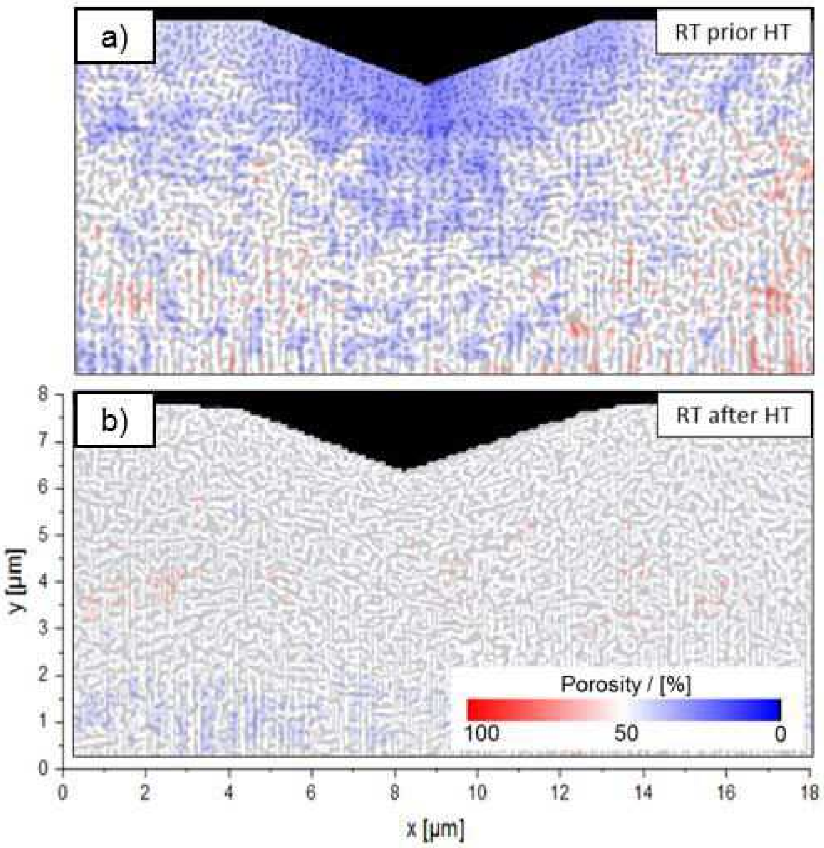

Figure 10. Densification of NP Au revealed by FIB cross-sections of nanoindentations performed a) prior and b) after HT experiments.

Considering mechanical and rate-dependent properties supported by the local porosity maps facilitates the establishment of a schematic model to describe the governing deformation mechanism, as demonstrated in Figure 11. The most conspicuous feature is the different densification behavior. In the aR sample sufficient mobile dislocations are present to arrange for the penetrating indenter tip, hence leading to lower H and a concentrated plastic zone size. At HT mobile dislocations employ the present thermal energy to leave the ligaments at the free surface.

Consequently, the microstructure exhibits less defects. Testing the annealed structure impedes the accommodation of the induced plastic deformation since dislocations must be nucleated. As annealed ligaments can bear higher stresses, the plastic zone can spread and results in an apparently non-densified appearance in Figure 10b. Clearly this is owed to the used analysis by porosity maps which is not sensitive enough to image densifications distributed in this large volume.

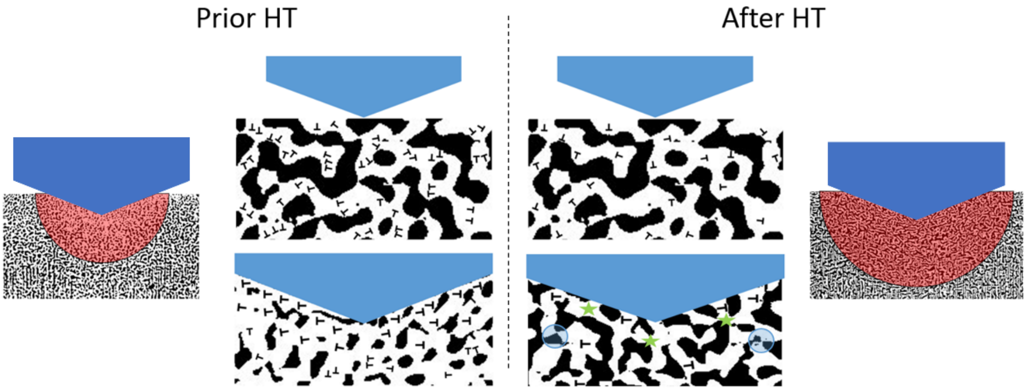

Figure 11. Schematic model of plastic deformation in NP Au. a) Samples tested prior HT contain enough dislocations to accommodate the deformation induced by the indenter tip. b) After HT, where mobile dislocations have left the material by thermal activation, the resistance against deformation increases, as dislocations must be nucleated to enable plastic deformation.

The work presented in the previous sections is an example par excellence how to exploit nanoindentation data and correlate it with deformation appearance to establish micromechanical models for modern materials. To extend the feasibility of indentation techniques, the following chapters will mainly deal with novel methodological approaches, particularly investigating the influence of dynamic indentation techniques and the possibility to extract mechanical flow curves by different approaches.

6.4. Investigation on the impact of dynamic measurement setups

The output of conventional static nanoindentation tests is limited as the elastic response must be accounted for. Therefore, mechanical properties can only be determined at the maximum displacement, where the slope of the unloading curve is equal to the material's stiffness. Adding multiple partial unloading sequences in the nanoindentation protocol enables to determine displacement dependent properties such as ISE [35]. However, many unloading cycles drastically increase the testing time, and measurements might be prone to thermal drift errors. Hence, the development of CSM was vitally important for the assertion of nanoindentation, which reduces testing times and massively increases the output of mechanical data over displacement. Admittedly, the manipulation of the force signal by a superimposed sinusoidal oscillation hazards an influence on the obtained properties. Therefore, numerous studies investigated dynamic indentation tests [24,25,27–30,88] and concluded that H at shallow depths, where the displacement amplitude is not negligible compared to the current penetration depth, deviates from values determined by static techniques. This is understandable by considering the respective partial loss of contact during loading, frequently referred to as Jackhammer effect [29]. Less attention has been drawn to deviations at large displacements. Figure 12 demonstrates that a vast difference of H is evident for tests on SX Cr depending on the used method. Static and multiple unloading tests show idem results, therefore excluding thermal drift as potential source of error. Conspicuously, the loading curves of CSM and multiple unloading tests shown in the inset match well, thus the hold regime is supposed to be crucial for the occurrent H differences.

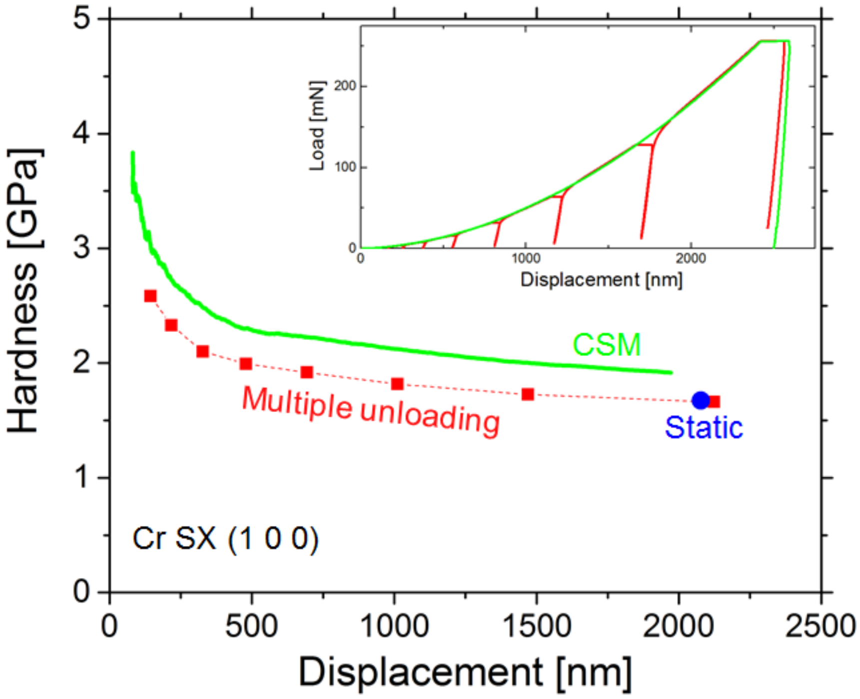

Figure 12. Hardness profile of SX Cr determined with different nanoindentation methods reveal significant differences. Notably, load-displacement curves shown in the inset coincide well except the hold segments.

6.4.1 Strain-rate effect & predictive model

The investigated materials, listed in Table 1, show a strongly varying absolute and relative hardness difference ΔH. Neither crystal structure nor mechanical properties could be associated with the characteristic of the occurring effect. Experiments on a broad range of materials were required to identify the correlation between ΔH and material properties. Rate-dependent properties were evaluated by conducting nanoindentation jump tests [48] for all examined samples which could then be linked to the hardness mismatch. To understand this behavior, a closer look at the hold regime, used in static and multiple unloading indentation experiments, gives further insights (Figure 13a). While H is obtained during the test and according to the anticipated strain-rate for dynamic tests, the hold segment in static tests causes a rapid decrease of $\dot{\varepsilon}$, hence leading to lower hardness values for rate-sensitive materials, such as SX Cr displayed in Figure 12. As seen from the inset in Figure 13a, the approximation used in equation (VI) breaks down during the hold period (solid blue line) as $\dot{P}$ becomes equal to zero and the term $\dot{H}$ becomes vital. Using the definition $\dot{h}/h$ instead shows a steady decrease of $\dot{\varepsilon}$ which can be used to predict the hardness difference between two different strain-rate tests if m is known [10,83,89]:

$$\begin{matrix} H_1 = K \cdot \dot{\varepsilon}_1^m \\ H_2 = K \cdot \dot{\varepsilon}_2^m \end{matrix} \qquad \dot{\varepsilon}_1 > \dot{\varepsilon}_2, \qquad \text{equation (XV)}$$

$$\Delta H = \frac{H_1 - H_2}{H_1} = \frac{K \cdot ({\dot{\varepsilon}_1}^m - {\dot{\varepsilon}_2}^m)}{K \cdot {\dot{\varepsilon}_1}^{\mathrm{m}}} = 1 - \left(\frac{\dot{\varepsilon}_2}{\dot{\varepsilon}_1}\right)^{\mathrm{m}} \qquad \text{equation (XVI)}$$

Figure 13b compares the expected ΔH derived from equation (XVI) with experimental data over a wide range of materials, demonstrating good agreement. Using the predictive model facilitates to reduce the average error down to a value of 2.5%. The CSM technique still results in slightly higher H values which might be ascribed to a weak dependence of m on H as noted in creep experiments [49,50,90]. Furthermore, this systematic error may arise from slightly differing material states. For static tests a stable microstructure is unloaded, while for CSM measurements a dynamic equilibrium structure is formed.

Summing up, the impact of different testing techniques has been investigated. It turns out that ΔH at high displacements does not originate from the dynamic stiffness measurement, but from related strain-rate effects. The use of CSM methods is beneficial since the anticipated $\dot{\varepsilon}$ is evidentially reached in the displacement regime used for the determination of the mechanical properties. Consequently, the strain-rate should be calculated and specified for static tests at the end of the hold regime if rate-sensitive materials are tested to guarantee non-restricted comparability among different nanoindentation techniques.

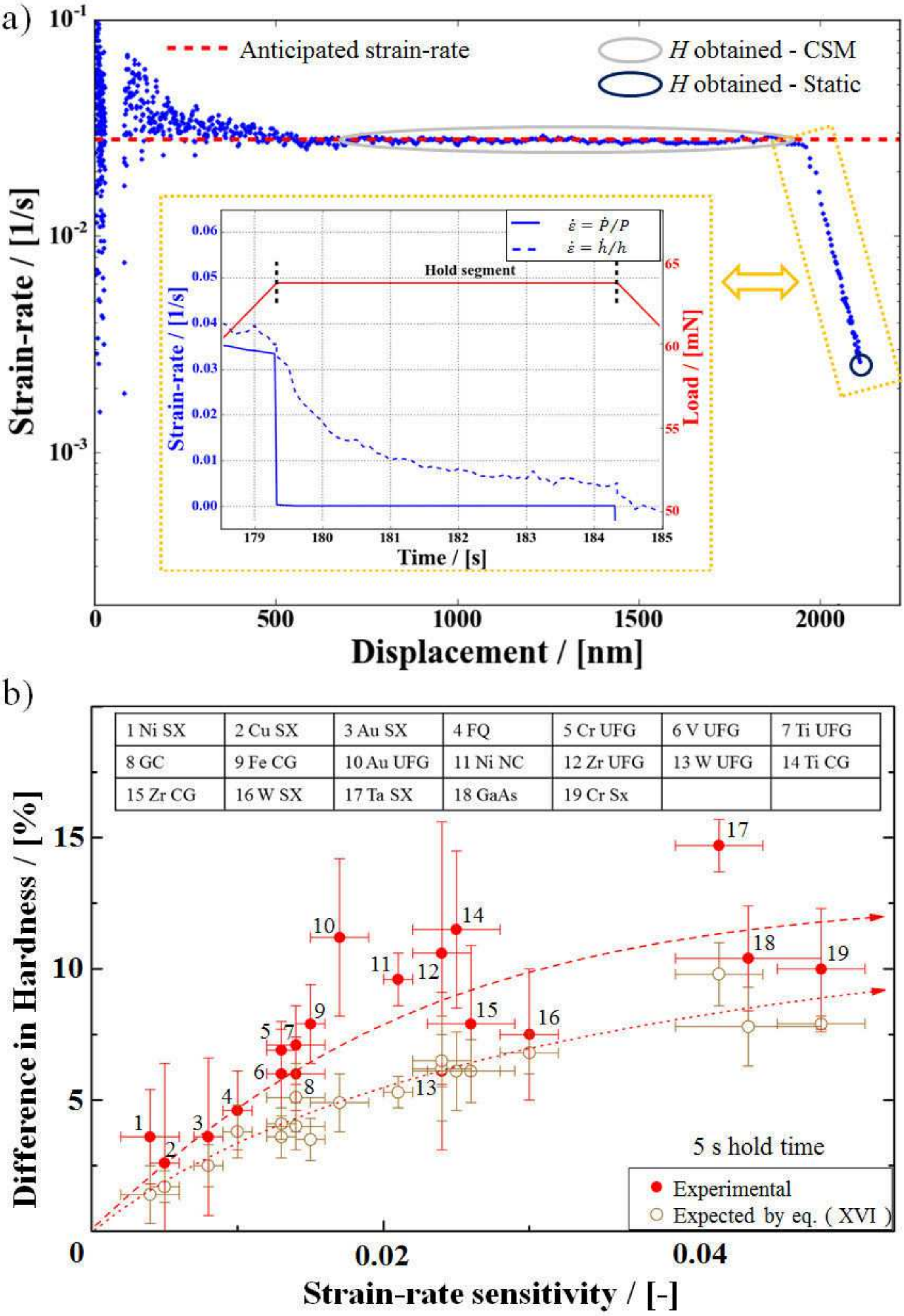

Figure 13. a) Strain-rate profile of a constant strain-rate nanoindentation test. CSM allows to determine H at the anticipated strain-rate. In static tests, where a hold regime is part of the measurement protocol, the strain-rate rapidly drops and causes apparent lower H values. b) Comparison of ΔH from experimental data and predicted from the model according to equation (XVI).

6.5. Exploitation of multiple sharp tip approaches

Sharp three-sided pyramidal tips have asserted themselves as the most commonly used geometries due to their straightforward fabrication which guarantees a high shape quality complying with their specifications. Four different indenter tips have been utilized in the present thesis, details are given in Table 2. The actual strain ε_a was obtained from calibration measurements by utilizing the first coefficient of a one-parameter-fit of equation (II) which can be converted to a representative cone angle and indentation strain according to equation (VII), respectively. Note that the nominal strain ε_n is in excellent agreement with ε_a obtained from calibration measurements, confirming that tip imperfections are negligible. The self-similar character further simplifies the consideration of indentation size-effects. Comparing H values of different tips, either displacement regimes with equal contact areas must be used for the analysis [88] (designated in Table 2) or extrapolation to bulk values have to be performed [35].

Table 2. Specifications of the four different tips used in this study. Nominal and actual strain are in good agreement indicating appropriate tip shapes. Given displacement regimes for the four tips refer to equal contact areas.

Tip	**Repr. cone angle α**	**Nominal strain ε_n**	**Actual strain ε_a**	**Mech. properties determined at**
FA 80	82.2 °	2.74 %	2.64 %	250 – 350 nm
Berkovich	70.3 °	7.16 %	7.16 %	650 – 780 nm
FA 50	56.9 °	13.04 %	12.62 %	1190 – 1430 nm
Cube Corner	42.3 °	21.98 %	21.65 %	2000 – 2400 nm

6.5.1 Determination of Hall-Petch parameters by sharp tip indentation

Testing of metals with varying average grain sizes allows to identify hardness HP parameters $k_{H,HP}$ and $H_{0,HP}$ in dependence of ε_r which can be converted to the related stress HP parameters [58,59] using equation (VIII):

$$\mathrm{H}(\varepsilon_r) = H_{0,HP}(\varepsilon_r) + k_{H,HP}(\varepsilon_r) \cdot \frac{1}{\sqrt{GS}} \quad \text{equation (XVII)}$$

$$\sigma(\varepsilon_r) = \sigma_0(\varepsilon_r) + k_{\sigma,HP}(\varepsilon_r) \cdot \frac{1}{\sqrt{GS}} \quad \text{equation (XVIII)}$$

For materials where the grain size exceeds the plastic zone size c, latter can be used as decisive material length scale for HP calculations and estimated by [38]:

$$\left(\frac{c}{a_c}\right)^3 = \frac{1}{3 \cdot tan\,\beta} \cdot \frac{E}{\sigma_y} \qquad \text{equation (XIX)}$$

HP parameters were determined on W and Ni specimens with four different microstructures each (see Table 1), ranging from SX to NC. Results for W are displayed in Figure 14. High correlation coefficients of > 0.96 indicate classical HP behavior down to the NC regime. The parameter $k_{\sigma,HP}$ is dependent on the work hardening behavior of the tested samples which is pronounced for the tested CG and SX specimens. For Ni, $k_{\sigma,HP}$ varies between 0.2 ± 0.05 and 0.28 ± 0.08 MPa·m$^{1/2}$, W yields values between 1.23 ± 0.33 and 1.86 ± 0.50 MPa·m$^{1/2}$. The value of σ_0 is directly related to ε_r as it represents the strength of the material in the absence of grain boundaries for a given strain. Hence, continuously increasing stress values with increasing indicates the expected classical work hardening behavior. Values obtained for W and Ni are in good agreement with literature, proofing that nanoindentation is a suitable technique to obtain grain-boundary hardening parameters [91–96].

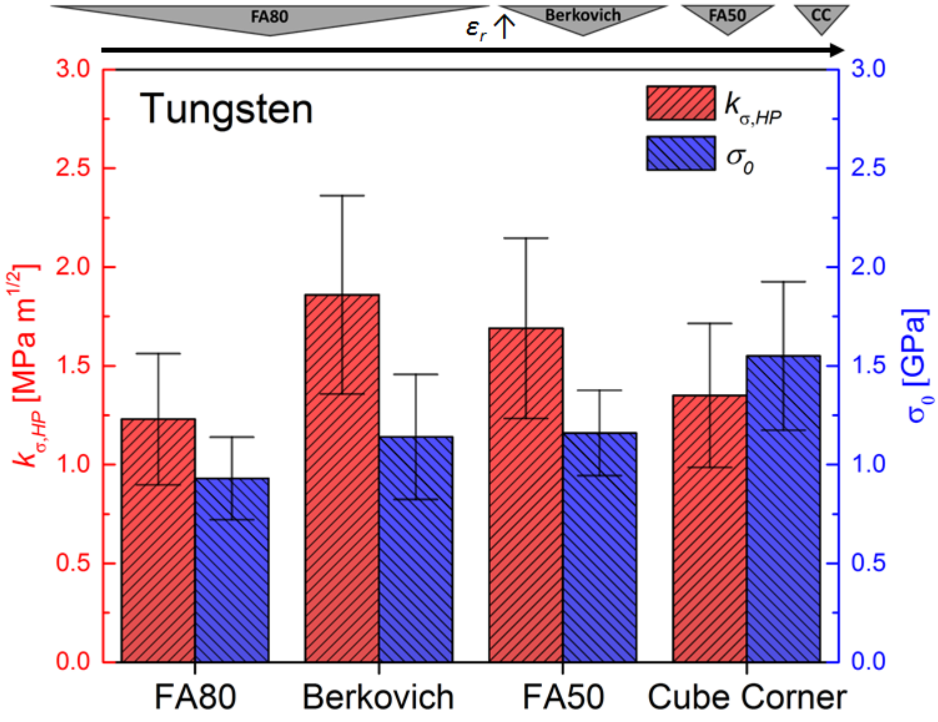

Figure 14. HP parameters obtained by various indenter tips on W samples with varying grain size. Above used representative cones to scale are shown.

6.5.2 Extraction of flow curves & validation of the concept

In principle, the determination of flow curves using a multiple sharp tip approach is straightforward. According to equation (VII) the representative strain depends only on the opening angle of the tip, hence utilizing various tips with differing opening angle enables to determine discrete points on a stress-strain curve. However, attention must be paid if a pronounced ISE is expected as it is the case for Ni SX in Figure 15a. Particularly at low strains, mismatches of almost 100% are notable which make results incomparable to literature macro data. In Figure 15b uniaxial literature values of samples with similar grain-sizes are displayed showing that once the hardness is properly accounted for the ISE and converted to a representative stress, values they agree well with nanoindentation experiments. Hence, it can be concluded that the simple empiric definitions of ε_r and σ_r proposed by Tabor [10] are suitable for Ni and W samples independent of the grain size once the size-effects are considered. Notably, the hydrostatic character of the indentation stress field is an asset compared to uniaxial tests as it allows to obtain mechanical properties also for brittle materials, yet the assessment of a materials ductility is hardly feasible.

Presented results implicate the numerous benefits of using multiple sharp tips for the characterization of metals. High tip shape qualities and straightforward analysis guarantee efficient experiments with comprehensive output of strain-dependent parameters such as HP coefficients or representative stress. Thus, the presented approach is an alternate for conventional uniaxial tests, especially if sample volumes are limited or required testing geometries are difficult to machine. Details are given in Publication B.

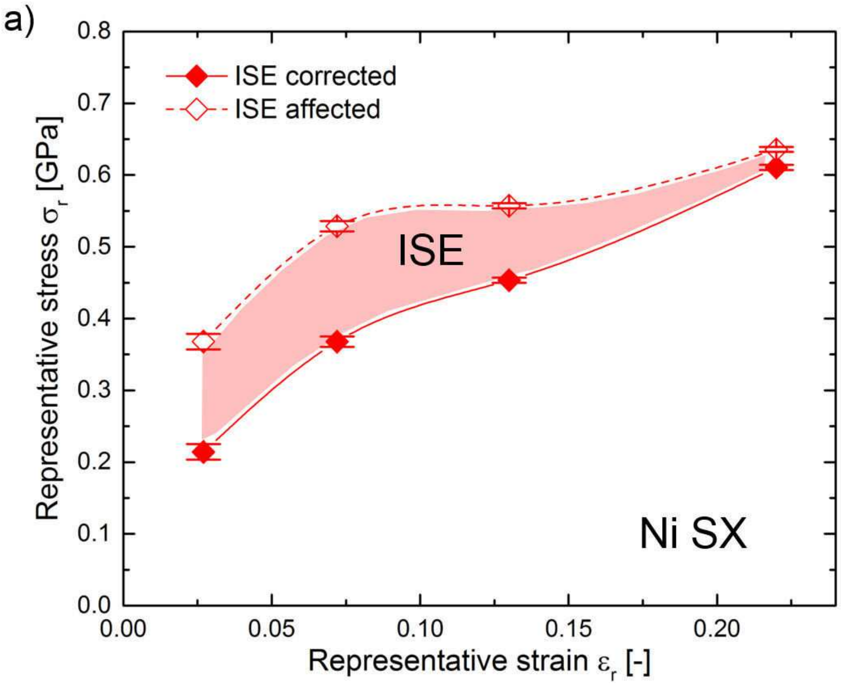

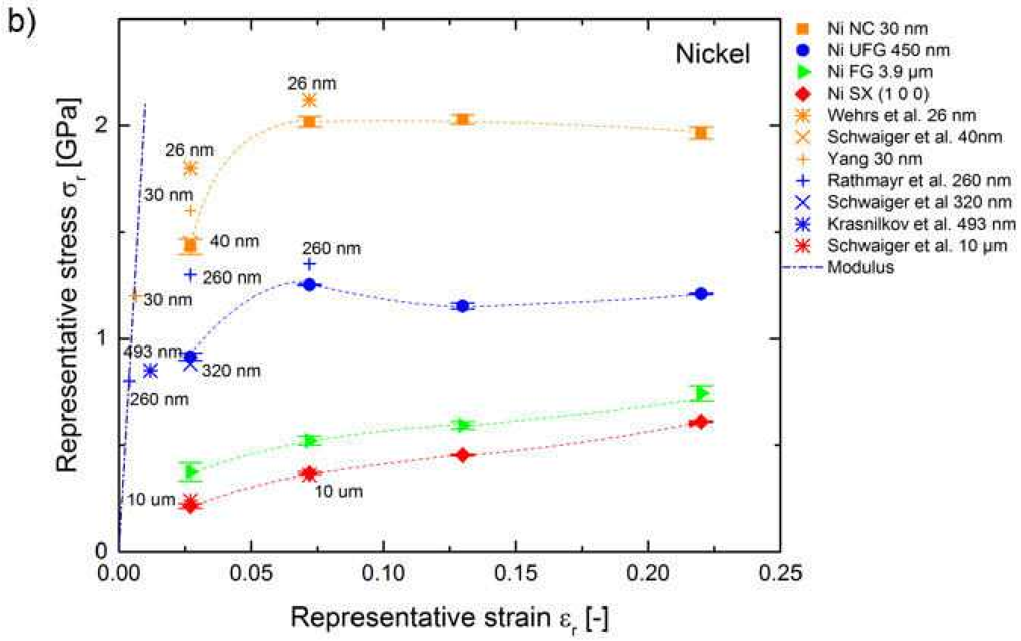

Figure 15. a) Comparison of stress-strain data obtained for SX Ni with and without consideration of ISE. b) Extracted flow curves of four Ni samples with different microstructures exhibit good agreement with literature values of samples of similar microstructures, indicated by symbols in the same color [97–101].

6.6. Refinements and extensions of spherical tip protocols

The potential of non-self-similar tip geometries is uncontestable, while at the same time numerous challenges must be faced which inhibit the extensive application so far. Testing protocols need to be refined to avoid propagation of errors originating from tip imperfections, undefined strain-rates during testing and unconsidered effects of mechanical properties for the conversion of H to σ_r. Following paragraphs will outline feasible refinements and advances which will ultimately allow to determine mechanical flow curves for materials with small internal length scales.

6.6.1 New calibration procedure for spherical tips

Imperfect tips shapes have been noticed to crucially impact the output of spherical indentation tests. As shown in Figure 16, the side view of a rounded tip shows a poor sphericity which goes along with errors in the obtained mechanical properties. The description of the tip shape with a representative radius is deficient as it only shifts the green modulus curve in parallel, hence retaining the strong non-physical gradient at low displacements. Certainly, the error introduced is not negligible and would not permit to access material flow curves. Therefore, the contact area in dependence of the contact displacement shall be described by a function inspired by the suggestions of Oliver and Pharr [12]. However, instead of using a series of power law terms as in equation (II), the variation of one exponent is expedient as it allows to alter the curvature efficiently, hence considering the ellipsoidal character of real tips:

$$A_c(h_c) = B_0 \cdot {h_c}^{B_1} - B_2 \cdot h_c^2 \qquad \text{equation (XX)}$$

For a perfect sphere, the values of the fitting parameters B_0, B_1 and B_2 result in $2 \cdot R \cdot \pi$, 1 and π, respectively, and thereby give physically based initial guesses for the used non-linear least square fitting method (Levenberg-Marquardt [102,103]), finally resulting in a robust and highly stable procedure. Figure 16 evidences the significant improvement achieved by using the new function as the modulus profile in blue accords to reference values independent of the displacement. Finally, it shall be mentioned that the spherical shape is limited by the opening angle of the used cone. Cones of 90° used in this study result in a maximum usable displacement of $R \cdot \left(1 - \frac{1}{\sqrt{2}}\right) \approx 0.29 \cdot R$.

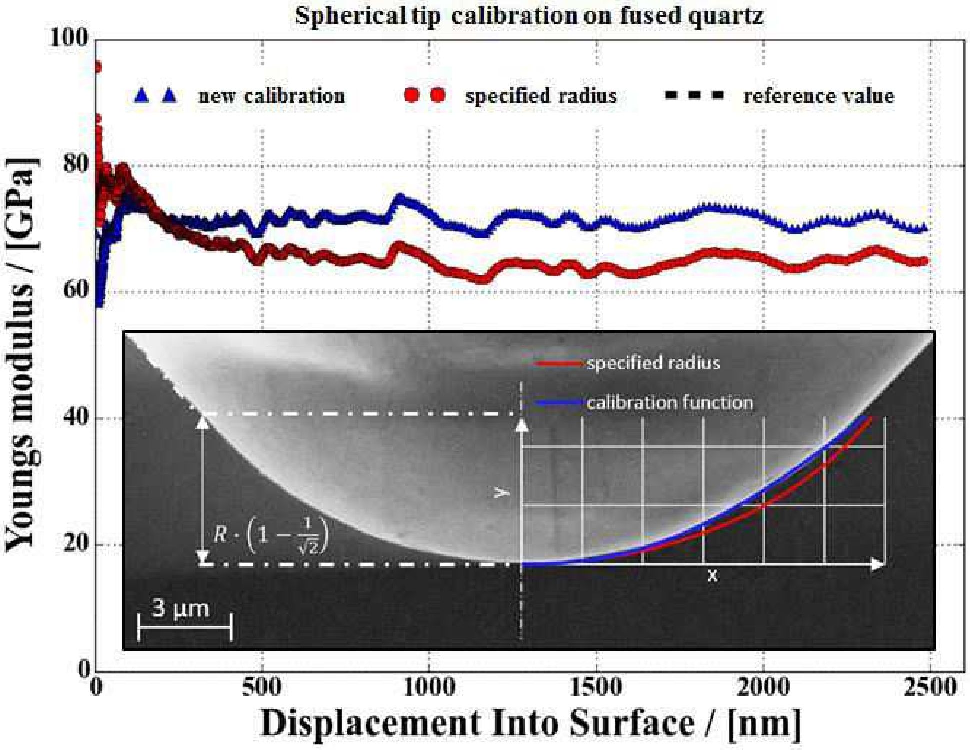

Figure 16. A new calibration method enhances the accuracy of indentation tests as proven by tests on isotropic FQ. The SEM micrograph of the tip contour, overlaid by functions of the specified radius and the novel area function affirm the utility of the new approach.

6.6.2 Strain-rate controlled experiments

The importance of strain-rate controlled tests for modern high-performance materials has been outlined in numerous studies [41,48–50,82,83,98,104–108], but remains a problem for spherical indentation testing as the induced strain is appreciably dependent on the tip shape. The novel elementary type of area function enables to control strain over time according to equation (XIII) which directly implicates tip imperfections from the calibration. Constant strain-rate tests conducted on GaAs SX, as depicted in Figure 17a, verify the applicability of the introduced testing method. The strain-rate profiles in Figure 17b confirm that the set values could be reached throughout the test, the pronounced discontinuities originate from pop-in events, indicating the first onset of plastic deformation [109]. As expected, no rate sensitivity is observed in the elastic regime, but is pronounced after the pop-in event. Furthermore, the slope of the elastic loading is conform to literature values of the Young's modulus of GaAs [110,111] and also matches E obtained by classical nanoindentation analysis [12], represented as magenta-colored profile in Figure 17a. Finally, Figure 17c displays the determined strain-rate sensitivity (equation (IX)) which coincidence well with values obtained Berkovich strain-rate jump tests. Even though these are related to a plastic strain of only 7%, the strain-insensitive behavior revealed from the spherical tests suggests the comparison to be reasonable. Figure 17a also underlines the importance of constant strain-rate tests for the extraction of flow curves since a non-linear strain-rate profile would significantly falsify work-hardening parameters and impede unrestricted comparability of spherical indentation tests. Strain-rate jump tests with spherical tips also yield to m values which are in good agreement with data from sharp tip indentation, details are given in Publication D.

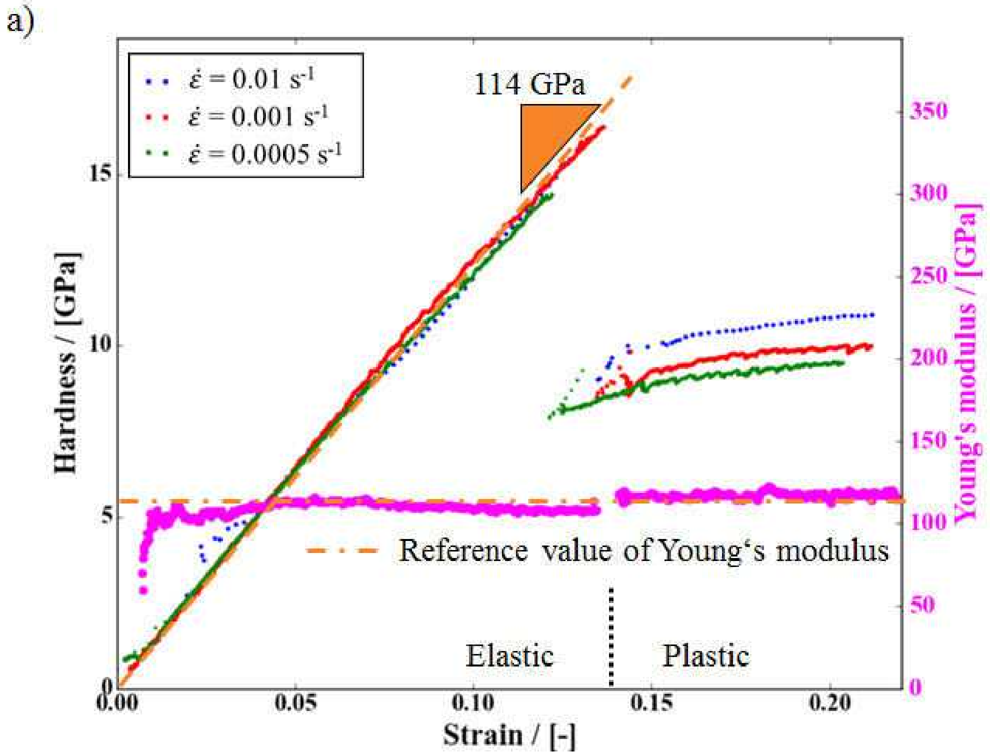

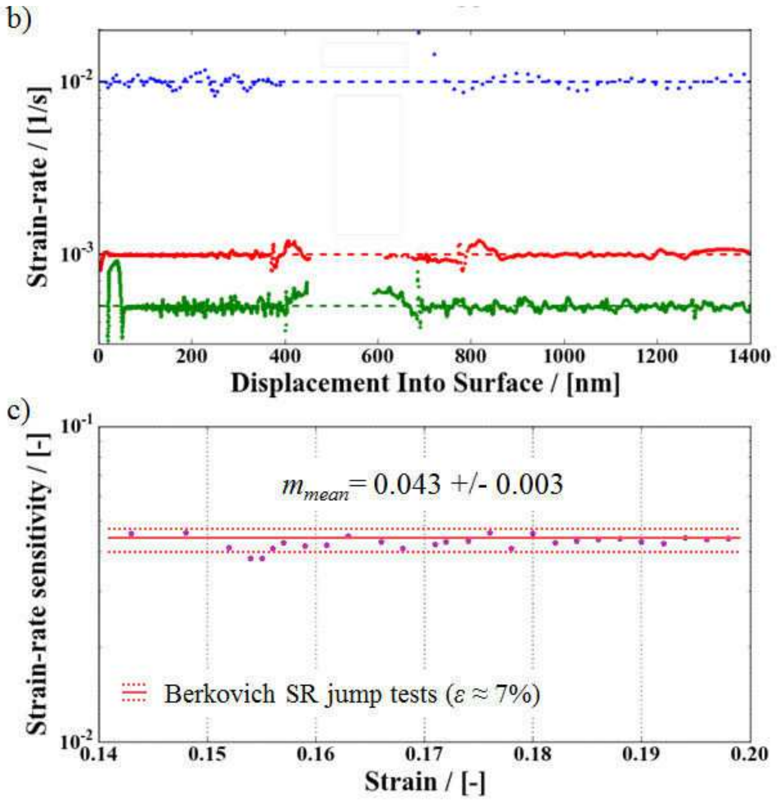

Figure 17. a) Constant strain-rate tests with a spherical indenter on GaAs SX. Conventional nanoindentation analysis and the slope of the Hooke's line result in the same value of around 114 GPa. Rate-dependence is restricted to the plastic regime. b) Strain-rate profile of the three different tests displayed in a). Discontinuities originate from pop-in events indicating the transition from elastic to elastoplastic deformation. c) Strain-rate sensitivity of GaAs is found independent of the indentation strain, hence reference values from Berkovich strain-rate jump tests are suitable for comparison, showing excellent agreement.

6.6.3 Determination of the constraint factor

Ensuring the consideration of imperfect tip shapes and achieving well controlled strain-rates, advances spherical nanoindentation move one step further towards the extraction of mechanical flow curves. In a last step, the constraint factor, linking hardness to the flow stress, must be addressed. Several studies showed the strong influence of elastic and plastic properties as well as induced indentation strain [10,32,38,42–47], often combined and expressed as dimensionless parameter:

$$\mu' = \frac{E_r}{\sigma_y} \cdot \frac{a}{R} \qquad \text{equation (XXI)}$$

Required a priori knowledge of E_r and yield stress σ_y are the main drawbacks of the use of μ'. However, some studies also demonstrated that the C* dependency can be linked to the occurrent hardness [32,47]. Particularly the approach to exploit the ratio between the unloading slope or stiffness, respectively, and the contact loading slope n_L is of interest since this parameter is experimentally accessible and closely related to μ':

$$\mu = \frac{S}{n_L} = \frac{E_r}{H} \cdot \frac{\cot\theta}{\pi} \qquad \text{equation (XXII)}$$

The derivation of this relation and exemplary profiles of μ over a wide range of materials can be found in publication D. FIB-milled micropillars of NC Ni were prepared to link μ to C*. Uniaxial compression experiments of these pillars provide uniaxial stress-strain curves which can be compared to spherical indentation data obtained at the same sample to exclude effects of inhomogeneities among different samples. The ratio of the stress values between uniaxial and nanoindentation tests within small strain increments ultimately allows to assess C* which can then be linked to the corresponding μ value. Figure 18a show this dependency where different deformation regimes shaded in different colors are noted. μ has a natural lower bound of 0.5 for purely elastic deformation because the loading and unloading curve match and $h_c = 0.5 \cdot h$ applies according to Hertz' contact theory [8]. The pseudo Hertzian regime, where elastic deformation dominates, is followed by the plastically dominated part. Finally, a steady state level with C*=2.91 is reached in the fully plastic regime which is in agreement with values found by various other research groups [10,32,42,43,47,48,112]. The physical background of this massive change of C* is the morphology of the plastic zone size which is constrained at low values of μ and continuously extends until it reaches the surface in the steady-state part. Figure 18b shows a schematic model established by Park et al. [43] who assessed this behavior by FEM studies which concurs to the experimental results of this study.

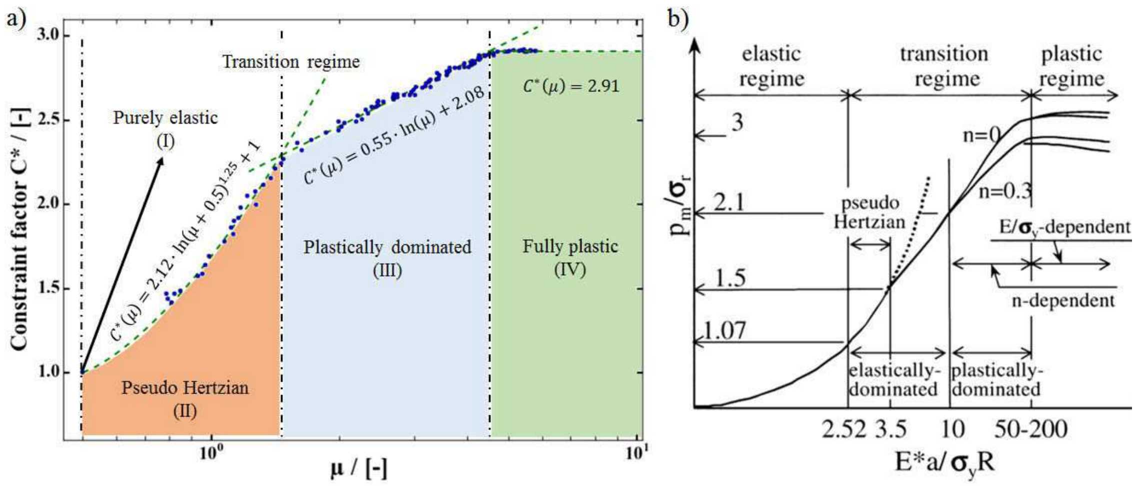

Figure 18. a) Experimental determination of C* in dependence of the dimensionless parameter μ shows varying deformation regimes. b) Schematic diagram of deformation regimes evaluated using FEM by Park et al. [43] are in agreement with experimental values obtained in this thesis.

It should be noted that a vastly different work-hardening behavior or deviating tribological properties might change the profile in Figure 18a. Hence, following partitioned empiric relations may only be used for materials with similar work hardening character and tribo-properties as in the present work:

$$C^*(\mu) = \begin{cases} 1 \quad , & \mu = 0.5 \quad \text{(I)} \\ 2.12 \cdot \ln(\mu + 0.5)^{1.25} + 1, & 0.5 < \mu < 1.45 \quad \text{(II)} \\ 0.55 \cdot \ln(\mu) + 2.08, & 1.45 \leq \mu < 4.5 \quad \text{(III)} \\ 2.91 \quad , & x \geq 4.5 \quad \text{(IV)} \end{cases} \qquad \text{equation (XXIII)}$$

However, this should be well given for most ultra-fine grained or nanostructured metals.

6.6.4 Validation by micro-pillar compression

Micro-pillars of four different materials were fabricated, and all featuring refined microstructures to exclude size-effects. Figure 19 compares flow curves obtained by uniaxial tests (green data) with spherical indentation data (blue), showing high coincidence once material dependent C* values and constant strain-rate methods are used. Interestingly, spherical indentation is apparently also able to detect instabilities as seen for UFG W in Figure 19d, which can be attributed to initiation of plastic deformation in adjacent grains. Lastly, Figure 19 underlines the importance of consideration of mechanical properties of the materials to be tested, as the use of a fixed C* (red data) introduces large errors, being most pronounced for materials with low E/σ-values.

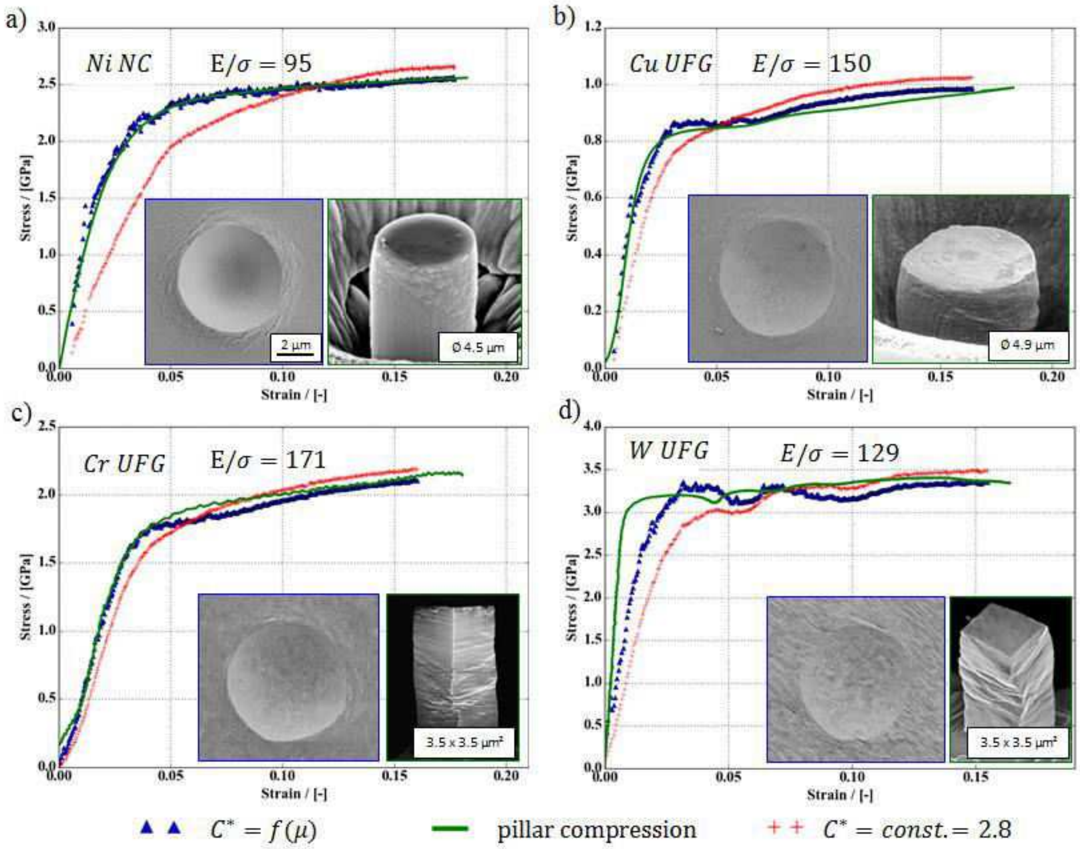

Figure 19. Stress-strain curves obtained by micro-pillar compression and spherical nanoindentation on the same material are in excellent accordance with each other. Dependent on the ratio of E/σ errors, introduced by using a fixed C* can be significant, particularly at low strains.

7. Concluding remarks

Elaborately working on nanoindentation techniques gives a true and fair view on the countless possibilities, but also on the restrictions of instrumented indentation. Even though testing setups and protocols are apparently simple, only painstaking deliberation of used methods and parameters guarantees a plenary comparability with properties obtained by other material testing techniques. Following conclusions can be drawn from investigations conducted within the present study:

- The comparability of nanoindentation to conventional hardness measurement techniques is generally restricted even if corrections are executed. Missing tip calibrations and elastic contributions reduce the precision of classical hardness tests, rendering instrumented indentation advantageous.
- Materials produced at a laboratory bench-scale, such as NP Au, can be extensively characterized by nanoindentation at ambient and elevated temperatures and give adjuvant indications of dominating deformation mechanisms in dependence of temperature.
- Special attention is required if rate-sensitive materials are tested. Standard static nanoindentation protocols do not consider the drop in the strain-rate within the hold regime which impedes a direct comparison to dynamic indentation data where the anticipated strain-rate is reliably reached. Hence, discrepancies of static and dynamic measurements might not be ascribed to influences of the superimposed force signal at large displacement, but actual strain-rates must be considered.
- Hall-Petch parameters obtained by sharp tip indentation are in accordance with data from uniaxial tests and can further be obtained for different representative strains if the indenter angle is varied.
- Multiple sharp tips can be utilized to assess flow curves which coincide well with uniaxial literature data if indentation size effects are accounted.
- Accurate tip calibrations based on the geometry of a sphere are necessary for acquirable spherical tips to gain precision required for the extraction of flow curves.
- Constant strain-rate tests are indispensable to measure realistic work hardening behavior and must be implemented to guarantee physical exploitable data.
- The determination of rate-dependent properties is feasible with spherical tips by either using constant strain-rate tests with different strain-rates or strain-rate jump tests which are in excellent agreement with reference measurements using a Berkovich indenter.

- The experimental determination of a material dependent C* which conforms with previous FEM studies, ultimately allows to assess flow curves of materials with refined microstructures, hence excluding tip size effects.

The present thesis outlines the versatility of nanoindentation and advances dynamic approaches with self-similar and non-self-similar tip geometries. Still, the attention of the reader shall also be drawn to the limitations of this small-scale technique. Conventional materials with large internal length scales are challenging to investigate as the tested volume might not be representative and influence the obtained properties by its own evolving dimension. This massively complicates the analysis, especially if the plastic zone size does not grow in a self-similar manner. On the other hand, it must also be considered that the anisotropy of inhomogeneous samples can have significant influences which also holds true for very thin samples. One should keep in mind that the plastic zone size is a multiple of the indentation depth in all directions. Thus, there is a given window of materials which can be tested unrestrictedly. Certainly, prospective studies, including FEM approaches, will be able to extend the spectrum of testable materials and structures.

Nanoindentation might be a swiss-army knife in terms of mechanical characterization, but only if used methods and parameters are expediently chosen and results are critically interpreted, demanding an extensive knowledge of material science and physics.

8. References

[1] R.A.F. de Réaumur, L'art de convertir le fer forgé en acier : et l'art d'adoucir le fer fondu, ou de faire des ouvrages de fer fondu aussi finis que de fer forgé, Chez M. Brunet, 1722.

[2] F. Mohs, Versuch einer Elementar-Methode zur naturhistorischen Bestimmung und Erkennung der Foßilien, Camesina, Wien, 1859.

[3] F.C. Calvert, R. Johnson, On the hardness of metals and alloys, J. Franklin Inst. 67 (1859) 198–203. doi:10.1016/0016-0032(59)90264-9.

[4] A. Martens, Handbuch der Materialkunde, Springer, Berlin, 1898.

[5] J.A. Brinell, Way of determining the hardness of bodies and some applications of the same, Tek. Tidskr. 5 (1900) 69.

[6] H.M. Rockwell, S.P. Rockwell, Hardness-tester, 1919.

[7] R.L. Smith, G.E. Sandly, An accurate method of determining the hardness of metals, with particular reference to those of a high degree of hardness, Proc. Inst. Mech. Eng. 102 (1922) 623–641. doi:10.1243/PIME_PROC_1922_102_033_02.

[8] H. Hertz, Über die Berührung fester elastischer Körper, J. Für Die Reine Und Angew. Math. 92 (1882) 156–171. doi:10.1515/crll.1882.92.156.

[9] L. Prandtl, Über die Härte plastischer Körper, Nachrichten von Der Gesellschaft Der Wissenschaften Zu Göttingen. (1920) 74–85. doi:10.1007/978-3-662-11836-8_7.

[10] D. Tabor, The Hardness of Metals, OUP Oxford, 1951.

[11] S.M. Walley, Historical origins of indentation hardness testing, Mater. Sci. Technol. 28 (2012) 1028–1044. doi:10.1179/1743284711Y.0000000127.

[12] W.C. Oliver, G.M. Pharr, An improved technique for determining hardness and elastic modulus using load and displacement sensing indentation experiments, J. Mater. Res. 7 (1992) 1564–1583. doi:10.1557/JMR.1992.1564.

[13] A.C. Fischer-Cripps, Nanoindentation, Springer New York, 2002. doi:10.1007/978-1-4419-9872-9.

[14] I. 14577, Metallic materials - Instrumented indentation test for hardness and materials parameters, ISO Tech. Rep. (2002).

[15] J.S. Field, M.V. Swain, A Simple Predictive Model for Spherical Indentation, J. Mater. Res. 8 (1993) 297–306. doi:10.1557/JMR.1993.0297.

[16] A.J. Bushby, Nanoindentation using spherical indenters, Nondestruct. Test. Eval. 17 (2001) 213–234. doi:10.1080/10589750108953112.

[17] A.J. Bushby, N.M. Jennett, Determining the Area Function of Spherical Indenters for Nanoindentation, Mater. Res. Soc. Symp. Proc. 649 (2000) 1–6. doi:10.1557/PROC-649-Q7.17.

[18] I. Sneddon, The relation between load and penetration in the axisymmetric Boussinesq problem for a punch of arbitrary profile, Int. J. Eng. Sci. 3 (1965) 47–57. doi:https://doi.org/10.1016/0020-7225(65)90019-4.

[19] E. Meyer, Untersuchungen über Härteprüfung und Härte, Zeitschrift Verein Dtsch. Ingenieure. 52 (1909).

[20] J.B. Pethica, W.C. Oliver, Mechanical Properties of Nanometre Volumes of Material: use of

the Elastic Response of Small Area Indentations, MRS Proc. 130 (1988) 13–23. doi:10.1557/PROC-130-13.

[21] S.A.S. Asif, K.J. Wahl, R.J. Colton, Nanoindentation and contact stiffness measurement using force modulation with a capacitive load-displacement transducer, Rev. Sci. Instrum. 70 (1999) 2408–2413. doi:10.1063/1.1149769.

[22] X. Li, B. Bhushan, A review of nanoindentation continuous stiffness measurement technique and its applications, Mater. Charact. 48 (2002) 11–36. doi:10.1016/S1044-5803(02)00192-4.

[23] W.C. Oliver, G.M. Pharr, Measurement of hardness and elastic modulus by instrumented indentation: Advances in understanding and refinements to methodology, J. Mater. Res. 19 (2004) 3–20. doi:10.1557/jmr.2004.19.1.3.

[24] J. Hay, P. Agee, E. Herbert, Continuous Stiffness Measurement during instrumented indentation testing, Exp. Tech. 34 (2010) 86–94. doi:10.1111/j.1747-1567.2010.00618.x.

[25] Y.-T. Cheng, W. Ni, C.-M. Cheng, Nonlinear Analysis of Oscillatory Indentation in Elastic and Viscoelastic Solids, Phys. Rev. Lett. 97 (2006) 75506-1–4. doi:10.1103/PhysRevLett.97.075506.

[26] K. Durst, O. Franke, A. Böhner, M. Göken, Indentation size effect in Ni-Fe solid solutions, Acta Mater. 55 (2007) 6825–6833. doi:10.1016/j.actamat.2007.08.044.

[27] M.J. Cordill, N.R. Moody, W.W. Gerberich, Effects of dynamic indentation on the mechanical response of materials, J. Mater. Res. 23 (2008) 1604–1613. doi:10.1557/JMR.2008.0205.

[28] G.M. Pharr, J.H. Strader, W.C. Oliver, Critical issues in making small-depth mechanical property measurements by nanoindentation with continuous stiffness measurement, J. Mater. Res. 24 (2009) 653–666. doi:10.1557/jmr.2009.0096.

[29] M.J. Cordill, M.S. Lund, J. Parker, C. Leighton, A.K. Nair, D. Farkas, N.R. Moody, W.W. Gerberich, The Nano-Jackhammer effect in probing near-surface mechanical properties, Int. J. Plast. 25 (2009) 2045–2058. doi:10.1016/j.ijplas.2008.12.015.

[30] K.W. Siu, A.H.W. Ngan, Oscillation-induced softening in copper and molybdenum from nano- to micro-length scales, Mater. Sci. Eng. A. 572 (2013) 56–64. doi:10.1016/j.msea.2013.02.037.

[31] B. Merle, V. Maier-Kiener, G.M. Pharr, Influence of modulus-to-hardness ratio and harmonic parameters on continuous stiffness measurement during nanoindentation, Acta Mater. 134 (2017) 167–176. doi:10.1016/j.actamat.2017.05.036.

[32] J.L. Hay, W.C. Oliver, A. Bolshakov, G.M. Pharr, Using the ratio of loading slope and elastic stiffness to predict pile-up and constraint factor during indentation, MRS Proc. 522 (1998) 101–106. doi:10.1557/PROC-522-101.

[33] A. Bolshakov, G.M. Pharr, Influences of pileup on the measurement of mechanical properties by load and depth sensing indentation techniques, J. Mater. Res. 13 (1998) 1049–1058. doi:10.1557/JMR.1998.0146.

[34] N.X. Randall, C. Julia-Schmutz, Evalution of contact area and pile-up during the nanoindentation of soft coatings on hard substrates, Mat. Res. Soc. Symp. Proc. 522 (1998) 21–26. doi:10.1557/PROC-522-21.

[35] W.D. Nix, H. Gao, Indentation size effects in crystalline materials: A law for strain gradient plasticity, J. Mech. Phys. Solids. 46 (1998) 411–425. doi:10.1016/S0022-5096(97)00086-0.

[36] H. Mughrabi, On the current understanding of strain gradient plasticity, Mater. Sci. Eng. A. 387–389 (2004) 209–213. doi:10.1016/j.msea.2004.01.086.

[37] N. Gane, F.P. Bowden, Microdeformation of solids, J. Appl. Phys. 39 (1968) 1432–1435. doi:10.1063/1.1656376.

[38] K.L. Johnson, The correlation of indentation experiments, J. Mech. Phys. Solids. 18 (1970) 115–126. doi:10.1016/0022-5096(70)90029-3.

[39] S. Qu, Y. Huang, G.M. Pharr, The indentation size effect in the spherical indentation of iridium : A study via the conventional theory of mechanism-based strain gradient plasticity, Int. J. Plast. 22 (2006) 1265–1286. doi:10.1016/j.ijplas.2005.07.008.

[40] K. Durst, M. Göken, G.M. Pharr, Indentation size effect in spherical and pyramidal indentations, J. Phys. D. Appl. Phys. 41 (2008) 1–5. doi:10.1088/0022-3727/41/7/074005.

[41] B.N. Lucas, W.C. Oliver, Indentation power-law creep of high-purity indium, Metall. Mater. Trans. A. 30 (1999) 601–610. doi:10.1007/s11661-999-0051-7.

[42] S.-D. Mesarovic, N.A. Fleck, Spherical indentation of elastic-plastic solids, Proc. R. Soc. London A Math. Phys. Eng. Sci. 455 (1999) 2707–2728. doi:10.1098/rspa.1999.0423.

[43] Y.J. Park, G.M. Pharr, Nanoindentation with spherical indenters : finite element studies of deformation in the elastic – plastic transition regime, Thin Solid Films. 448 (2004) 246–250. doi:10.1016/S0040-6090.

[44] M. Mata, O. Casals, J. Alcalá, The plastic zone size in indentation experiments: The analogy with the expansion of a spherical cavity, Int. J. Solids Struct. 43 (2006) 5994–6013. doi:10.1016/j.ijsolstr.2005.07.002.

[45] S. Kang, Y. Kim, K. Kim, J. Kim, D. Kwon, Extended expanding cavity model for measurement of flow properties using instrumented spherical indentation, Int. J. Plast. 49 (2013) 1–15. doi:http://dx.doi.org/10.1016/j.ijplas.2013.02.014.

[46] X. Chen, J.J. Vlassak, Numerical study on the measurement of thin film mechanical properties by means of nanoindentation, J. Mater. Res. 16 (2001) 2974–2982. doi:10.1557/JMR.2001.0408.

[47] M. Rodríguez, J.M. Molina-Aldareguia, C. González, J. Llorca, Determination of the mechanical properties of amorphous materials through instrumented nanoindentation, Acta Mater. 60 (2012) 3953–3964. doi:10.1016/j.actamat.2012.03.027.

[48] V. Maier, K. Durst, J. Mueller, B. Backes, H.W. Höppel, M. Göken, Nanoindentation strain-rate jump tests for determining the local strain-rate sensitivity in nanocrystalline Ni and ultrafine-grained Al, J. Mater. Res. 26 (2011) 1421–1430. doi:10.1557/jmr.2011.156.

[49] D. Peykov, E. Martin, R.R. Chromik, R. Gauvin, M. Trudeau, Evaluation of strain rate sensitivity by constant load nanoindentation, J. Mater. Sci. 47 (2012) 7189–7200. doi:10.1007/s10853-012-6665-y.

[50] V. Maier, B. Merle, M. Göken, K. Durst, An improved long-term nanoindentation creep testing approach for studying the local deformation processes in nanocrystalline metals at room and elevated temperatures, J. Mater. Res. 28 (2013) 1177–1188. doi:10.1557/jmr.2013.39.

[51] N.A. Sakharova, J. V Fernandes, J.M. Antunes, M.C. Oliveira, Comparison between Berkovich, Vickers and conical indentation tests: A three-dimensional numerical simulation study, Int. J. Solids Struct. 46 (2009) 1095–1104. doi:10.1016/j.ijsolstr.2008.10.032.

[52] S.R. Kalidindi, S. Pathak, Determination of the effective zero-point and the extraction of

spherical nanoindentation stress – strain curves, Acta Mater. 56 (2008) 3523–3532. doi:10.1016/j.actamat.2008.03.036.

[53] S. Pathak, J. Shaffer, S.R. Kalidindi, Determination of an effective zero-point and extraction of indentation stress – strain curves without the continuous stiffness measurement signal, Scr. Mater. 60 (2009) 439–442. doi:10.1016/j.scriptamat.2008.11.028.

[54] S. Pathak, S.R. Kalidindi, Spherical nanoindentation stress-strain curves, Mater. Sci. Eng. R Reports. 91 (2015) 1–36. doi:10.1016/j.mser.2015.02.001.

[55] P. Feldner, B. Merle, M. Göken, Determination of the strain-rate sensitivity of ultrafine-grained materials by spherical nanoindentation, J. Mater. Res. 49 (2017) 1466–1473. doi:10.1557/jmr.2017.69.

[56] G. Simmons, H. Wang, Single Crytsal Elastic Constants and Calculated Aggregate Properties - A Handbook, MIT Press, Cambridge, MA, 1971.

[57] M.P. D'Evelyn, T. Taniguchi, Elastic properties of translucent polycrystalline cubic boron nitride as characterized by the dynamic resonance method, Diam. Relat. Mater. 8 (1999) 1522–1526. doi:10.1016/S0925-9635(99)00077-1.

[58] E.O. Hall, The Deformation and Ageing of Mild Steel: Discussion of Results, Proc. Phys. Soc. Sect. B. 64 (1951) 747. doi:10.1088/0370-1301/64/9/303.

[59] N.J. Petch, The cleavage strength of polycrystals, J. Iron Steel Inst. 174 (1953) 25–28.

[60] X. Li, K. Lu, Playing with defects in metals, Nat. Mater. 16 (2017) 700–701. doi:10.1038/nmat4929.

[61] R. Pippan, S. Scheriau, A. Hohenwarter, M. Hafok, Advantages and Limitations of HPT: A Review, Mater. Sci. Forum. 584–586 (2008) 16–21. doi:10.4028/www.scientific.net/MSF.584-586.16.

[62] R. Pippan, F. Wetscher, M. Hafok, A. Vorhauer, I. Sabirov, The Limits of Refinement by Severe Plastic Deformation, Adv. Eng. Mater. 8 (2006) 1046–1056. doi:10.1002/adem.200600133.

[63] R.Z. Valiev, Y. Estrin, Z. Horita, T.G. Langdon, M.J. Zehetbauer, Y.T. Zhu, Fundamentals of Superior Properties in Bulk Nano SPD Materials, Mater. Res. Lett. 4 (2016) 1–21. doi:10.1080/21663831.2015.1060543.

[64] A.P. Zhilyaev, T.G. Langdon, Using high-pressure torsion for metal processing: Fundamentals and applications, Prog. Mater. Sci. 53 (2008) 893–979. doi:10.1016/j.pmatsci.2008.03.002.

[65] R.Z. Valiev, R.K. Islamgaliev, I. V Alexandrov, Bulk nanostructured materials from severe plastic deformation, Prog. Mater. Sci. 45 (2000) 103–189. doi:10.1016/S0079-6425(99)00007-9.

[66] Y. Saito, H. Utsunomiya, N. Tsuji, T. Sakai, Novel ultra-high straining process for bulk materials—development of the accumulative roll-bonding (ARB) process, Acta Mater. 47 (1999) 579–583. doi:10.1016/S1359-6454(98)00365-6.

[67] L.P. Bicelli, B. Bozzini, C. Mele, L. D'Urzo, A review of nanostructural aspects of metal electrodeposition, Int. J. Electrochem. Sci. 3 (2008) 356–408. doi:10.1.1.655.5201.

[68] E.M. Bringa, J.D. Monk, A. Caro, A. Misra, L. Zepeda-Ruiz, M. Duchaineau, F. Abraham, M. Nastasi, S.T. Picraux, Y.Q. Wang, D. Farkas, Are Nanoporous Materials Radiation Resistant?, Nano Lett. 12 (2012) 3351–3355. doi:10.1021/nl201383u.

[69] Y. Sun, S.A. Burger, T.J. Balk, Controlled ligament coarsening in nanoporous gold by

annealing in vacuum versus nitrogen, Philos. Mag. 94 (2014) 1001–1011. doi:10.1080/14786435.2013.876113.

[70] J. Biener, A.M. Hodge, A. V Hamza, L.M. Hsiun, J.H. Satcher, Nanoporous Au: A high yield strength material, J. Appl. Phys. 97 (2005). doi:10.1063/1.1832742.

[71] C.A. Volkert, E.T. Lilleodden, Size effects in the deformation of sub-micron Au columns, Philos. Mag. 86 (2006) 5567–5579. doi:10.1080/14786430600567739.

[72] D. Lee, X. Wei, X. Chen, M. Zhao, S.C. Jun, J. Hone, E.G. Herbert, W.C. Oliver, J.W. Kysar, Microfabrication and mechanical properties of nanoporous gold at the nanoscale, Scr. Mater. 56 (2007) 437–440. doi:10.1016/j.scriptamat.2006.08.069.

[73] N.J. Briot, T. Kennerknecht, C. Eberl, T.J. Balk, Mechanical properties of bulk single crystalline nanoporous gold investigated by millimetre-scale tension and compression testing, Philos. Mag. 94 (2014) 847–866. doi:10.1080/14786435.2013.868944.

[74] M. Hakamada, M. Mabuchi, Mechanical strength of nanoporous gold fabricated by dealloying, Scr. Mater. 56 (2007) 1003–1006. doi:10.1016/j.scriptamat.2007.01.046.

[75] A.M. Hodge, J. Biener, J.R. Hayes, P.M. Bythrow, C.A. Volkert, A. V Hamza, Scaling equation for yield strength of nanoporous open-cell foams, Acta Mater. 55 (2007) 1343–1349. doi:10.1016/j.actamat.2006.09.038.

[76] N. Mameka, K. Wang, J. Markmann, E.T. Lilleodden, J. Weissmüller, Nanoporous Gold - Testing Macro-scale Samples to Probe Small-scale Mechanical Behavior, Mater. Res. Lett. 0 (n.d.) 1–10. doi:10.1080/21663831.2015.1094679.

[77] M.M. Primorac, M.D. Abad, P. Hosemann, M. Kreuzeder, V. Maier, D. Kiener, Elevated temperature mechanical properties of novel ultra-fine grained Cu-Nb composites, Mater. Sci. Eng. A. 625 (2015) 296–302. doi:http://dx.doi.org/10.1016/j.msea.2014.12.020.

[78] A. Misra, M.J. Demkowicz, X. Zhang, R.G. Hoagland, The radiation damage tolerance of ultra-high strength nanolayered composites, J. Miner. Met. Mater. Soc. 59 (2007) 62–65. doi:10.1007/s11837-007-0120-6.

[79] N. Li, N.A. Mara, Y.Q. Wang, M. Nastasi, A. Misra, Compressive flow behavior of Cu thin films and Cu/Nb multilayers containing nanometer-scale helium bubbles, Scr. Mater. 64 (2011) 974–977. doi:10.1016/j.scriptamat.2011.02.001.

[80] A. Bachmaier, M. Kerber, D. Setman, R. Pippan, The formation of supersaturated solid solutions in Fe-Cu alloys deformed by high-pressure torsion, Acta Mater. 60 (2012) 860–871. doi:10.1016/j.actamat.2011.10.044.

[81] M. Kreuzeder, M.-D. Abad, M.-M. Primorac, P. Hosemann, V. Maier, D. Kiener, Fabrication and thermo-mechanical behavior of ultra-fine porous copper, J. Mater. Sci. 50 (2015) 634–643. doi:10.1007/s10853-014-8622-4.

[82] J. Chen, L. Lu, K. Lu, Hardness and strain rate sensitivity of nanocrystalline Cu, Scr. Mater. 54 (2006) 1913–1918. doi:10.1016/j.scriptamat.2006.02.022.

[83] Q. Wei, S. Cheng, K.T. Ramesh, E. Ma, Effect of nanocrystalline and ultrafine grain sizes on the strain rate sensitivity and activation volume: fcc versus bcc metals, Mater. Sci. Eng. A. 381 (2004) 71–79. doi:10.1016/j.msea.2004.03.064.

[84] T. Zhu, J. Li, A. Samanta, A. Leach, K. Gall, Temperature and Strain-Rate Dependence of Surface Dislocation Nucleation, Phys. Rev. Lett. 100 (2008) 25502. doi:10.1103/PhysRevLett.100.025502.

[85] X. Huang, N. Hansen, N. Tsuji, Hardening by Annealing and Softening by Deformation in

Nanostructured Metals, Science (80-.). 312 (2006) 249–251. doi:10.1126/science.1124268.

[86] O. Renk, A. Hohenwarter, K. Eder, K.S. Kormout, J.M. Cairney, R. Pippan, Increasing the strength of nanocrystalline steels by annealing: Is segregation necessary?, Scr. Mater. 95 (2015) 27–30. doi:10.1016/j.scriptamat.2014.09.023.

[87] L.J. Gibson, M.F. Ashby, The Mechanics of Three-Dimensional Cellular Materials, Proc. R. Soc. Lond. A. 382 1782 (1982) 43–59. doi:10.1098/rspa.1982.0088.

[88] K. Durst, B. Backes, O. Franke, M. Göken, Indentation size effect in metallic materials: Modeling strength from pop-in to macroscopic hardness using geometrically necessary dislocations, Acta Mater. 54 (2006) 2547–2555. doi:10.1016/j.actamat.2006.01.036.

[89] E.W. Hart, Theory of the tensile test, Acta Metall. 15 (1967) 351–355. doi:10.1016/0001-6160(67)90211-8.

[90] V. Maier, A. Leitner, R. Pippan, D. Kiener, Thermally Activated Deformation Behavior of ufg-Au: Environmental Issues During Long-Term and High-Temperature Nanoindentation Testing, JOM. (2015) 1–11. doi:10.1007/s11837-015-1638-7.

[91] A.W. Thompson, Yielding in nickel as a function of grain or cell size, Acta Metall. 23 (1975) 1337–1342. doi:10.1016/0001-6160(75)90142-X.

[92] F. Ebrahimi, G.R. Bourne, M.S. Kelly, T.E. Matthews, Mechanical properties of nanocrystalline nickel produced by electrodeposition, Nanostructured Mater. 11 (1999) 343–350. doi:10.1016/S0965-9773(99)00050-1.

[93] X. Feaugas, H. Haddou, Grain-size effects on tensile behavior of nickel and AISI 316 L stainless steel, Metall. Mater. Trans. A. 34 (2003) 2329–2340. doi:10.1007/s11661-003-0296-5.

[94] A. Godon, J. Creus, S. Cohendoz, E. Conforto, X. Feaugas, P. Girault, C. Savall, Effects of grain orientation on the Hall-Petch relationship in electrodeposited nickel with nanocrystalline grains, Scr. Mater. 62 (2010) 403–406. doi:10.1016/j.scriptamat.2009.11.038.

[95] C.E. Carlton, P.J. Ferreira, What is behind the inverse Hall-Petch effect in nanocrystalline materials?, Acta Mater. 55 (2007) 3749–3756. doi:10.1016/j.actamat.2007.02.021.

[96] U.K. Vashi, R.W. Armstrong, G.E. Zima, The hardness and grain size of consolidated fine tungsten powder, Metall. Trans. 1 (1970) 1769–1771. doi:10.1007/BF02642027.

[97] J. Wehrs, G. Mohanty, G. Guillonneau, A. Taylor, X. Maeder, D. Frey, L. Philippe, S. Mischler, J. Wheeler, J. Michler, Comparison of In Situ Micromechanical Strain-Rate Sensitivity Measurement Techniques, JOM. (2015) 1–10. doi:10.1007/s11837-015-1447-z.

[98] R. Schwaiger, B. Moser, M. Dao, N. Chollacoop, S. Suresh, Some critical experiments on the strain-rate sensitivity of nanocrystalline nickel, Acta Mater. 51 (2003) 5159–5172. doi:10.1016/S1359-6454(03)00365-3.

[99] N. Krasilnikov, W. Lojkowski, Z. Pakiela, R. Valiev, Tensile strength and ductility of ultra-fine-grained nickel processed by severe plastic deformation, Mater. Sci. Eng. A. 397 (2005) 330–337. doi:10.1016/j.msea.2005.03.001.

[100] B. Yang, Grain size effects on the mechanical behaviour of polycrystalline nickel from micro to nanoscale, Universität des Saarlandes, 2006.

[101] G.B. Rathmayr, A.Hohenwarter, R. Pippan, Influence of grain shape and orientation on the mechanical properties of high pressure torsion deformed nickel, Mater. Sci. Eng. A. 560

(2013) 224–231. doi:10.1016/j.msea.2012.09.061.

[102] K. Levenberg, A method for the solution of certain non-linear problems in least squares, Q. Appl. Math. 2 (1944) 164–168. doi:10.1090/qam/10666.

[103] D.W. Marquardt, An Algorithm for Least-Squares Estimation of Nonlinear Parameters, J. Soc. Ind. Appl. Math. 11 (1963) 431–441. doi:10.1137/0111030.

[104] J. Alkorta, J.M. Martínez-Esnaola, J.G. Sevillano, Critical examination of strain-rate sensitivity measurement by nanoindentation methods: Application to severely deformed niobium, Acta Mater. 56 (2008) 884–893. doi:10.1016/j.actamat.2007.10.039.

[105] A.T. Jennings, J. Li, J.R. Greer, Emergence of strain-rate sensitivity in Cu nanopillars: Transition from dislocation multiplication to dislocation nucleation, Acta Mater. 59 (2011) 5627–5637. doi:10.1016/j.actamat.2011.05.038.

[106] Y.M. Wang, A. V Hamza, E. Ma, Temperature-dependent strain rate sensitivity and activation volume of nanocrystalline {N}i, Acta Mater. 54 (2006) 2715–2726. doi:10.1016/j.actamat.2006.02.013.

[107] S.H. van den Brink, A. van den Beukel, P.G. McCormick, Strain rate sensitivity and the portevin-le chatelier effect in Au-Cu alloys, Phys. Status Solidi. 30 (1975) 469–477. doi:10.1002/pssa.2210300205.

[108] M.J. Mayo, W.D. Nix, A micro-indentation study of superplasticity in Pb, Sn, and Sn-38 wt% Pb, Acta Metall. 36 (1988) 2183–2192. doi:10.1016/0001-6160(88)90319-7.

[109] H.S. Leipner, D. Lorenz, A. Zeckzer, H. Lei, P. Grau, Nanoindentation Pop-In Effect in Semiconductors, Phys. B Condens. Matter. 308–310 (2001) 446–449. doi:10.1016/S0921-4526(01)00718-9.

[110] S.E. Grillo, M. Ducarroir, M. Nadal, E. Tournié, J.-P. Faurie, Nanoindentation of Si, GaP, GaAs and ZnSe single crystals, J. Phys. D Appl. Phys. 36 (2003) 5–9. doi:10.1088/0022-3727/36/1/102.

[111] T.H. Fang, W.J. Chang, C.M. Lin, Nanoindentation and nanoscratch characteristics of Si and GaAs, Microelectron. Eng. 77 (2005) 389–398. doi:10.1016/j.mee.2005.01.025.

[112] A. Clausner, F. Richter, Determination of yield stress from nano-indentation experiments, Eur. J. Mech. - A/Solids. 51 (2015) 11–20. doi:10.1016/j.euromechsol.2014.11.008.

CHAPTER 2

Publication A

Interface dominated mechanical properties of ultra-fine grained and nanoporous Au at elevated temperatures

A. Leitner[1], V. Maier-Kiener[2], J. Jeong[3], M.D. Abad[4], P. Hosemann[4], S.H. Oh[5], D. Kiener[1]

Acta Materialia 121 (2016) 104-116

[1] Department Materials Physics, Montanuniversität Leoben, Austria
[2] Department Physical Metallurgy and Materials Testing, Montanuniversität Leoben, Austria
[3] IBS Center for Integrated Nanostructure Physics, Sungkyunkwan University, Republic of Korea
[4] Department of Nuclear Engineering, University of California, Berkeley, USA
[5] Department of Energy Science, Sungkyunkwan University, Republic of Korea

A - Abstract

Modern design and engineering of highly efficient devices and machines demand innovative materials to satisfy requirements such as high strength at low density. The purpose of this study was to oppose the mechanical properties and deformation behavior of ultra-fine grained Au to those of nanoporous Au, to study the influence of different types of interfaces. Microstructural investigations of the foam surrendered a ligament size of ~ 100 nm which themselves consist of 70 nm grains in average, while the ultra-fine grained gold features a mean grain size of 325 nm. Nanoindentation lend itself as a convenient technique to obtain material properties at ambient as well as high temperature conditions. In this work, a substantial indentation test series was performed in order to determine hardness, Young's modulus, strain-rate sensitivity and activation volume at room and elevated temperatures up to 300 °C. On account of the small characteristic dimensions, high hardness values were noted for both materials, which rapidly drop at elevated temperature. Additionally, an enhanced strain-rate sensitivity accompanied by low activation volumes was determined at room temperature, which further increased at elevated temperatures. This behavior is associated with thermally activated interactions between dislocations and interfaces. For nanoporous Au, due to the presence of free surfaces, a considerable increase of hardness was observed upon annealing. This can be attributed to a reduced number of mobile dislocations in the material after annealing, as supported by implemented porosity maps on indent cross-sections, showing distinct differences for tests at varying temperature.

A – Introduction

Metals with characteristic structure dimensions approaching the sub-micron scale are known to differ in their mechanical properties compared to their coarse-grained counterparts, especially due to the restrained state of dislocations. This issue, first described by Hall and Petch [1, 2], in addition with lately observed hardening effects caused by annealing [3, 4], put this material classes such as ultra-fine grained (UFG) and nanocrystalline (NC) materials in the spotlight of various fields of applications. Grain boundary strengthening provides the opportunity to increase the strength without undesired effects on the endurable strain of the metal, and thus is widely used for high-performance components. Light-weight constructions on the other hand, are considered to be the key to high efficiency and energy-saving technologies, which are indispensable in the 21st century. Hence, it seems natural to investigate not only UFG bulk materials, but in particular nanoporous (NP) structures which combine the assets of small structure dimensions and light-weight materials. It is not surprising that studies on NP Au revealed exceptional high ligament strengths at room temperature [5-10], since it is well known that strength increases with decreasing structure size, often demonstrated for nano-pillars or nanowires [11-15]. Recently, there was also evidence that NP materials possess a high radiation resistance resulting from self-healing mechanisms [16], making them suitable for nuclear applications. The governing deformation mechanisms in such NP structures, in particular at elevated temperatures, are thus of great interest in order to understand their mechanical behavior.

Face-centered cubic (fcc) UFG metals are reported to exhibit multiple deformation mechanisms, such as dislocation emission from grain boundaries [17], likewise grain boundary diffusion or micro shear banding can play a crucial role [18, 19], and grain boundary sliding is known to occur at high temperature (HT) [18, 20, 21]. The dominating mechanism can be indicated by a noticeable strain-rate sensitivity corresponding to low activation volumes [22-29]. Certainly, this raises the question whether the type of interface exerts a significant influence on the mechanical behavior, since the models of the mentioned deformation mechanisms are based on bulk materials with a high amount of grain boundaries. Therefore, the present study will investigate the different behavior of the NP and UFG state of Au to contrast grain boundaries with free surfaces, at RT as well as elevated temperatures up to 300 °C. Nanoindentation proves to be an optimal technique to extract mechanical properties [30], but also rate-dependent parameters, such as the strain-rate sensitivity *m* and the activation volume *V** [22, 31-34], accompanied by minimal material consumption for testing.

Through a unique fabrication route by powder compaction and severe plastic deformation using High Pressure Torsion (HPT) temperature-stable UFG Au bulk samples as well as a NP Au foam with well-defined microstructure will be produced. Additionally, the deformation morphology will be unfolded by Focused Ion Beam (FIB) cross sections of indents, for the first time allowing to verify the dominating deformation mechanisms by the appearance of the plastic deformation underneath an indent. This will enable us to demonstrate that the interface type as well as the temperature have a major impact on the mechanical behavior and rate-dependent properties of nanostructured gold.

A - Experimental details

Sample fabrication and microstructure analysis

For this study, spherical Au powder (Alpha Aesar GmbH & Co KG) with a purity of 99.96 % and an average particle size of 5.5 - 9.0 µm was used as a base material. The powder was poured into a copper ring, which in turn was glued on an HPT anvil. Subsequently the powder was consolidated and deformed via HPT [35, 36] to produce UFG Au disks with a diameter of 8 mm and a height of 0.8 – 1 mm. Likewise, a Au/Fe powder mixture (50/50 vol.%) was densified to create a nanostructured composite [37-39], where the spherical Fe powder (obtained from Merck KGaA) features a purity of 99.9 % with particle sizes < 10 µm. Since the formation of supersaturated phases after extensive severe plastic deformation has been observed [38], all samples were annealed at 300 °C for 1 h in a vacuum furnace (SERIES XRETORT, Xerion Advanced Heating Ofentechnik GmbH, Germany) to allow a reduction of the forced mixing. The pure UFG Au samples were annealed the same way in order to maintain comparable material conditions for both material types.

Subsequently, the HPT disks were ground from one side to 0.4 - 0.5 mm thickness to eliminate surface artefacts and reach the most homogenous zone of the sample. Next, Au/Fe specimens underwent a selective etching process to remove the Fe and obtain a novel nanoporous Au structure, similar to a procedure recently described to produce NP Cu [37]. For this purpose, a 5 wt.% hydrochloric acid served as an etchant, where the Fe in the composite was entirely dissolved after 24 h at 55 °C, leaving behind a Au foam with ~ 50 % porosity. Finally, UFG and NP samples were annealed at 100 °C, 200 °C and 300 °C to study the microstructure stability.

The resultant microstructures were characterized using a scanning electron microscope (SEM; LEO type 1525, Carl Zeiss GmbH, Germany) combined with Electron Backscatter Diffraction (EBSD, EDAX Inc. Mahwah, USA). For the latter a 15 ° misorientation angle was set as threshold to differentiate low-angle from high-angle grain boundaries. An ultra-fine grained structure was revealed for compact Au samples with an average grain size of about 325 nm at room temperature (RT) (Fig. 1 a). As evident from Fig. 1 a) to d) and Fig. 2 a), minor grain coarsening can be observed after high temperature (HT) annealing up to 300 °C. Energy dispersive X-ray (EDX) spectra exhibit that the UFG Au disks contain small amounts of Cu (< 1 at.%), which most likely originates from the copper ring used in the production process via powder consolidation.

SEM micrographs illustrate the NP topology of the Au foam after tests at the inscribed temperatures (Fig. 1 e) – h)). The foam features a porosity of approximately 50 % and ligaments with an average diameter of about 100 nm at RT. Using EBSD, it is shown that the ligaments themselves consist on average of approximately 70 nm diameter small grains with a narrow size distribution, see Fig. 1 i). Information of the black area was not considered, since the image quality of the Kikuchi patterns in this zone falls below a critical value of 35 %, and therefore an accurate determination of the grain structure could not be guaranteed. While a slight coarsening of grains takes place upon annealing, the ligament diameter remains rather unaltered (Fig. 1 e) - l)), evaluated quantitatively in Fig. 2. The grain size of the foam may exceed the ligament's diameter, as intersections where ligaments converge are not considered in the analysis of the diameter. Several EDX scans performed at different areas show that despite the preceded annealing up to 5.5 at.% Fe are still remaining within the Au matrix.

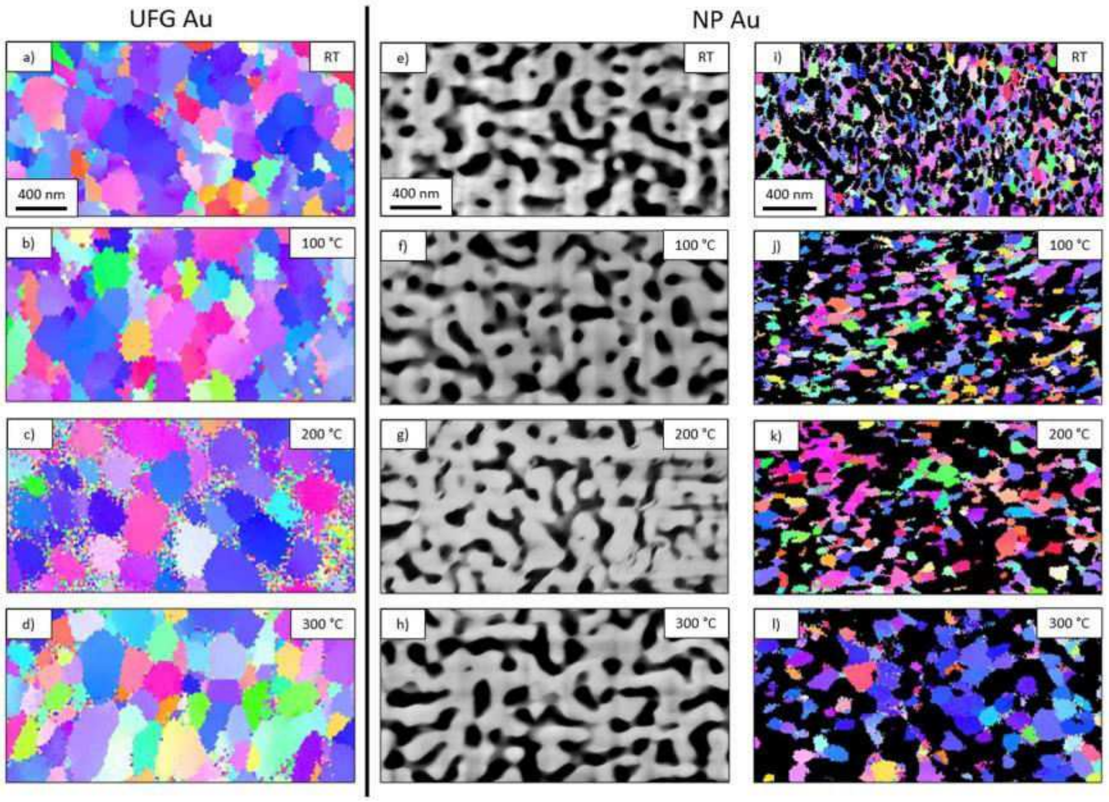

Fig. 1. Microstructural characteristics at RT and after annealing at the inscribed temperature up to 300 °C. EBSD scans, represented in a) - d) reveal the grain size and structure of UFG Au. Images e) - h) display SEM micrographs of the ligaments of NP Au and i) - l) the EBSD data of the foam. Scale bar is the same for all images.

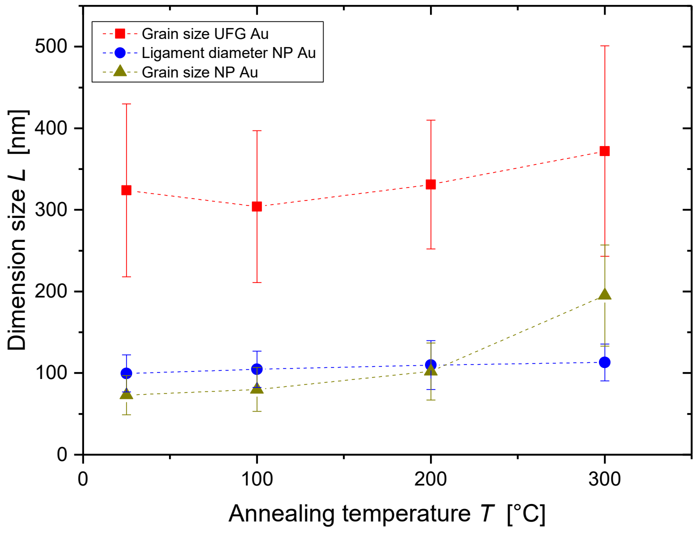

Fig. 2. Evolution of grain size and ligament diameter for UFG Au and NP Au upon annealing to 300 °C.

Nanoindentation

Experimental Setup

Depth sensing nanoindentation enables the determination of fundamental mechanical properties and parameters for the indication of the predominating deformation mechanism expending minimal material volumes. The experiments were performed using a Micro Materials NanoTest Platform 3 (Micro Materials, UK) nanoindentation device including a hot stage option. Common Berkovich tips were used, made from diamond for room temperature (RT) and from cubic boron nitride (cBN) for elevated temperature testing. Both tip materials are well-suited for HT testing since no tip/sample interaction is expected [40]. Calibrations of the indenter tips were conducted on fused silica according to the method proposed by Oliver and Pharr [30] to maintain an accurate area function and machine compliance. For high temperature measurements the sample was fixed with a ceramic adhesive (Omegabond 600, Omega Engineering Inc., Stamford, USA), likewise a reference sample was mounted. The indenter cabinet was purged with a reductive protective gas (hydrogen / argon mixture) in order to avoid any oxidational effects on the material. In addition to the thermocouples preinstalled on the nanoindenter device, an additional one was externally mounted on the surface of the reference sample to double-check the temperature conditions as close to the sample as possible.

A Nanoindenter G200 (Keysight Technologies, USA) featuring a continuous stiffness measurement (CSM) option was used to double-check the obtained RT indentation values by conducting CSM constant strain-rate (0.05 s^{-1}) measurements and nanoindentation strain-rate jump tests [32].

Testing procedure

Displacement controlled (DC) runs with proportional load ramps (equivalent to a constant strain-rate) with 5 s dwell time at maximum load were performed to obtain the hardness (H) and reduced modulus (E_r) following the method proposed by Oliver and Pharr [30]. In addition, load controlled (LC) tests with longer dwell times of 200 s were executed to determine the strain-rate sensitivity m and activation volume V^*, which were inferred from relaxation data of the hold segment, recently elaborately described by other authors [22, 33, 37, 41]. Exemplary load-displacement curves are displayed in the appendix (Fig. A1). At least 10 indents were performed for each condition, and an overview of the testing temperature profile is depicted in Fig. 3. Starting at RT and further increasing temperature in steps of 100 °C to 300 °C corresponds to a homologue temperature range from 0.22 to 0.43. Supplementary RT measurements were conducted prior and after HT experiments in order to check for changes of the material or setup, respectively.

A penetration depth of 2000 nm for NP Au was supposed to be reasonable to comprise a sufficient number of ligaments. For UFG Au the maximum depth was reduced to 1000 nm, still covering about 100 grains in the tested volume. Indentation tests where thermal drift exceeded ± 0.3 nm/s were identified and not considered in the later data analysis.

The reference measurements on the G200 nanoindentation device were conducted in DC mode with CSM to 2000 nm displacement into the surface to obtain mechanical properties at RT. In order to obtain *m* and *V**, strain rate jump tests were performed between strain-rate levels of 0.05 s^{-1}, 0.01 s^{-1} and 0.005 s^{-1}.

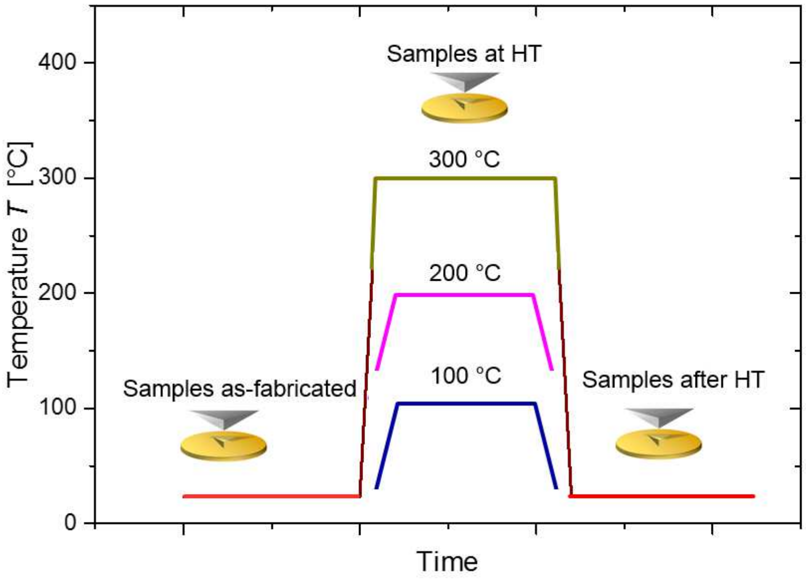

Fig. 3. Overview of the temperature profile for nanoindentation testing. Indenter symbols imply that the test was carried out at the assigned condition.

Analysis

The hardness and Young's modulus were obtained following the conventional procedure first described by Oliver and Pharr [30]. The strain-rate sensitivity *m* for a constant temperature *T* can be determined by rewriting the well-known power-law relation between strain-rate $\dot{\varepsilon}$ and stress σ [28, 42] to

$$m = \left(\frac{\partial \ln H}{\partial \ln \dot{\varepsilon}}\right)_T, \qquad (1)$$

since *H* is proportional to the indentation flow stress $\sigma_{f,i}$ via the constraint factor $H = \sigma_{f,i} \cdot C^*$. From this, it follows that the slope of the double logarithmic Norton plot is the reciprocal of *m* and hence can be plotted in dependence of the corresponding indentation flow stress. At a constant load, the resultant time / displacement curve during the dwell period can provide the required data [22, 33], see Fig. 4.

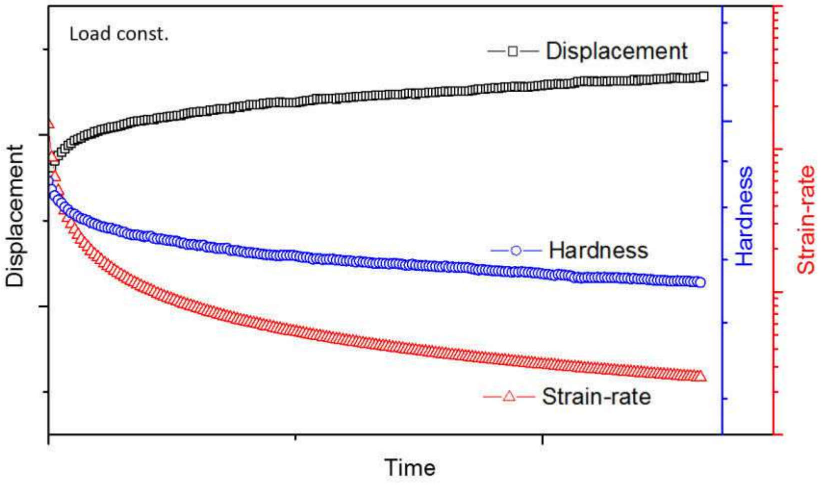

Fig. 4. Time profile of displacement, hardness and strain-rate during a dwell segment, used to determine *m* and *V**.

Last but not least, the activation volume *V** can be determined based on the fundamental thermodynamic relation for the Gibbs free energy

$$V^* = -\left(\frac{\partial \Delta G}{\partial \tau}\right)_T . \tag{2}$$

For thermally activated deformation mechanisms and by taking into account the von Mises yield criterion, the activation volume may be written as [24]

$$V^* = C^* \cdot \sqrt{3} \cdot k_b \cdot T \cdot \frac{1}{m \cdot H} . \tag{3}$$

Frequently, *V** is divided by b^3, with *b* being the Burgers vector of the tested material. In the case of gold $b = 2.884 \cdot 10^{-10}$ nm.

For porous media, Gibson and Ashby established a relation between macroscopic foams and bulk properties [43], which are often applied to microscopic foams too, even though their validity for ultra-fine porous or nanoporous foams with higher densities is still under debate [8, 10, 44-46]. These equations allow to calculate the flow stress and Young's modulus of the ligaments based on the bulk properties:

$$\sigma_f^* = C_1 \cdot \sigma_{f,s} \cdot \left(\frac{\rho^*}{\rho_s}\right)^p , \quad (4), \qquad E^* = C_2 \cdot E_s \cdot \left(\frac{\rho^*}{\rho_s}\right)^q , \quad (5),$$

with $\sigma_{f,s}$ as the flow stress, E_s the Young's modulus and ρ_s the density of a solid bulk sample. The flow stress σ_f^*, Young's modulus E^* and density ρ^* refer to the porous foam. C_1, C_2, *p* and *q* are constants ascribed to cell geometry and cell deformation ($C_1 = 0.3$, $C_2 = 1$, $p = 1.5$, $q = 2$) [43].

For NP Au the value of *ν* has controversially been discussed in the past. While in some studies *ν* is assumed to be zero [5, 9, 10], experiments of several other authors indicate an average

ν of about 0.2 [6, 47, 48]. Lately, this value was confirmed again in an extensive study of tension and compression tests of nanoporous Au [8, 47], thus $\nu = 0.2$ will be used in the present work. Eventually, C^* strongly depends on ν and changes from 1 ($\nu = 0$) to about 2.5 ($\nu = 0.2$) [43], ending up in lower indentation flow stresses. Thus, all presented stress data on NP Au can be regarded as a lower bound.

Implementation of porosity maps

Since the stress field beneath an indenter tip is not homogenous, the occurring deformation is not necessarily self-evident either. Cross-sections of indents were prepared with a focused ion beam (FIB, LEO-1540XB, Carl Zeiss GmbH, Germany) to examine the deformation appearance beneath the surface. The local densification of NP Au samples was analyzed through porosity maps. For this purpose, a python script was written to execute the following necessary steps. At first the SEM images (8-bit greyscale) are converted to binary b/w images, in which the ratio of black and white pixels can be ascribed to the porosity of the foam (Fig. 5 a) & b)). To validate that an insensitive binarization threshold was used and the porosity maps display a realistic structure, two markers having 0 % and 100 % porosity, respectively, were artificially added in an image, which should be clearly visible in the final map (Fig. 5 c)). Subsequently, a 500 nm x 500 nm box scans the image for local porosity with a step size of around 10 nm (corresponding to 1 px) to gain maximum resolution (Fig. 5 d)). This results in about three million porosity data points per image. Those are written in a 2-dimensional array, corresponding to the center coordinates of the of the analysis box, from which a densification colormap is created (Fig. 5 e)). Since the actual densification and not the inhomogeneity of the foam itself should be displayed, a deviation of ± 5 % around the mean relative density (measured in an unaffected zone) is displayed in white. Notably, an outer frame of half the box width, indicated in Fig. 5 c), cannot be analyzed and is therefore neglected. Finally, the original image is automatically aligned with the porosity map to avoid any mismatch. The result in Fig. 5 e) confirms that the expected bulk porosity of 50 %, as well as variations of the porosity, in this case the artificial markers, are detected properly. Therefore, this tool will be used later to analyze the densification of NP Au during nanoindentation at different temperatures. A more detailed study of the influence of numerical parameters such as threshold, box size and step size is given in appendix C.

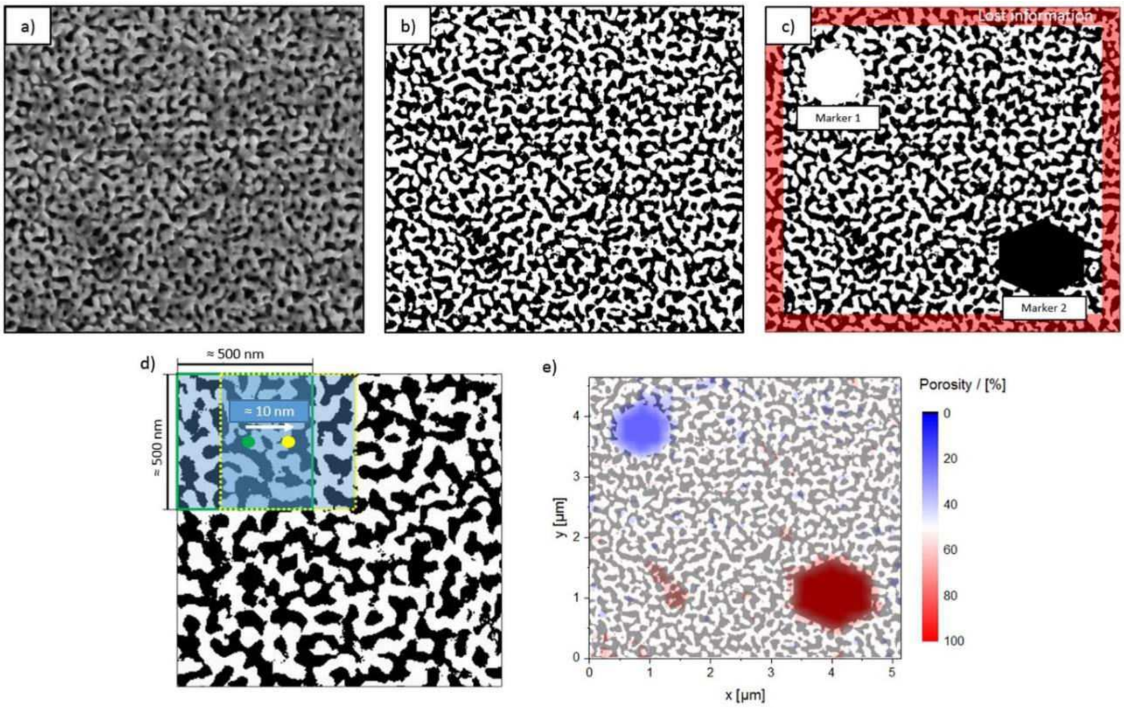

Fig. 5. Determination of localized porosity variations in NP Au. a) SEM micrograph of NP Au and b) binary image generated with python. c) Artificial markers and lost information at the outer border. d) Magnified visualization of the scanning procedure. e) Resulting porosity map with overlaid binary image which illustrates the local material porosity.

A - Results and analysis

Young's modulus and hardness

Fig. 6 demonstrates the trends of *H* and *E* as a function of temperature. For UFG Au the hardness shows a continuous decrease from *H* = 1.58 ± 0.04 GPa at RT to *H* = 0.22 ± 0.01 GPa at 300 °C, which is conform to 14 % of the RT value. At ambient temperature the Young's modulus reaches a value of *E* = 88.0 ± 2.0 GPa, which eventually decreases to a level as low as *E* = 54.3 ± 2.7 GPa (62 % of E_{RT}) at 300 °C (Fig. 6 a)). When samples are measured again at RT after HT experiments, the Young's modulus appears unaltered, *H* on the other hand slightly decreases.

The initial hardness of NP Au measured prior HT experiments reveals values with low deviations (< 0.05 GPa) for every prepared disk itself, but varies between individual samples with *H* = 0.53 GPa ± 0.14 GPa. RT measurements after HT tests disclose a significant increased hardness of around 68 % to 0.89 GPa ± 0.06 GPa. The hardness reaches higher levels than the RT material after increasing the temperature to 100 °C, and then shows a continuous decrease up to 300 °C, where *H* reduces to 0.24 GPa ± 0.05 GPa. *E* was determined to be 28.9 GPa ± 4.0 GPa at RT, slightly increases at 100 °C but then reverses the trend until finally ending up at 23.9 GPa ± 1.2 GPa at 300 °C, illustrated in Fig. 6 b). Just as for *H*, an increase of *E* was observed when tests were conducted again at ambient temperatures. The origin of this increase after annealing will be discussed later.

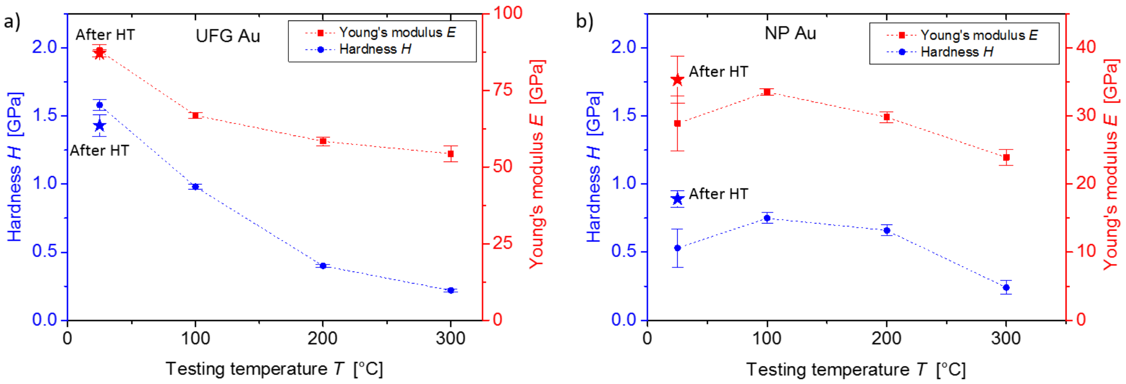

Fig. 6. Hardness and Young's modulus in the tested temperature range for both sample types a) UFG Au and b) NP Au. Star symbols mark the corresponding values measured again at RT after HT testing.

Strain-rate sensitivity and activation volume

As a matter of clearness, data of representative indents for each temperature condition are plotted in Fig. 7, instead of whole data sets. It is common practice to deduce deformation rate-dependent parameters from Norton plots (Fig. 7 a) & d)), resulting from equation (1). The graphs show that while the load is held constant, the tip sinks deeper into the material. As a consequence, the hardness and indentation strain-rate are reduced, as depicted in Fig. 4.

RT experiments on UFG Au (Fig. 7 a)) result in *m* values reaching from 0.06 up to 0.16 with rising dwell time and hence decreasing $\sigma_{f,i}$. When the samples are measured at HT, *m* shifts to slightly higher numbers accompanied by an expected reduction of $\sigma_{f,i}$, respectively (Fig. 7 b)). At 300 °C the maximum *m* value increases to 0.25. At RT *V** shows rather low numbers of less than 10 b^3 (Fig. 7 c)). *V** increases with ascending temperature up to 70 b^3 and becomes more independent of the indentation flow stress.

Aside from the mechanical strength of NP Au, *m* and *V** show a slight change too after the material was exposed to elevated temperatures. Results of tests at RT after annealing were obtained from 30 s dwell periods in contrast to the other tests, which were obtained from 200 s hold periods. For a better comparability, the first 30 s of the 200 s dwell data were marked with black lines in Fig. 7 d) - f). At ambient temperature, *m* extends from values starting at around 0.03 and eventually ends up at 0.12. *V** results in values in the range between 23 b^3 and 90 b^3 at RT (Fig. 7 f)). After annealing, one can identify from Fig. 7 e) that *m* decreases to slightly lower values and *V** alike. The increase in hardness after HT testing is recognized by the shift to higher indentation flow stresses.

High temperature experiments on the NP Au show a distinct rise of *m* compared to values after annealing. A further increase from 100 °C to 300 °C only causes a minor shift to higher *m* values, even though the flow stress decreases significantly (Fig. 7 e)). At 100 °C, *V** remains at a comparable level to RT, but clearly increases after further heating to 200 °C and 300^{-4} °C, eventually ending up in a maximum activation volume of 67 b^3.

The additional strain-rate jump tests carried out at RT are also indicated in Fig. 7, and those, considering the slightly higher strain-rates of $2.5 \cdot 10^{-2}\ s^{-1}$ to $5 \cdot 10^{-4}\ s^{-1}$, are in good accordance with the data measured by the creep analysis, as expected from previous studies [22, 41].

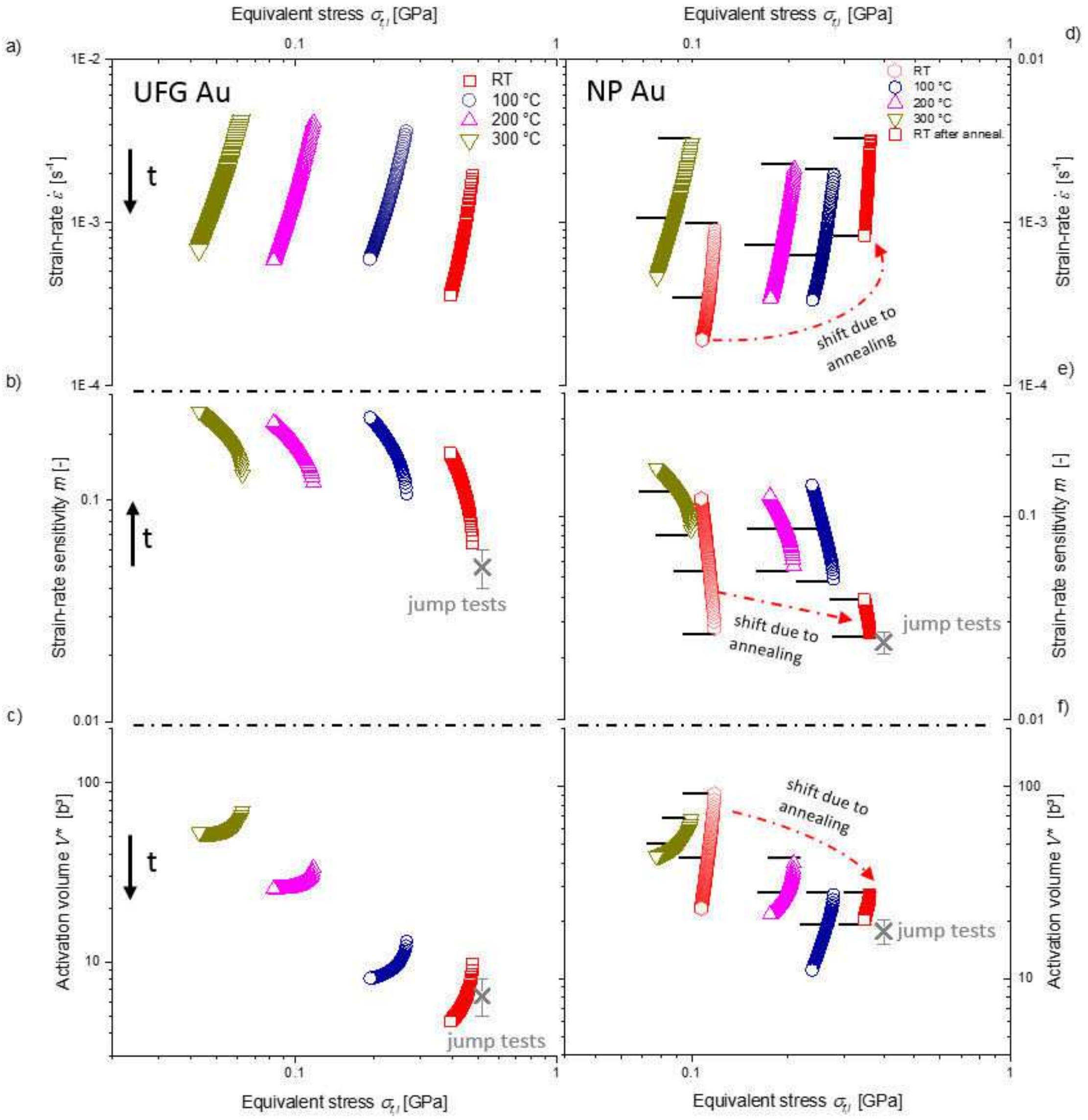

Fig. 7. Norton plot and corresponding diagrams of strain-rate sensitivity *m* and activation volume *V** in dependence of the equivalent indentation flow stress for indents at various temperatures for a) – c) UFG Au and d) – f) NP Au. In diagrams of NP Au, black lines indicate the first 30 s of the dwell time. A change in the RT behavior due to annealing of the foam is marked by a dashed-dot arrow. The increasing dwell time is marked by arrows on the left-hand side. Additional RT strain-rate jump tests are in good agreement.

A - Discussion

In this chapter we will at first compare our results of mechanical properties from static tests to existing literature data. After that, rate-dependent parameters will be discussed to draw conclusions regarding the governing dominant thermally activated deformation mechanism. Finally, we will visualize and examine the occurring deformation of NP Au by porosity maps and analyze their structure.

Mechanical properties

UFG Au

The RT hardness of UFG Au results in $H = 1.58 \pm 0.04$ GPa for the present 325 nm grain size material. In another study of HPT deformed UFG Au, a microhardness of 0.8 GPa was measured on samples with a mean grain size of 520 nm [49]. Hardness data obtained from nanoindentation of coarse grained (CG) Au shows values in the range between 0.8 GPa [50] and 2 GPa [51], whereat the latter value was measured at low indentation depths and will therefore underlie the indentation size effect [52]. However, considering the finer microstructure of the instant UFG Au due to the higher amounts of impurities resultant of the used powder route, well-known grain boundary hardening (Hall-Petch relation) [1, 2] and solid solution hardening are a plausible explanation for the higher hardness. Similar trends have been noted for C impurities in Ni [53]. The measured Young's modulus with a value of 88.0 GPa ± 2.0 GPa is reasonable, as literature data varies between 57 GPa and 87 GPa depending on the crystal orientation [54-56]. Compared to CG metals, the UFG structure is known for a rapid decrease of H at elevated temperatures [57]. This has been observed for Al and Cu [58] and also goes along with observations of the present study, where UFG Au reaches lower hardness values at 300 °C compared to CG Au measured by Beake *et al.* at 400 °C [50]. While a slight decrease of E over T was expected, the present trend appears anomalous compared to bulk data [54], where E drops less than 10 % in this temperature range. Such deviations could be associated with a deviating frame compliance during HT tests, a known problem of this setup [50], even though a conjunction with microstructural effects cannot be excluded [59].

NP Au

To the best knowledge of the authors, NP Au has never been produced through powder consolidation, HPT processing and subsequent selective etching so far. Through this study, it can be validated that the described proceeding is suitable to fabricate NP Au with a unique microstructure. In contrast to porous Au made from Au/Ag precursors, where grains comprise several ligaments or the foam even features a single crystalline structure [5, 8], the present foam differs in the grain size, which is about 70 nm in average when measured right after processing. For this reason, most of the ligaments contain more than one grain and consequently several grain boundaries. Therefore, it is not guaranteed that the values are non-restrictively comparable to literature data.

Following equation (4), one would estimate an indentation flow stress lower than 100 MPa for the foam, were the smaller structure size is already taken into account by applying the Hall-Petch law [1, 2, 23]. However, a far higher value of 212 MPa ± 56 MPa was measured in the present study, even further increasing to 356 MPa ± 24 MPa after annealing. Another approach is to rewrite equation (4) to solve for the flow stress of a corresponding bulk material. The flow stress of the ligament at RT prior HT tests results in 2.00 GPa ± 0.53 GPa. As mentioned before, after annealing the indentation flow stress increases to 3.36 GPa ± 0.22 GPa, a value approaching the theoretical strength of gold [56, 60]. Various other studies on NP Au, using nanoindentation technique, observed ligament strengths in the same order of magnitude [6, 7, 9]. However, it has been noted that NP materials endure far lower stresses in tensile tests [8, 61]. Tests with millimeter-sized samples on coarse grained and single crystalline nanoporous gold revealed a significant lower yield strength of about 440 MPa [8], thereby most probably testing the material flaws rather than the intrinsic ligament strength.

The noticeable increase of H after HT tests, despite minor coarsening of the microstructure, suggest that the deformation behavior has changed. Recent investigations on severe plastically deformed metals reveal that annealing can cause an increase in hardness [3, 4] due to annihilation of mobile dislocations and grain boundary relaxation [62]. Even though the relative increase of H is lower in the mentioned bulk studies (about 20 %), the high fraction of free surface could promote the dislocation annihilation effect and therefore lead to a more pronounced hardening of the NP compared to UFG metals [63].

Recalculating the Young's modulus of the ligaments by using equation (5) results in E = 116 GPa ± 16 GPa. This does not accord well with studies of other authors, whose values obtained from equation (6) are conform with bulk data, assuming the Ashby equations still hold as an accurate approximation [5-7]. Taking into account the remaining iron by applying the rule of mixture proposed by Voigt [64] gives an estimate that the Young’s modulus will be 10 % higher compared to pure Au. Moreover, small deviations of the actual porosity at the imprint site can also lead to significant errors, since porosity enters the equation quadratically.

Even though the determined data for modulus and yield strength show similar results compared with literature data [5-10], the analysis has to be critically reflected. One must keep in mind that the Ashby equations refer to macroscopic low-density foams and do not take into account the more complex situation of the nanometer-sized microstructure, and consequently different conditions for dislocation motion. Anyway, using the same equations as other authors previously certainly allows to compare values, even though it cannot be guaranteed that these lead to the actual intrinsic mechanical properties of the ligaments. Rate-dependent properties, as discussed in the next chapter, may allow to indicate more directly if there are any distinct changes of the deformation mechanisms.

Strain-rate sensitivity and activation volume

At this point, some critical remarks shall be made regarding the testing technique. Since the used nanoindentation devices is not capable of performing dynamic indentation techniques such as continuous stiffness measurement, the sink-in depth h_s cannot be obtained continuously during the dwell period, but is calculated from the stiffness determined at the end of the hold segment. Another consequence of not using a dynamic indentation technique is that measurements are prone to thermal drift errors [22, 41, 59, 65]. Even though a thermal drift rate is measured after 90 % unloading, there is no guarantee that the linear correction is conform to the actual drift during the test [41, 59]. However, due to the short dwell time and comparison of h_s after shorter hold times, major deviations should be eliminated.

UFG Au

In general, a decreasing structure size in fcc metals is linked to an increase of *m,* which is in turn attributed to boundary / dislocation interactions [22, 26, 28]. Controversial results were published concerning the temperature dependence of V^*, where a decrease [24, 66], as well as an increase [32, 67] was observed for UFG and nanocrystalline (NC) fcc materials at elevated temperatures.

The present study revealed increasing values for m and low values of V^* for UFG Au, which is in good accordance with studies on freestanding gold films [25, 29]. Activation volumes in this order of magnitude are often referred to dislocation nucleation and accommodation processes at grain boundaries [24, 27, 68]. Similar values, obtained from nanoindentation strain-rate jump tests, were noted for other UFG fcc metals as well, such as Al and Ni [22]. At elevated temperatures, climb may enable dislocations to overcome obstacles, additionally favored by the high amount of high angle grain boundaries due to the HPT process [69]. Eventually, this results in a rising V^* with increasing temperature. Moreover, dislocation nucleation is favored by the induced thermal energy at HT, and a reduction of sub-grains at HT (Fig. 1 a)-d)) will support the trend. In conclusion, V^* rises with increasing temperature and no profound changes of the deformation mechanism, e.g. towards diffusional deformation processes, are detected. For both materials supersaturated elements, Cu and Fe, respectively, do not show a significant influence on the rate-dependent properties. At least the impact of remaining dissolved elements is hardly assessable with the methods applied in this study.

NP Au

The obtained values for *m* are linked to dislocation plasticity, where interaction with interfaces lead to a more strain-rate sensitive behavior [22, 26, 28]. A recent atomistic simulation study of np Au demonstrated that perfect dislocations can occur even in ligaments with diameters down to 5 nm [70]. The reduction of *V** after HT tests fits into the concept that mobile dislocations may leave the material. Therefore, dislocations have to be nucleated either at free surfaces or from grain boundaries, both associated with low activation volumes [24, 27, 63, 68], while prior annealing abundant dislocations are present in the ligaments and consequently enable an easier deformation. With increasing temperature, the nucleation of dislocations as well as their movement is supported by introduced thermal energy [68], therefore *m* and *V** show increasing values. The slight grain coarsening with temperature, displayed in Fig. 1 and Fig. 2, will promote an increase too because slip distance and dislocation length will increase. Besides common mechanisms described for UFG Au, it is conceivable that enhanced surface diffusion could contribute to a more rate-dependent behavior. Unfortunately, comparable literature data is lacking, since some of the required parameters which would certainly affect the obtained properties, such as porosity, ligament diameter, purity and microstructure, differ from other studies.

A different appearance of the deformed zone underneath indents that were conducted at different conditions could support the preceding assumption. Thus, FIB cross-sections of various indents were prepared and analyzed as described previously to give an insight on the occurring deformation.

Interpretation of appeared deformation of NP Au

The porosity maps displayed in Fig. 8 reveal a different appearance of the plastically deformed volume in NP Au at different temperature conditions. A distinct plastic deformation and densification, respectively, at highly stressed positions is obvious for indents made prior HT tests (Fig. 8 a)), as one would expect for a foam. Through the densification the prescribed deformation can be accommodated in a small volume, resulting in a small plastic zone, as schematically depicted in Fig. 9 a). However, this behavior changes significantly once the sample was exposed to HT, since in this condition the dislocation density is reduced (Fig. 9 b)). Instead of the local densification underneath the tip as seen for prior HT indents, slightly denser zones are emerging in an extended range of the cross-section (Fig. 8 b)). This suggests that deformation is localized in weak ligaments which presumably fail by slip events. Instead of a global densification by dislocation plasticity, weak ligaments close to the tip fail at first. If there are no more favorable ligaments around, the plastic deformation will be pushed farther away from the tip, ending up in an extended plastic zone (Fig. 9 b)). Once the induced stress is sufficient to nucleate dislocations at the surface or at interfaces, these can contribute again to meet the prescribed deformation. These observations coincide well with the obtained numbers for m and V^* indicating dislocation mediated processes. The reduction of V^* after annealing suggests a shift from dislocation plasticity by pre-existing dislocations to a more nucleation controlled deformation behavior.

At higher temperatures a mixed state of deformation morphology was noticed (Fig. 8 c) & d)). At 100 °C the extended plastic zone can clearly be seen by densified areas afar from the tip, supporting the idea of an extended plastic zone in the annealed material. Densification occurs at some positions, but is not as homogenously distributed as in Fig. 8 a). Available thermal energy can support nucleation of dislocations, and therefore account for an easier deformation during the tests. Interestingly, at 300 °C, when values for V^* are again similar to those of the prior-RT indent, also the deformation appearance becomes more alike again. At this temperature, dislocations can easily be nucleated and are able to contribute to a collective densification of the foam underneath the tip (Fig. 8 d)). Therefore, the assumption that the mechanical properties of the foam are strongly dependent on the presence of dislocations, appears to be justified. In-situ TEM studies could support this hypothesis, however, the nanocrystalline microstructure of the foam requires alignment of several $\underline{g \cdot b}$ - conditions for each analyzed grain before and after, possibly even during annealing, which would be a very demanding task.

Contrary to the investigated UFG Au, where no distinct change of the deformation behavior was noted after annealing, these observations suggest that the high amount of free surfaces promotes an enormous hardening effect, given that the microstructure is temperature-stable as in the present case. Since no distinct coarsening of the ligaments was observed, it is unlikely that diffusional processes are the dominating deformation mechanism. Finally, we conclude that the deformation will mainly be governed by dislocation nucleation and accommodation processes for both materials, whereas the availability of free surfaces in the foam does not have a substantial impact on the rate-dependent parameters, or potentially the used method is not sensitive enough to assert clear differences. However, regarding the hardness of the materials the free surface plays a crucial role, since dislocations are able to leave the material during annealing. In contrast, in UFG Au the accommodation of dislocations will be restrained compared to NP Au since only grain boundaries are available as sinks for dislocations.

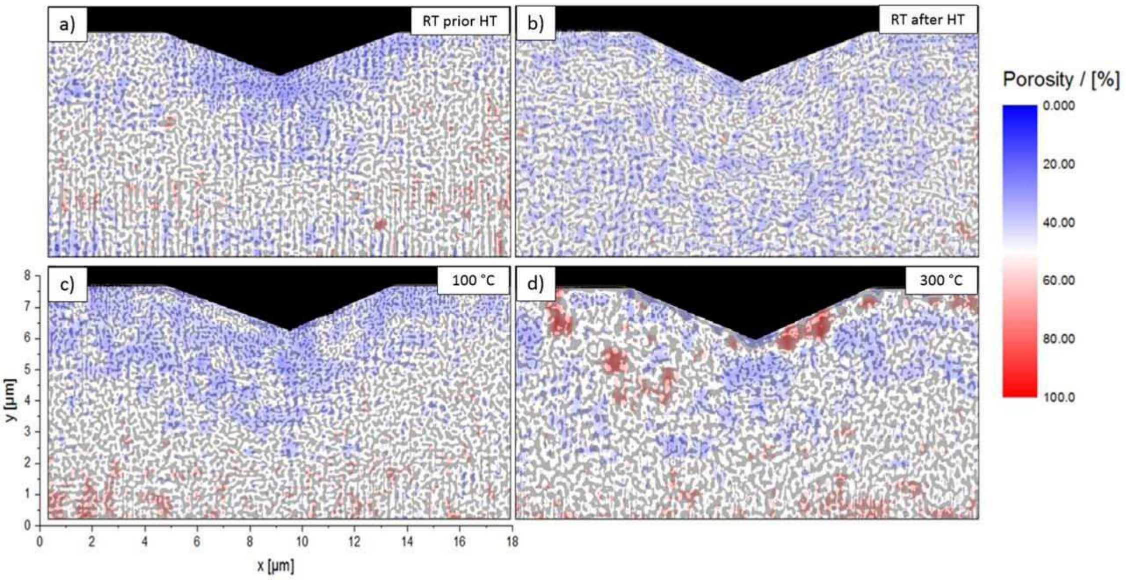

Fig. 8. FIB cross-sections of NP Au indents with overlapped porosity maps. a) Indent made right after processing at RT, b) RT indent after sample was exposed to elevated temperatures, c) indent made at 100 °C and d) at 300 °C.

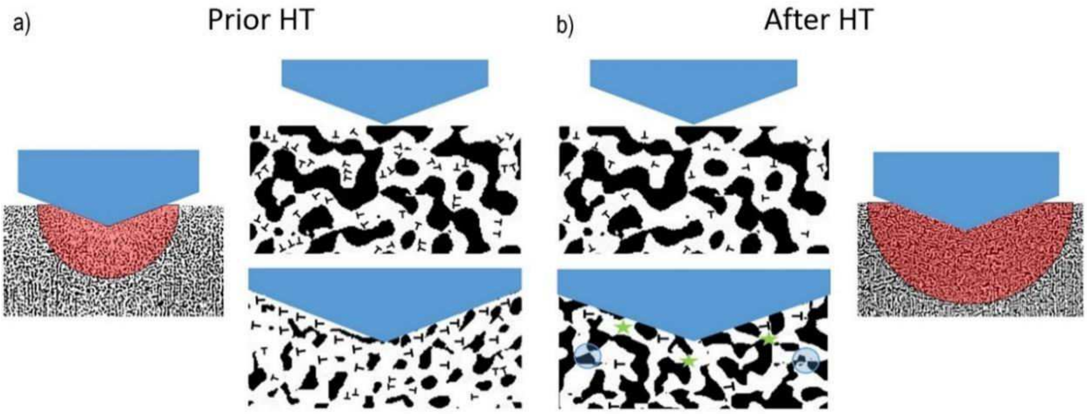

Fig. 9. Schematic illustration of different deformation mechanisms occurring in the NP Au. Slight transparent red semicircles indicate the occurring plastic zone. a) Prior to HT enough dislocations are present to evenly densify the ligaments during indentation. b) After HT testing, very limited densification was noted. This suggests more localized failure of ligaments by local slip (blue circles) and the need of dislocation nucleation (green stars) in order to comply with the imposed deformation.

A - Summary and conclusions

UFG and NP Au, both based on the same raw material, were fabricated via HPT and subsequently investigated regarding their temperature- and rate-dependent deformation mechanisms. UFG Au revealed an average grain size of 325 nm, while the Au-Fe composite-derived Au foam offers a unique microstructure with a ligament diameter of around 100 nm, consisting of about 70 nm small grains in average (Fig. 1 & 2). A slight coarsening of the microstructure (reduction of sub-grains in the UFG materials, grain growth in the ligaments) was noted after the samples were exposed to elevated temperatures. Nanoindentation tests were performed from RT up to 300 °C (corresponding to a homologue temperature range of from 0.22 to 0.43) in order to obtain hardness *H*, Young's modulus *E*, strain-rate sensitivity *m* and activation volume *V**. In combination with implemented local porosity maps of FIB cross-sections of indents in NP Au, the following conclusions were drawn:

- UFG Au reveals a high hardness of 1.58 ± 0.04 GPa at RT, which is due to grain boundary and solid solution hardening. An increasing temperature leads to a rapid reduction of *H* (Fig. 6a)), since climb of edge dislocations will be enhanced and favor easier deformation.
- For UFG Au, at RT *V** (5 b^3 - 10 b^3) is reduced and *m* (0.06 - 0.16) is clearly raised compared to conventionally grained materials, which can be associated with dislocation nucleation and accommodation processes. Both quantities increase at elevated temperatures (Fig. 7 a)–c)), which can be referred to thermally activated climb of edge dislocations. Additionally, thermal energy will favor dislocation nucleation.
- It was noted that the hardness of NP Au significantly increased (~ 68 %) after annealing (Fig. 6 b). This goes along with a different appearance of the deformed volumes underneath nanoindents (Fig. 8). Such behavior could be caused by a significant reduction of mobile dislocations upon annealing of the foam, as dislocations are able to leave the material at free surfaces.
- The activation volume of NP Au decreases after the heat treatment from 23 b^3 - 91 b^3 to 20 b^3 - 27 b^3 at RT, while *m* slightly decreases from 0.030 - 0.053 to 0.027 - 0.038, again attributed to the reduction of mobile dislocations. Dislocation nucleation at free surfaces or grain boundaries, respectively, is required in order to deform the material. At HT *m* and *V** rise as nucleation will be supported by thermal energy (Fig. 7 d)-f)). Diffusional processes seem not to be dominant since no distinct coarsening of the ligaments was noted.
- FIB cross-sections of NP Au prior and after HT testing (Fig 8 a) & b)) affirm that the hardness increase is accompanied by a changing deformation appearance, in turn supported by changing rate-dependent properties. Cross-sections of indents conducted at HT show a mixed state of deformation morphology (Fig. 8 c) & d)).
- In comparison, we conclude that the deformation of both tested materials is dominated by dislocation nucleation processes, whereas the presence of free surface in the NP Au leads to a similar rate dependent material behavior compared to UFG Au. In turn, the possibility for dislocations to leave the NP Au during annealing at free surfaces promotes a significant increase in hardness, shifting the deformation behavior from dislocation mobility controlled plasticity to a more nucleation-controlled mechanism.

Further investigations of the hardening effects will be necessary to understand the present processes in more detail. In particular, future in-situ TEM studies on the deformation behavior of NP Au could substantiate the details to the described dislocation behavior.

A - Acknowledgements

The financial support by the Austrian ‘‘Marshall-Plan Scholarships’’ and the Montanuniversität Leoben (AL) as well as the ‘‘Zukunftsfond Steiermark’’ (PN 6019-Nanofatigue) (VM, DK) are gratefully acknowledged. Parts of this work were funded by the Austrian Science Fund (FWF) via the international Project I 1020-N20. Further funding of the Styrian and the Tyrolean Provincial Government, represented by Steirische Wirtschaftsförderungsgesellschaft mbH and Standortagentur Tirol, within the framework of the COMET Funding Programme (837900, MPPE A7.19) is appreciated. The authors also acknowledge funding by the European Research Council under Grant number: 340185 (VM).

A - Appendix

A Figure A1 exemplary demonstrates the reproducibility of nanoindentation load-displacement curves for both materials, UFG Au and NP Au, at various temperatures.

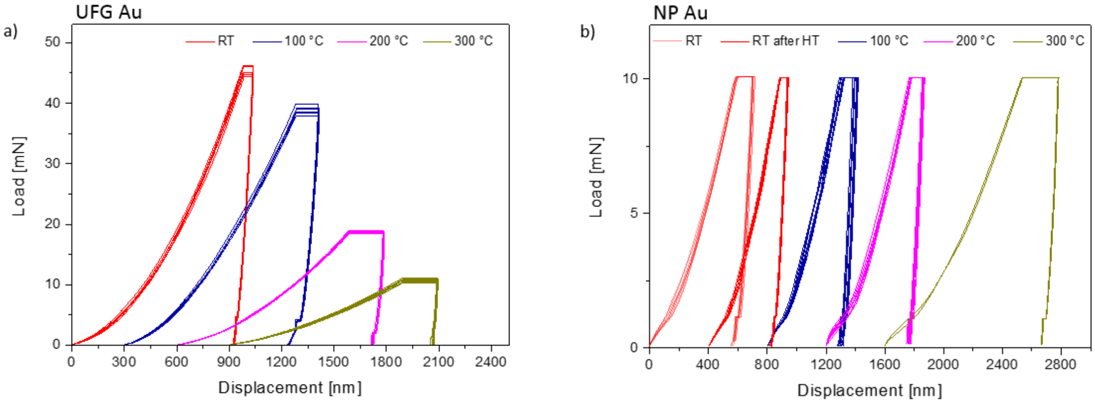

Fig. A1. Exemplary load-displacement curves obtained by nanoindentation. a) Displacement-controlled tests on UFG Au and b) load-controlled tests on NP Au from RT to 300 °C. Note the offset of the curves for a better presentability.

B Figure B1 shows the original SEM micrographs of the prepared FIB cross-sections which were used for creating the density maps in Fig. 8.

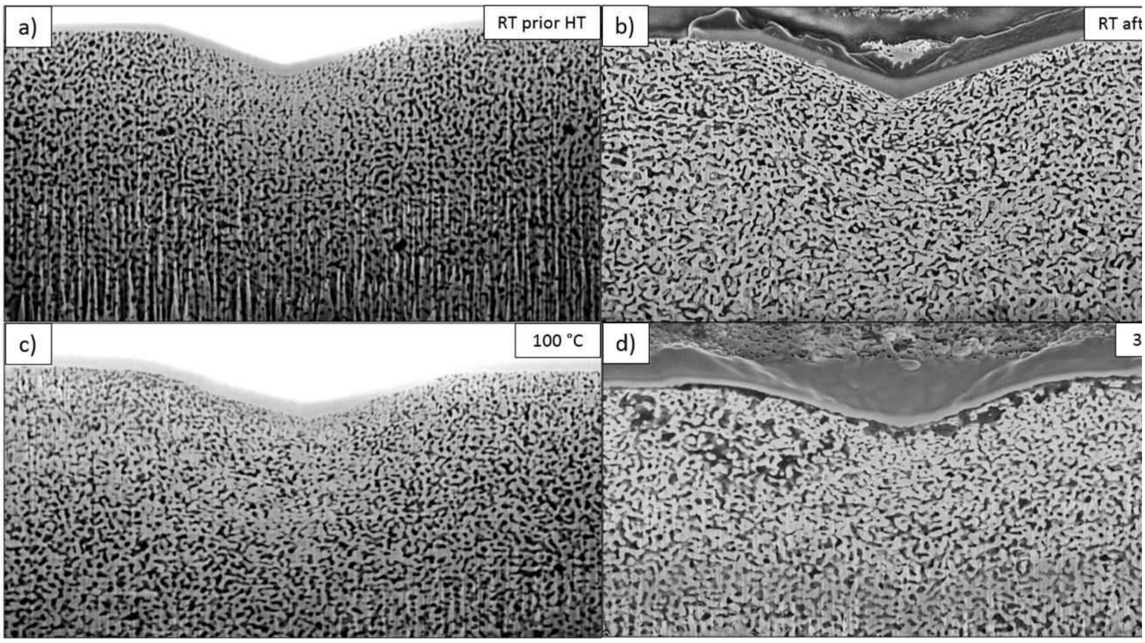

Fig. B1. a) - d) SEM images of the prepared FIB cross-sections of indents from different testing conditions.

C In the following a short overview of the influence of parameters used for creating porosity maps will be given. Three parameters are investigated: threshold, step size and box size (see Fig. 5 for details).

Threshold: The conversion from greyscale to a b/w image requires a threshold value which can be chosen in the interval of 0-255 due to the 8-bit greyscale format of the original image. Fig. C1 shows the development of the relative density in a selected box (see inset) in dependence of the threshold. Usually, the global density is at least known in the range of +/- 10 %. In our case, this would allow a threshold between 160 and 220. Fig C2 demonstrates that, regardless of the chosen threshold the procedure can still qualitatively differ denser from less dense regions, even though the absolute density level naturally varies. If the deviation of the porosity would be displayed relatively with respect to the determined mean porosity, all images would have the same appearance, but absolute values would be lost.

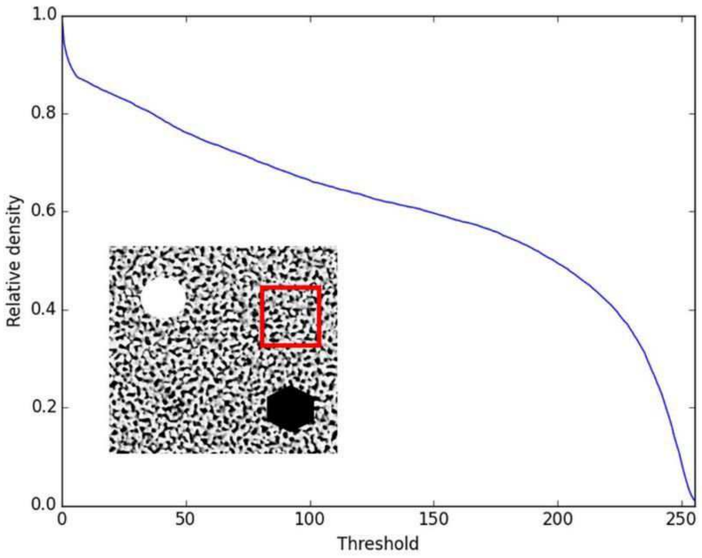

Fig. C1. Relative density in dependence of the threshold for the marked red box.

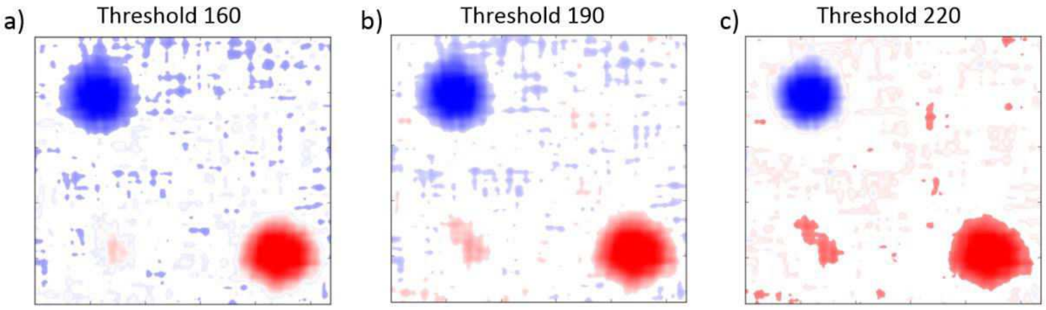

Fig. C2. Influence of threshold on obtained porosity maps. The maps depict absolute porosity values, which naturally vary with the threshold.

Box size: The used box should cover a representative area in regard to the microstructure. On the other hand, if size increases information and therewith local densification effects can be lost. For the present foam a box size of 500 nm was found sufficient to show the occurring densification zones. The influence of the box size on the porosity map appearance can be seen in Fig. C3.

Step size: The step size will decide on the resolution of the image, as to see in Fig. C4. The only advantage of larger step sizes is the lower processing time. Considering usual image sizes of around 2000 x 1500 px, this will end up in around 3,000,000 data points. Using a fast algorithm in the present study allows to obtain maximum resolution for all images, even though one can see that larger step sizes still give appropriate results.

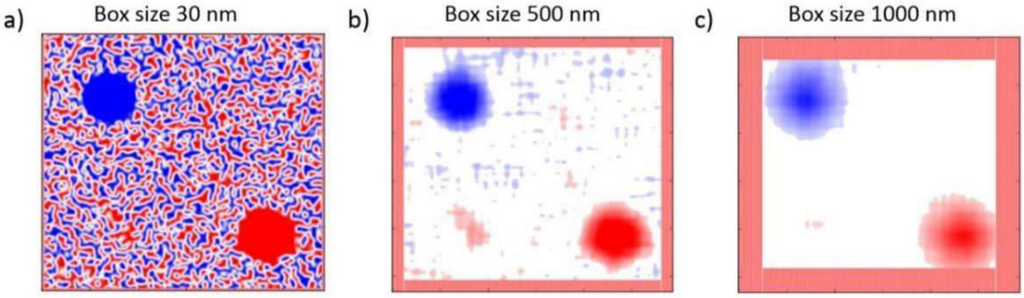

Fig. C3. Influence of the box size on obtained porosity maps. The zone of the indicated outer frame will be lost due to the box size.

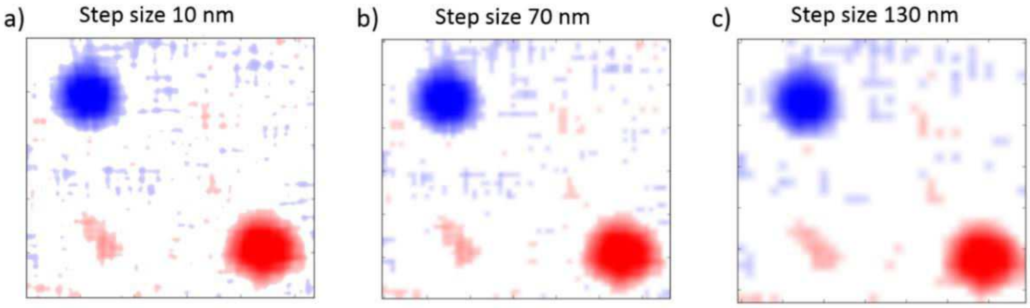

Fig. C4. Resultant porosity maps in dependence of the used step size. Resolution is worse for higher step sizes, but still gives an appropriate trend.

A - References

[1] E. O. Hall, The deformation and ageing of mild steel: Discussion of results, Proceedings of the Physical Society. Section B, 64 (9) (1951) 747-753.

[2] N. J. Petch, The cleavage strength of polycrystals, J. Iron Steel Inst., 174 (1953) 25–28.

[3] X. Huang, N. Hansen, N. Tsuji. Hardening by annealing and softening by deformation in nanostructured metals, Science, 312 (5771) (2006) 249–251.

[4] O. Renk, A. Hohenwarter, K. Eder, K.S. Kormout, J.M. Cairney, R. Pippan, Increasing the strength of nanocrystalline steels by annealing: Is segregation necessary? Scripta Materialia, 95 (0) (2015) 27–30.

[5] J. Biener, A. M. Hodge, A. V. Hamza, L. M. Hsiun, J. H. Satcher, Nanoporous Au: A high yield strength material, Journal of Applied Physics, 97 (2) (2005) 024301.

[6] C. A. Volkert, E. T. Lilleodden, D. Kramer, J. Weissmüller, Approaching the theoretical strength in nanoporous Au, Applied Physics Letters, 89 (6) (2006) 061920.

[7] D. Lee, X. Wei, X. Chen, M. Zhao, S. C. Jun, J. Hone, E. G. Herbert, W. C. Oliver, J. W. Kysar, Microfabrication and mechanical properties of nanoporous gold at the nanoscale, Scripta Materialia, 56 (5) (2007) 437–440.

[8] N. J. Briot, T. Kennerknecht, C. Eberl, T. J. Balk, Mechanical properties of bulk single crystalline nanoporous gold investigated by millimetre-scale tension and compression testing, Philosophical Magazine, 94 (8) (2014) 847–866.

[9] M. Hakamada, M. Mabuchi, Mechanical strength of nanoporous gold fabricated by dealloying, Scripta Materialia, 56 (11) (2007) 1003–1006.

[10] A. M. Hodge, J. Biener, J. R. Hayes, P. M. Bythrow, C. A. Volkert, A. V. Hamza, Scaling equation for yield strength of nanoporous open-cell foams, Acta Materialia, 55 (4) (2007) 1343–1349.

[11] D.M. Dimiduk, M.D. Uchic, T.A. Parthasarathy, Size-affected single-slip behavior of pure nickel microcrystals, Acta Materialia, 53 (15) (2005) 4065–4077.

[12] M. D. Uchic; P. Shade, D. M. Dimiduk. Plasticity of micrometer-scale single crytstals in compression, Annual Review of Materials Research, 39 (2009) 361-386

[13] C. A. Volkert, E. T. Lilleodden, Size effects in the deformation of sub-micron Au columns, Philosophical Magazine, 86 (33-35) (2006) 5567–5579.

[14] M. D. Uchic, D. M. Dimiduk, J. N. Florando, W. D. Nix, Sample dimensions influence strength and crystal plasticity, Science, 305 (5686) (2004) 986–989.

[15] J. R. Greer, W. D. Nix. Nanoscale gold pillars strengthened through dislocation starvation, Phys. Rev. B, 73 (2006) 245410.

[16] E. M. Bringa, J. D. Monk, A. Caro, A. Misra, L. Zepeda-Ruiz, M. Duchaineau, F. Abraham, M. Nastasi, S. T. Picraux, Y. Q. Wang, D. Farkas, Are nanoporous materials radiation resistant? Nano Letters, 12 (7) (2012) 3351–3355.

[17] Z. W. Wang, Y. B. Wang, X. Z. Liao, Y. H. Zhao, E. J. Lavernia, Y. T. Zhu, Z. Horita, T. G. Langdon, Influence of stacking fault energy on deformation mechanism and dislocation storage capacity in ultrafine-grained materials, Scripta Materialia, 60 (1) (2009) 52–55.

[18] I. Sabirov, Y. Estrin, M.R. Barnett, I. Timokhina, P.D. Hodgson, Tensile deformation of an ultrafine-grained aluminium alloy: Micro shear banding and grain boundary sliding, Acta Materialia, 56 (10) (2008) 2223–2230.

[19] R. W. Hayes, D. Witkin, F. Zhou, E. J. Lavernia, Deformation and activation volumes of cryomilled ultrafine-grained aluminum, Acta Materialia, 52 (14) (2004) 4259–4271.

[20] N. Q. Chinh, P. Szommer, Z. Horita, T.G. Langdon, Experimental evidence for grain-boundary sliding in ultrafine-grained aluminum processed by severe plastic deformation, Advanced Materials, 18 (1) (2006) 34–39.

[21] T. G. Langdon, Grain boundary sliding revisited: Developments in sliding over four decades, Journal of Materials Science, 41 (3) (2006) 597–609.

[22] V. Maier, B. Merle, M. Göken, K. Durst, An improved long-term nanoindentation creep testing approach for studying the local deformation processes in nanocrystalline metals at room and elevated temperatures, Journal of Materials Research, 28 (9) (2013) 1177–1188.

[23] Y. H. Chew, C. C. Wong, F. Wulff, F. C. Lim, H. M. Goh, Strain rate sensitivity and Hall-Petch behavior of ultrafine-grained gold wires, Thin Solid Films, 516 (16) (2008) 5376 – 5380.

[24] Y. M. Wang, A. V. Hamza, E. Ma, Temperature-dependent strain rate sensitivity and activation volume of nanocrystalline Ni, Acta Materialia, 54 (10) (2006) 2715–2726.

[25] B. Merle, M. Göken, Bulge fatigue testing of freestanding and supported gold films, Journal of Materials Research, 29 (2) (2014) 267–276.

[26] J. Chen, L. Lu, K. Lu, Hardness and strain rate sensitivity of nanocrystalline Cu, Scripta Materialia, 54 (11) (2006) 1913–1918.

[27] A. T. Jennings, J. Li, J. R. Greer, Emergence of strain-rate sensitivity in Cu nanopillars: Transition from dislocation multiplication to dislocation nucleation, Acta Materialia, 59 (14) (2011) 5627–5637. [28] Q. Wei, S. Cheng, K. T. Ramesh, E. Ma, Effect of nanocrystalline and ultrafine grain sizes on the strain rate sensitivity and activation volume: fcc versus bcc metals, Materials Science and Engineering: A, 381 (12) (2004) 71–79.

[29] R. D. Emery, G. L. Povirk, Tensile behavior of free-standing gold films. Part II. Fine-grained films, Acta Materialia, 51 (7) (2003) 2079–2087.

[30] W. C. Oliver, G. M. Pharr, An improved technique for determining hardness and elastic modulus using load and displacement sensing indentation experiments, Journal of Materials Research, 7 (6) (1992) 1564–1583.

[31] R. Schwaiger, B. Moser, M. Dao, N. Chollacoop, S. Suresh, Some critical experiments on the strain-rate sensitivity of nanocrystalline nickel, Acta Materialia, 51 (17) (2003) 5159–5172.

[32] V. Maier, K. Durst, J. Mueller, B. Backes, H. W. Höppel, M. Göken. Nanoindentation strain-rate jump tests for determining the local strain-rate sensitivity in nanocrystalline Ni and ultrafine-grained Al, Journal of Materials Research, 26 (11) (2011) 1421–1430.

[33] D. Peykov, E. Martin, R. R. Chromik, R. Gauvin, M. Trudeau, Evaluation of strain rate sensitivity by constant load nanoindentation, Journal of Materials Science, 47 (20) (2012) 7189–7200.

[34] Y. Liu, J. Hay, H. Wang, X. Zhang, A new method for reliable determination of strain-rate sensitivity of low-dimensional metallic materials by using nanoindentation, Scripta Materialia, 77 (0) (2014) 5–8.

[35] R. Pippan, F. Wetscher, M. Hafok, A. Vorhauer, I. Sabirov, The limits of refinement by severe plastic deformation, Advanced Engineering Materials, 8 (11) (2006) 1046–1056.

[36] R. Pippan, S. Scheriau, A. Hohenwarter, M. Hafok, Advantages and limitations of HPT: A review, Materials Science Forum, 584-586 (2008) 16–21.

[37] M. Kreuzeder, M.-D. Abad, M.-M. Primorac, P. Hosemann, V. Maier, D. Kiener, Fabrication and thermo-mechanical behavior of ultra-fine porous copper, Journal of Materials Science, 50 (2) (2015) 634–643.

[38] A. Bachmaier, M. Kerber, D. Setman, R. Pippan, The formation of supersaturated solid solutions in Fe-Cu alloys deformed by high-pressure torsion, Acta Materialia, 60 (3) (2012) 860–871.

[39] M. M. Primorac, M. D. Abad, P. Hosemann, M. Kreuzeder, V. Maier, D. Kiener, Elevated temperature mechanical properties of novel ultra-fine grained Cu-Nb composites, Materials Science and Engineering: A, 625 (0) (2015) 296–302.

[40] J. M. Wheeler, J. Michler, Indenter materials for high temperature nanoindentation, Review of Scientific Instruments, 84 (10) (2013) 101301.

[41] K. Durst, V. Maier, Dynamic nanoindentation testing for studying thermally activated processes from single to nanocrystalline metals, Current Opinion in Solid State and Materials Science, 19 (6) (2015) 340-353.

[42] E. W. Hart, Theory of the tensile test, Acta Metallurgica, 15 (2) (1967) 351–355.

[43] L. J. Gibson, M. F. Ashby, Cellular solids: structure and properties, Vol 11. Cambridge University Press, 1997.

[44] D. Farkas, A. Caro, E. Bringa, D. Crowson, Mechanical response of nanoporous gold, Acta Materialia, 61 (9) (2013) 3249–3256.

[45] T. J. Balk, C. Eberl, Y. Sun, K. J. Hemker, D. S. Gianola, Tensile and compressive microspecimen testing of bulk nanoporous gold, JOM, 61 (12) (2009) 26–31.

[46] N. Mameka, K. Wang, J. Markmann, E. T. Lilleodden, J. Weissmüller, Nanoporous gold - testing macro-scale samples to probe small-scale mechanical behavior, Materials Research Letters, 4 (1) (2016) 27-36.

[47] L. Luehrs, C. Soyarslan, J. Markmann, S. Bargmann, J. Weissmüller, Elastic and plastic poisson’s ratios of nanoporous gold, Scripta Materialia, 110 (2016) 65–69.

[48] O. B. Olurin, N. A. Fleck, M. F. Ashby, Deformation and fracture of aluminium foams, Materials Science and Engineering: A, 291 (1-2) (2000) 136–146.

[49] K. Edalati, Z. Horita, High-pressure torsion of pure metals: Influence of atomic bond parameters and stacking fault energy on grain size and correlation with hardness, Acta Materialia, 59 (17) (2011) 6831–6836.

[50] B. D. Beake, J. F. Smith, High-temperature nanoindentation testing of fused silica and other materials, Philosophical Magazine A, 82 (10) (2002) 2179–2186.

[51] W. C. Oliver, R. Hutchings, J. B. Pethica, Measurement of hardness at indentation depths as low as 20 nanometers, Microindentation Techniques in Material Science and Engineering, 889 (1986) 90–108.

[52] W. D. Nix, H. Gao, Indentation size effects in crystalline materials: A law for strain gradient plasticity, Journal of the Mechanics and Physics of Solids, 46 (3) (1998) 411–425.

[53] G. B. Rathmayr, R. Pippan. Influence of impurities and deformation temperature on the saturation microstructure and ductility of HPT-deformed nickel, Acta Materialia, 59 (19) (2011) 7228–7240.

[54] G. Simmons, H. Wang, Single Crytsal Elastic Constants and Calculated Aggregate Properties - A Handbook. MIT Press, Cambridge, 1971.

[55] H. E. Boyer, T. L. Gall, Metals Handbook, American Society for Metals, Ohio, 1985.

[56] J. D. Kiely, J. E. Houston, Nanomechanical properties of Au (111), (001), and (110) surfaces, Phys. Rev. B, 57 (1998) 12588–12594.

[57] D. Caillard, J. L. Martin, Thermally activated mechanisms in crystal plasticity, Vol. 8, Pergamon, 2003.

[58] B. Farrokh, A. S. Khan, Grain size, strain rate, and temperature dependence of flow stress in ultra-fine grained and nanocrystalline Cu and Al: Synthesis, experiment, and constitutive modeling, International Journal of Plasticity, 25 (5) (2009) 715–732.

[59] V. Maier, A. Leitner, R. Pippan, and D. Kiener. Thermally activated deformation behavior of ufg-Au: Environmental issues during long-term and high-temperature nanoindentation testing, JOM, 67 (12) (2015) 2934–2944.

[60] A. Stalder, U. Dürig, Study of yielding mechanics in nanometer-sized Au contacts, Applied Physics Letters, 68 (5) (1996) 637–639.

[61] K. Wang, A. Kobler, C. Kübel, H. Jelitto, G. Schneider, J. Weissmüller. Nanoporous-gold-based composites: toward tensile ductility, NPG Asia Materials, 7 (2015).

[62] T. J. Rupert, J. R. Trelewicz, C. A. Schuh, Grain boundary relaxation strengthening of nanocrystalline Ni-alloys, Journal of Materials Research, 27 (2012) 1285–1294.

[63] R. Dou, B. Derby, Deformation mechanisms in gold nanowires and nanoporous gold, Philosophical Magazine, 91 (7-9) (2011) 1070–1083.

[64] W. Voigt, Über die Beziehung zwischen den beiden Elasticitätsconstanten isotroper Körper. Annalen der Physik, 274 (12) (1889) 573–587.

[65] J. M. Wheeler, D. E. J. Armstrong, W. Heinz, R. Schwaiger, High temperature nanoindentation: The state of the art and future challenges, Current Opinion in Solid State and Materials Science, 19 (6) (2015) 354-366.

[66] T. Kunimine, T. Aragaki, T. Fujii, S. Onaka, M. Kato, Inverse temperature dependence of activation volume in ultrafine-grained copper processed by accumulative roll-bonding, Journal of Materials Science, 46 (12) (2011) 4302–4307.

[67] J. M. Wheeler, V. Maier, K. Durst, M. Göken, J. Michler, Activation parameters for deformation of ultrafine-grained Aluminum as determined by indentation strain rate jumps at elevated temperature, Materials Science and Engineering: A, 585 (0) (2013) 108–113.

[68] T. Zhu, J. Li, A. Samanta, A. Leach, K. Gall, Temperature and strain-rate dependence of surface dislocation nucleation, Phys. Rev. Lett., 100 (2008) 025502.

[69] J. Bach, J. P. Liebig, H. W. Höppel, W. Blum, Influence of grain boundaries on the deformation resistance: insights from an investigation of deformation kinetics and microstructure of copper after predeformation by ECAP, Philosophical Magazine, 93 (35) (2013) 4331–4354.

[70] C. J. Ruestes, D. Farkas, A. Caro, E. M. Bringa, Hardening under compression in Au foams, Acta Materialia, 108 (2016) 1–7.

Publication B

Extraction of flow behavior and Hall–Petch parameters using a nanoindentation multiple sharp tip approach

A. Leitner[1], V. Maier-Kiener[2], D. Kiener[1]

Advanced Engineering Materials 19:4 (2017) 1-9

[1] Department Materials Physics, Montanuniversität Leoben, Austria
[2] Department Physical Metallurgy and Materials Testing, Montanuniversität Leoben, Austria

B - Abstract

An appealing idea to material scientists is to extensively characterize the mechanical behavior of materials with minimal experimental effort while guaranteeing highly reliable results. In the course of time, depth-sensing hardness testing has become incessantly apparent to be a candidate technique to reach this objective. While nanoindentation is already a standard method to extract hardness and Young's modulus of a material the potential of this technique is not yet fully exploited. Outlined in this study, attention must be paid to precise tip calibration and the restricted comparability of nanoindentation hardness and Vickers microhardness. We demonstrate on the example of nickel and tungsten, with microstructures ranging from single crystalline to nanocrystalline dimensions, how Hall-Petch parameters and flow curves can be extracted from nanoindentation by using four pyramidal tips with varying apex angle. It is shown that by using appropriate definitions of indentation stress and strain and considering the indentation size effect the obtained values exceedingly coincidence with literature values determined by uniaxial tests.

B - Introduction

The mechanical characterization of materials by simple hardness measurements attracts attention in engineering disciplines since decades [1, 2]. Nowadays, nanoindentation provides the opportunity to extract a variety of mechanical properties on the nano- or micro-scale and thus is of great interest especially for limited volumes of interest. Nanostructured materials, often only produced in bench-scale, are in the focus of researchers due to their outstanding strength and functionality [3]. Their mechanical characterization is of prime interest, which may be amongst the governing reasons why the number of publications per year on nanoindentation steadily increases since more than twenty years. The determination of hardness *H* and Young's modulus *E* following the analysis introduced by Oliver and Pharr [30] is common practice by now, but also more sophisticated techniques seize the material research community. By way of example, obtaining stress-strain curves from nanoindentation which are comparable to uniaxial flow curves is of great interest and has been extensively investigated in recent years [5-12]. One major asset is that the stress state with a high hydrostatic part allows testing materials with poor ductility, where mechanical and rate-dependent behavior would not be accessible in conventional uniaxial tests. Furthermore, it enables studying the hardening behavior of single crystals [13]. Still the technique has not yet asserted as a standard testing method. By reviewing the existing literature, one realizes that there are still several uncertainties. In a strict sense, discrepancy starts at the definition of hardness per se, which is imprecisely defined as the resistance of a material to the penetration of a harder material. The analysis of conventional hardness tests compared to instrumented indentation may yield to significantly differing values and shall be part of the focus of the present study [14]. Furthermore, the introduced stress-state is multiaxial and therefore it is not self-evident to define a representative strain ε_r and representative stress σ_r corresponding to uniaxial tests. Basic findings are that the stress strongly correlates with hardness and that strain is dependent at least on the geometry of the indenter tip [15-17]. For instance, in early works of Tabor cone-shaped tips with varying opening angles were used to perform macroscopic hardness tests [16]. A linear relation between H to σ_r was assumed, and linked by a constant called by constraint factor C^*. By comparing hardness to uniaxial stress-strain curves, C^* was determined to be close to 2.8. Additionally, this resulted in an empirical definition of a representative strain ε_r which was found to be dependent on the half apex angle of the used cones [16, 17]. Surveyed, Tabor was likely not considering the additional influence of the materials parameter E/σ since the tested materials mild steel and copper show rather high values of around 800-1600 at which the C^* is rather insensitive [18, 19]. Particularly various FEM studies showed that C^* may strongly depend on this parameter [9, 10, 18, 20-22]. Sophisticated dimensionless analysis gives an accurate approximation of C*, but always requires knowledge of constitutive parameters such as yield strength, modulus or hardening parameters a priori [10-12, 22]. Once definitions for stress and strain are clarified, determination of stress-strain curves is a straight-forward procedure.

In the present work, we will conduct a detailed comparison of nanoindentation and Vickers microhardness tests, and follow Tabors work investigating the approach of determining stress-strain curves by nanoindentation using four sharp indenter tips with varying opening angle. To the best knowledge of the authors, this has never been conducted on metals so far. Four samples each of nickel and tungsten will be investigated where the specimen have microstructures reaching from single crystalline (SX) to nanocrystalline (NC) dimensions, ending up in a large interval of E/σ ratios and strongly different work-hardening behavior. In addition to their flow behavior, also Hall-Petch (HP) parameters will be extracted for both materials to examine whether hardness tests are actually suitable and comparable to parameters obtained from uniaxial tests. Finally, it will be demonstrated that the used analysis method leads to excellent flow curve data when applied to the tested materials compared to bulk literature data.

B - Experimental details

Investigated materials

Nickel and tungsten samples have been investigated in the present study. The high melting points ($T_{M,Ni}$ = 1455 °C, $T_{M,W}$ = 3422 °C [55]) will ensure that no microstructural changes occur at RT, particularly important for the NC and ultra-fine grained (UFG) specimen. Due to the face centered cubic (FCC) structure of Ni and body centered cubic (BCC) structure of W, possible influences of the crystal structure will be observable. Fine grained (FG) Ni, UFG Ni and UFG W were fabricated by High Pressure Torsion (HPT), whereat former was annealed to coarsen the microstructure. Further details of fabrication and microstructure of UFG Ni and electrodeposited NC Ni can be obtained from the study by Leitner et al. [24]. For details regarding CG W and FG W see the study of Maier et al. [25]. Both, electrodeposited and HPT metals feature a high fraction of high angle grain boundaries (> 65%) [26-28], thus no significant influence of the grain boundary character is expected. The orientations of SX samples were confirmed by electron backscatter diffraction (EBSD) where the Ni SX is oriented in (1 0 0) and W SX in (1 1 0). The mean grain size of the refined microstructures was either determined using EBSD (UFG and FG samples), X-Ray Diffraction (XRD) (Ni NC) or optical microscope (W CG, linear intercept method). The grain size determined by XRD has to be considered as a lower limit, since also sub-grain structures will be covered by this technique. Micrographs of all samples except the SX state are shown in Figure 1, where the images were obtained by a scanning electron microscope (SEM; LEO type 1525, Carl Zeiss GmbH, Germany) except of CG W, which was recorded using an optical microscope. All samples were mechanically and electrolytically polished in order to avoid any influences of surface preparation.

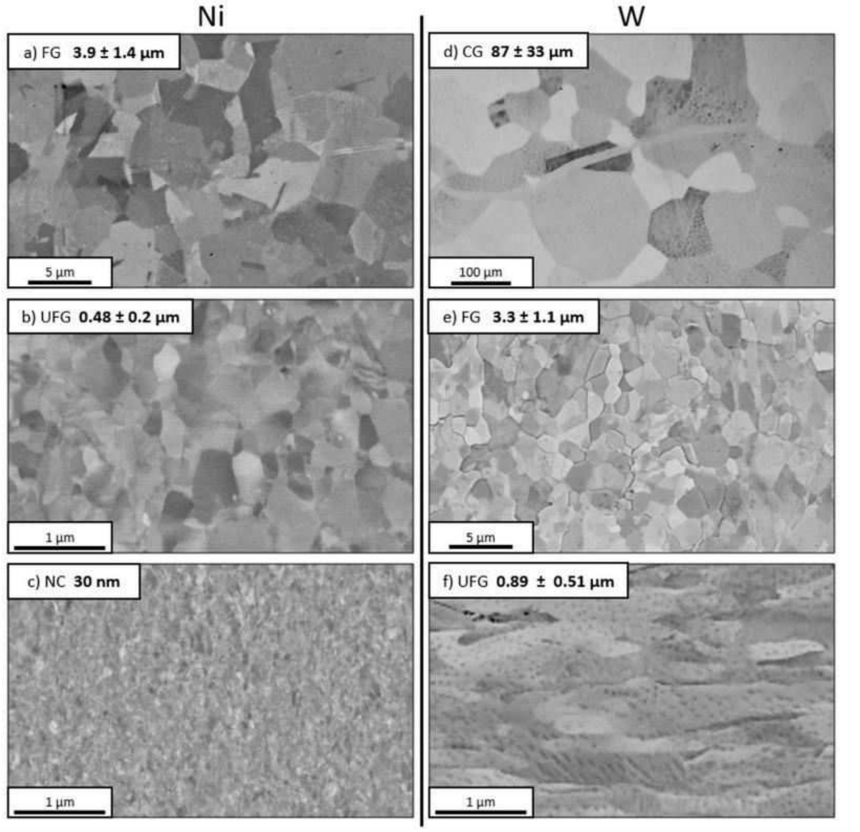

Figure 1. SEM microstructure observations of the Ni (a)-c)) and W (e)-f)) sample. FG and UFG Ni (a) & b)) show HPT Ni samples in axial direction. d) The microstructure of CG W was investigated with an optical microscope. f) shows UFG W in radial direction. Mean grain sizes are imprinted in the according images. Ni SX (1 0 0) and W SX (1 1 0) are not displayed.

Nanoindentation experiments

Indentation tests were conducted on a Nanoindenter G200 (Keysight Technologies, USA) with a continuous stiffness measurement (CSM) option. The frequency of the superimposed force was set to 45 Hz with a displacement amplitude of 2 nm. Hardness and Young's modulus were obtained by the standard analysis proposed by Oliver and Pharr [30]. CSM measurements allow to determine the mechanical properties continuously in dependence of indentation displacement. Thus, for isotropic materials a horizontal profile of the Young's modulus over displacement is a feasible indicator for reliable measurements (see for example supplementary Figure A1). At least five indents were made with an indentation strain-rate of 0.05 s^{-1} for each tip and material, and measurements were the thermal drift exceeded 0.1 nm/s were discarded. Four 3-sided pyramidal diamond tips with varying face angle (FA) were tested on each material, details are given in Table 1. The Berkovich tip was manufactured by MicroStar, USA while the FA 80, FA 50 and Cube Corner tip were obtained from Synton MDP LTD, Nidau, Switzerland. The maximum displacement was set to be 2500 nm, but for the FA 80 tip the device specific force limit of 500 mN was reached already at lower depths for materials with higher strengths. For perfect pyramidal tips the projected area depending on the contact depth is described by [30]:

$$A_c(h_c) = C_1 \cdot h_c^2 \,, \qquad \text{equation (1)}$$

where C_1 composes from the pyramidal geometry as

$$C_1 = 3 \cdot \sqrt{3} \cdot \tan^2(\alpha), \qquad \text{equation (2)}$$

with α as the face angle of the pyramid. Hence, by calibration of the area function on an isotropic material such as fused quartz, one can assess C_1 experimentally and determine the actual face angle. In order to calculate ε_r of the respective tip, the corresponding cone angle β will be needed which can be determined by

$$\tan(\beta) = \sqrt{\frac{C_1}{\pi}} \qquad \text{equation (3)}$$

Table 1 shows the obtained data and compares the nominal strain predicted from the strain definition of Tabor [16] with the actual strain from calibrations, proofing that the tip shapes are very close to the ideal specifications. Furthermore, it is important to note that for materials exhibiting an indentations size effect (ISE) hardness should rather be determined at the same contact area than the same contact depth [29, 30]. Table 1 shows the contact depths for each tip resulting in identical contact areas. Another approach is to determine the bulk hardness of the material following the analysis of Nix and Gao [29]. In their work, an extrapolation to the bulk hardness H_0 is possible if several data pairs of H and displacement h are experimentally measured:

$$\left(\frac{H}{H_0}\right)^2 = 1 + \frac{h^*}{h} \,, \qquad \text{equation (4)}$$

where h^* is an internal length scale parameter which provides information on how pronounced the indentation size effect is. In the present study, the consequences of using either H at the same contact area or H_0 will be discussed.

Table 1. Overview of used tips and their geometrical properties. Actual strain values compared to the nominal values imply that all tips are close to their specifications.

Tip	**Face angle α**	**Repr. cone angle β**	**Nominal strain ε_n**	**Actual strain ε_a**	**Mech. properties determined at**
FA 80	80 °	82.2 °	2.74 %	2.64 %	250 – 350 nm
Berkovich	65.3 °	70.3 °	7.16 %	7.16 %	650 – 780 nm
FA 50	50 °	56.9 °	13.04 %	12.62 %	1190 – 1430 nm
Cube Corner	35.3 °	42.3 °	21.98 %	21.65 %	2000 – 2400 nm
Vickers	68 ° (4-sided)	70.3 °	7.16 %	-	after unloading

Microhardness testing

All microhardness measurements were performed on a BUEHLER Micromet 5100 using a diamond Vickers indenter. Depending on the material, loads F of either 200 or 500 gf were used to determine the Vickers hardness. Again at least five impressions were performed for each material. Diagonals (*D1, D2*) of residual impressions were measured with an optical microscope in order to calculate H_V according to [1]:

$$HV = \frac{F \cdot 2 \cdot \sin\left(\frac{136\,°}{2}\right)}{D^2} \qquad \text{equation (5)}$$

Vickers hardness vs. nanoindentation hardness

Since hardness is dependent on the geometry of the used tip it is important to note that different hardness testing techniques are only restrictively comparable. Primary, tips have to be divided into two groups, self-similar (pyramidal tips, cones) and non-self-similar tips (e.g. spheres). In the present work we will only focus on the self-similar type so that ε_r should not be influenced by the indentation depth. Secondly, for sharp tips the hardness value will be dependent on the tip opening angle. Therefore, if we want to compare conventional Vickers hardness testing with nanoindentation, we have to ensure that the representative cone has the same apex angle. For large indentation depths commonly reached in Vickers hardness testing imperfect tip shapes at low penetration depths can be neglected. This is not the case for nanoindentation and thereby the reason why three-sided pyramids are used. Three faces converging at one point this will, for geometric reasons, necessarily give a sharp tip, while four faces will likely result in an edge instead.

However, the proportions of a Berkovich tip were chosen in a way that it has the equal representative cone compared to a Vickers tip.

We would like to point out, that obtained hardness values can still not be directly compared, even though these values are sometimes mixed up in literature. The discrepancy results from two main aspects:

1) Used contact area

Vickers hardness refers to the load normalized by the real area in contact while in nanoindentation hardness load is divided by the projected area. However, this issue can simply be compensated by using D^2 instead of $D^2/\sin(\alpha)$ for the hardness calculation, resulting in a constant coefficient of 1.08 to convert the real contact area to the projected contact are in the case of Vickers and Berkovich tips.

2) Consideration of real contact depth

Vickers hardness is calculated from the size of the residual impression, while nanoindentation obtains the projected area in contact at maximum load. Particularly for materials with low Young's modulus and high hardness, such as fused quartz, this aspect may lead to a vast underestimation of microhardness. Unlike point 1), it is not possible to correct the hardness directly for Vickers measurements since the stiffness of the material has to be known. In this work, we will always refer to the hardness definition of nanoindentation. Vickers values will be corrected by the stiffness obtained from nanoindentation measurements.

Another aspect to consider is the well-known indentation size effect for materials with a coarse microstructure, resulting from geometrically necessary dislocations and thereby introduced large strain gradients, especially at low indentation depths [29]. This can be accounted for by obtaining H_0 from equation (4).

Stress and strain definitions for hardness testing

Beside different definitions of hardness per se, the conversion to a stress value is controversially discussed, too. In general, a linear relationship between representative stress and hardness is assumed [16],

$$H(\varepsilon_r) = C^* \cdot \sigma_r(\varepsilon_r), \qquad \text{equation (6)}$$

with σ_r as the representative stress for a representative strain ε_r and C^* as the constraint factor. For analytical approaches, as performed in an early work of Prandtl [15], an equivalent stress has to be defined. Prandtl uses the prominent definition of Tresca and defines the material as rigid-perfectly plastic which finally leads to a constraint factor of 2.57. A later work of Tabor also proposes to use a constant constraint factor C^*, independent of tip angle and material [16].

Indeed, several studies have demonstrated that C^* actually depends on material parameters and tip angle. Literature values for C^* vary between 1 and 3.3 depending on the material. Various approaches showed that with consideration of E/σ_y reasonable C^* values can be determined. Since this ratio is in the same order of magnitude (10^2-10^3) for most conventional metals, a factor of 2.8 as proposed by Tabor is reasonable and will be used throughout this paper.

Similar disagreements still exist in terms of strain definitions. Tabor noted a cotangents dependency of the strain [16, 17]:

$$\varepsilon_r = 0.2\cot(\beta) \qquad \text{equation (7)}$$

Definition of strain by equation (7) will be used in this study. Several other definitions of ε_r emerge in literature but are seldom used. Recently, Pathak and Kalidindi tried to describe strain in a more physical way, meaning to relate a length of the unstrained material to the length of the strained material [6]. Even though this was based on the idea of describing the strain introduced by a sphere, one can easily apply equation (7) to cones. Since those are self-similar, this results in a constant strain, only depending on the cone angle. However, this results in a pre-factor of 0.42 and thereby in far higher strains, but still in a cotangents dependency:

$$\varepsilon_r = \frac{4}{3\pi}\cdot\frac{h_t}{a_c} = \frac{4}{3\pi}\cdot\cot(\beta) \qquad \text{equation (8)}$$

Once representative strain and stress are defined, the determination of flow curves is straight forward. Using the four tips with varying apex angle each will provide a data pair of $(\varepsilon_r|\sigma_r)$ for the flow diagram. The additional knowledge of the Young's modulus enables to imprint Hooke's line and will supplement the stress-strain diagram. In the present work, rather than relying on certain assumptions, comparison to known bulk data will justify the correct conversion of stress and strain.

Hall-Petch behavior

Since Hall and Petch [1, 2] noted the increase of strength with decreasing grain size in mild steel, the Hall-Petch relation has often been confirmed to describe a broad range of materials and structure sizes. It has also been noted that the HP parameters are dependent on the strain at which the stress values are obtained [33]:

$$H(\varepsilon) = H_0(\varepsilon) + k_{H,HP}(\varepsilon)\cdot\frac{1}{\sqrt{d}} \qquad \text{equation (9)}$$

Taking into account the relation between hardness and strength (equation (6)) for metals, one can simply obtain the stress-related parameter according to

$$\sigma(\varepsilon) = \sigma_0(\varepsilon) + k_{\sigma,HP}(\varepsilon)\cdot\frac{1}{\sqrt{d}} \qquad \text{equation (10)}$$

The material parameter k_{HP} indicates the extent to which grain boundaries contribute to the strengthening. The higher k_{HP}, the more gain in strength can be reached by the refinement of the microstructure. On the other hand, σ_0 represents the strength of the material in the absence of grain boundaries, which in the end should coincidence with the strength of a single crystal with similar dislocation density ρ. The strength contribution of dislocation hardening may slightly shift the HP-parameters, even though microstructural dimensions of the UFG and NC samples may lead to differing deformation mechanisms, where the ~√ρ dependency of the flow stress does not necessarily hold true anymore. Moreover, all tips introduce rather large strains and therewith increase the dislocation density around the indent. Naturally, the increase will be higher in single crystals than in the samples with refined microstructure (higher dislocation densities) and reduce the effect on the k_{HP} parameter. Furthermore, it has to be noted that strictly spoken the HP parameters are also influenced by the strain rate of the tests. For fine grained FCC metals, higher strain-rates will lead to increasing k_{HP} and decreasing σ_0 values, while BCC metals, tested underneath their critical temperature, will show the opposite behavior.

In order to consider hardness measurements of single crystals in the HP analysis, a reasonable grain size has to be chosen. Once the plastic zone size *c* is significantly smaller than the grain volume, *H* cannot further be dependent on the grain size. FEM studies of Durst et al. revealed that *c* is about three times the contact radius a_c when a plastic strain of 0.2 % is set as border between plastic zone and unaffected material [34]. This results in a radius of 7-55 µm depending on the used tip. Using Johnsons model, which also includes the mechanical properties if the tested material, *c* can be predicted by [13],

$$\left(\frac{c}{a_c}\right)^3 = \frac{1}{3\cdot\tan\beta}\cdot\frac{E}{\sigma_y}, \qquad \text{equation (11)}$$

resulting in values of 13-52 µm for Ni and 12-48 µm for W, respectively. These values should be seen as a lower bound but due to the $\propto d^{-\frac{1}{2}}$ relation, and obtained HP parameters are insensitive to the used grain size in this order of magnitude anyway, as the forest dislocation spacing will set the smaller internal length scale. Taking into account the mentioned aspects, mechanical data obtained in this study can be used to extract HP parameters and examine their dependency on strain.

B - Results and analysis

Comparison between Vickers and nanoindentation hardness

Evaluation of the hardness values for all tested materials shows good agreement between Berkovich nanoindentation and Vickers microhardness tests as demonstrated in Figure 2. However, even after the indicated corrections regarding contact area, there is a slight underestimation of the hardness when microhardness measurements are considered. The misfit, displayed with open triangles in Figure 2, does not exceed 13% and apparently scales with the microstructure size. A difficulty in microhardness measurements is that Vickers tips can commonly not be calibrated and therefore a deviation of the tip angle and consequently the representative strain are not known. Overall, the materials show the expected trend, as hardness clearly increases with decreasing grain size.

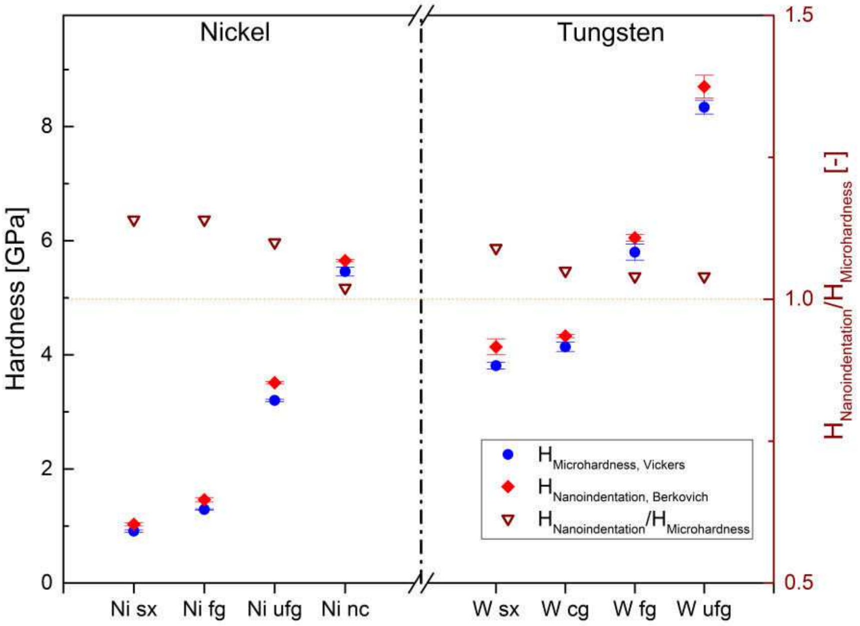

Figure 2. Comparison between nanoindentation hardness data measured with a Berkovich tip and Vickers microhardness measurements which were corrected according to issues mentioned in chapter 2.3. The relative mismatch between the hardness values is illustrated with open triangles.

Hall-Petch behavior

Beside the mechanical behavior of the individual samples, the obtained nanoindentation data also allows to determine HP parameters for each tip type, and thereby for varying values of representative strain. Cross-sections of the corresponding cones are shown to scale above the diagram in Figure 3. The correlation coefficient for Ni is 0.961 on average and 0.996 for W, suggesting that the HP behavior is valid down to the smallest grain size tested and that the contribution of dislocation hardening is negligible. Figure 3 shows k_{HP} and σ_0 in dependence of the tip type, where error bars were obtained by error analysis using the total differential method. HP parameters naturally vary with strain and are eventually dependent on the hardening behavior of the individual samples. Therefore, coarse grained metals which are expected to show distinct hardening compared to their fine structured counterparts will exhibit reduced k_{HP} and additionally increased σ_0 at high strains, a trend clearly observed in the present study. The k_{HP} values obtained by ISE corrected data for Ni is in the range between 0.2 and 0.28 MPa·m$^{-1/2}$, for W k_{HP} is significantly higher ranging from 1.23 to 1.86 MPa·m$^{-1/2}$. The strength of the grain interior given by σ_0 continuously increases with higher strains. If hardness is still affected by the ISE (illustrated as open symbols in Figure 3), this of course rises the level of σ_0. For Ni the different analysis ends up in the same k_{HP} values, while for W a slight decrease is observed.

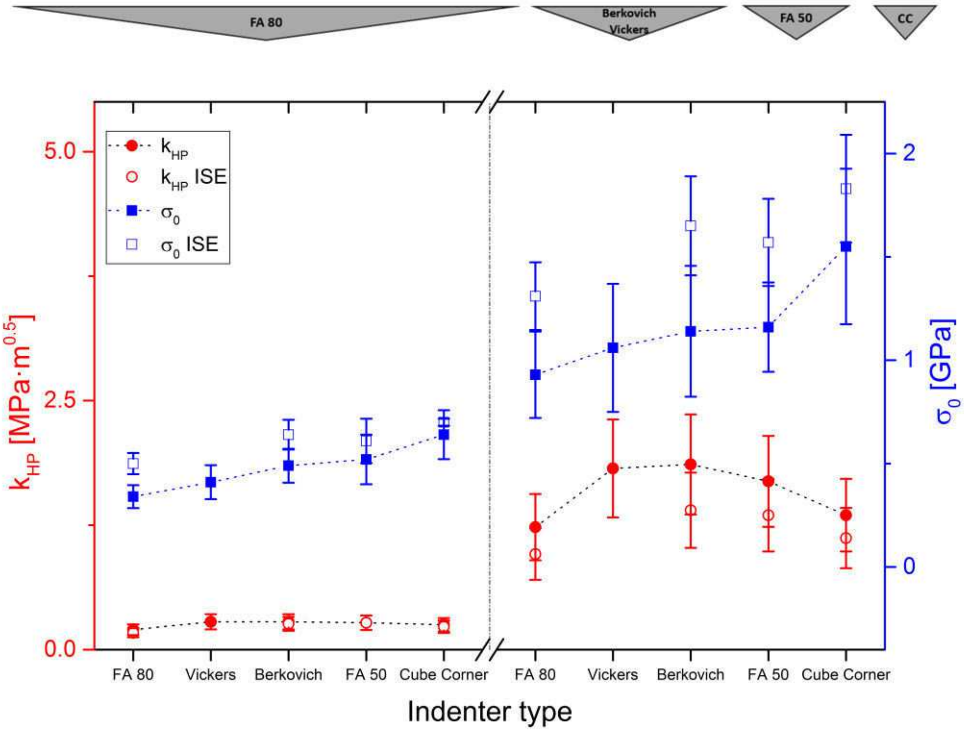

Figure 3. Hall-Petch parameter in dependence of the used indenter type. Representative cones of all used tips, imprinted above the diagram to scale. As expected, σ_0 increases with decreasing tip angle. The HP parameter k_{HP} shows a slight increase from FA80 to Berkovich and decreases again for tips with smaller apex angle. Open symbols are referred to data still including the ISE.

Nanoindentation flow curves

The indentation flow curves of the tested samples are displayed in Figure 4. The refinement of the Ni and W microstructure considerably increases the stress levels and leads to a reduced hardening behavior. The hardness values of CG W only slightly deviate from SX W. However, since the volume of the plastic zone introduced by nanoindentation is distinctly smaller than the average grain volume, grain boundaries will only play a minor role and hardly contribute to higher hardness values. For UFG Ni, NC Ni and UFG W even a slight softening behavior is observable at high strains. The open symbols represent data still including the ISE contribution. Consequently, the stress values especially of coarse microstructures are shifted to significant higher levels, nonetheless the trends in flow behavior remain the same.

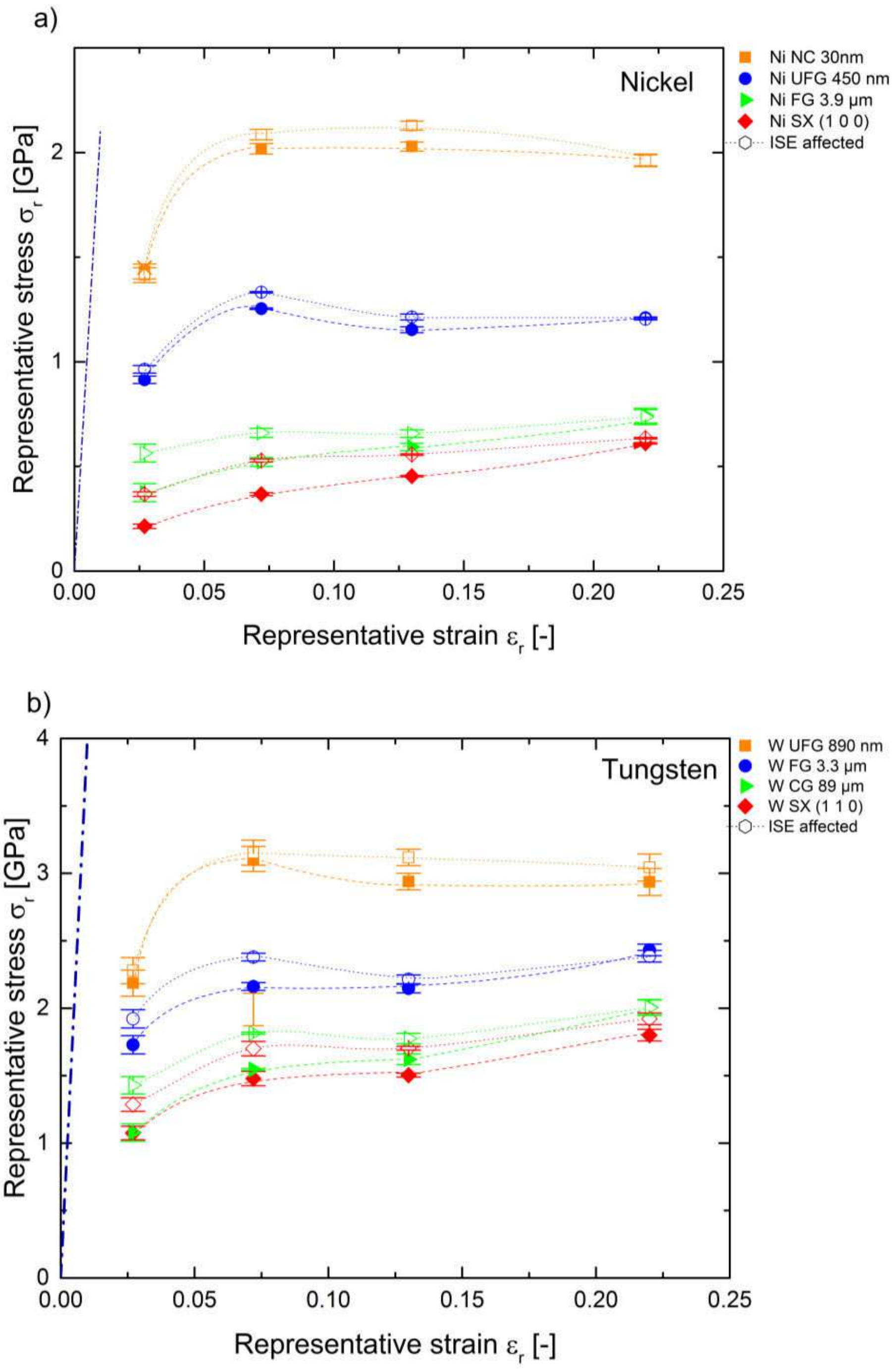

Figure 4. Indentation flow curves for a) Ni and b) W with different microstructures. As expected, coarse grained materials and single crystals show a low yield stress and significant hardening behavior with increasing strain. NC and UFG samples show a slight decrease of stress at higher strains.

B - Discussion

Microhardness vs. Nanoindentation

Only little attention in literature is paid to proper comparison of hardness data. As demonstrated, one has to be cautious when hardness values from different measurement techniques are compared. At first, it has to be ensured that the used tips have a comparable representative strain, such as Berkovich and Vickers tips. If so, also the analysis procedure has to be carefully reviewed in order to avoid mismatches. In the investigated case of Berkovich nanoindentation and Vickers microhardness testing, neglecting the differences in analysis procedure as described in 2.3 would end up in errors up to 30 %, while after correcting the error drops to levels below 10 % in average. A slight underestimation of microhardness has also been noted in FEM studies on thin films [35]. Riester et al. showed in a study that the nanoindentation hardness values can also be lower if the tip shape differs from specification. Recalculating their tip shapes from calibration data shows a strain deviation of 0.6% between Berkovich and Vickers tip, which consequently leads to higher hardness values for the Vickers measurements [14]. Since the correct shape of the Vickers tip is not known, this remains a potential error source in the current work. A slightly higher apex angle of the Vickers tip would agree well with the findings in this study. Coarse grained materials, which naturally feature a more distinct work hardening, would then show a larger relative misfit, as observed in this study.

Hall-Petch behavior

As demonstrated, HP-constants should carefully be used since there are various influences on their absolute values. Due to the strain dependency, literature values have to be carefully reviewed. Figure 3 demonstrates that a significant difference of HP values, obtained at different strain levels, may occur. This mismatch may even grow if the parameters are obtained by uniaxial tests, where the flow stress at a plastic strain of only 0.2% is used, thus excluding most strain hardening contributions. Despite strain and strain-rate dependency, also the dislocation hardening behavior of the tested samples has to be considered. Since σ_0 can be understood as the strength of the grain interior, this value will be influenced by the dislocation densities of the used samples. As seen for Ni in this study, this can still end up in lower stress values for the tested single crystal compared to the σ_0 values. This most likely results from a lower dislocation density of the tested SX compared to the samples with refined microstructures.

Overall, the obtained HP-parameters agree well with literature values ranging from 0.16 to 0.24 MPa·m$^{0.5}$ [36-39]. Carlton and Ferreira collected literature data and provided a fit of all data, which ends up in an average value of 0.21 MPa·m$^{0.5}$ [40]. Tungsten is close to literature values as well, even though no comprehensive data could be found in literature. Tests on cold rolled W show values of 0.9 MPa·m$^{0.5}$, while samples obtained by powder consolidation exhibited values of around 1.4 MPa·m$^{0.5}$ [41] (converted to nanoindentation stress following section 2.3) and are thereby close to values measured in this study. Different to Ni, there is a slight influence on k_{HP} in W when data is not corrected for the ISE.

Nanoindentation flow curves

The slight softening behavior at high strains of the UFG and NC materials has been critically examined. Even though potential analysis errors may result from the constraint factor or occurring pile-ups, as illustrated in Figure 5, these would even lead to even lower hardness values. Moreover, as the stiffness is recorded continuously during indentation and the Young's modulus profiles show the expected values independent of depth (e.g. Figure A1), a strong influence of pile-ups can be excluded, although they are clearly visible for FA 50 and Cube Corner indents. Moreover, stress induced softening is known to occur for NC materials [42] and has also been observed in uniaxial compression tests of NC Ni [43]. For Ni, considering slightly differing grain sizes in the compared studies, values obtained by nanoindentation are in excellent agreement with literature values from uniaxial tests.

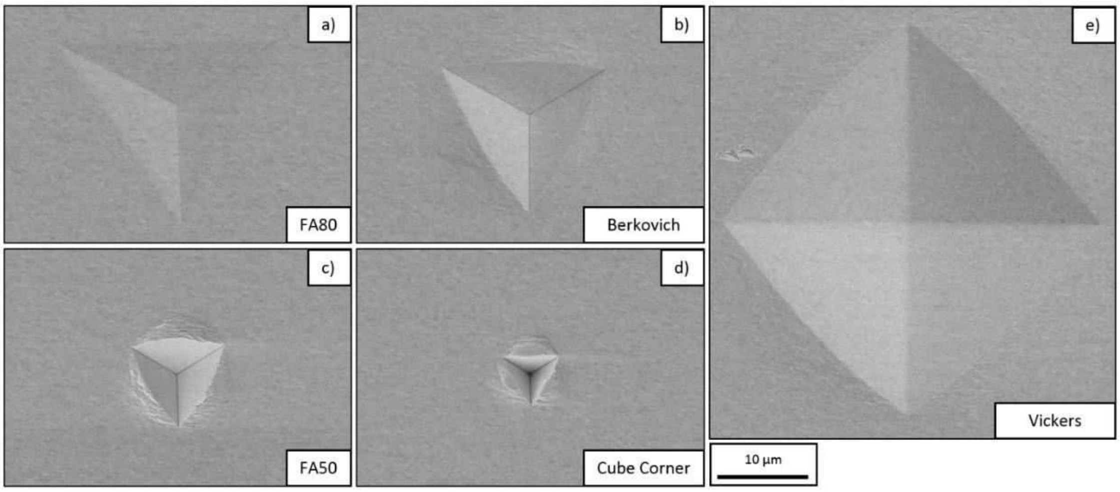

Figure 5. a)-e) SEM micrographs of residual impressions on UFG Ni for all used tips at the same magnification. With decreasing tip angle, material pile-ups become more distinct.

Figure 6 demonstrates the importance of correcting stress values for the ISE, particularly CG and SX samples. Without that correction stress levels are significantly above values found in literature. Data for high strains as introduced by Cube Corner or FA 50 is lacking in literature, as in uniaxial tests samples often fail due to poor ductility before reaching such strains. The multiaxial stress state during nanoindentation with a high hydrostatic contribution allows to test at higher strains.

The machining of uniaxial testing samples of W is challenging. This might be the reason for the lack of data literature, which makes it difficult to compare our results. Therefore, mainly Vickers hardness data is presented in Figure 6 b), which was corrected the same way as the Vickers values in this study. Taking into account the varying grain sizes, one can see that data of the present study is in good agreement with literature data.

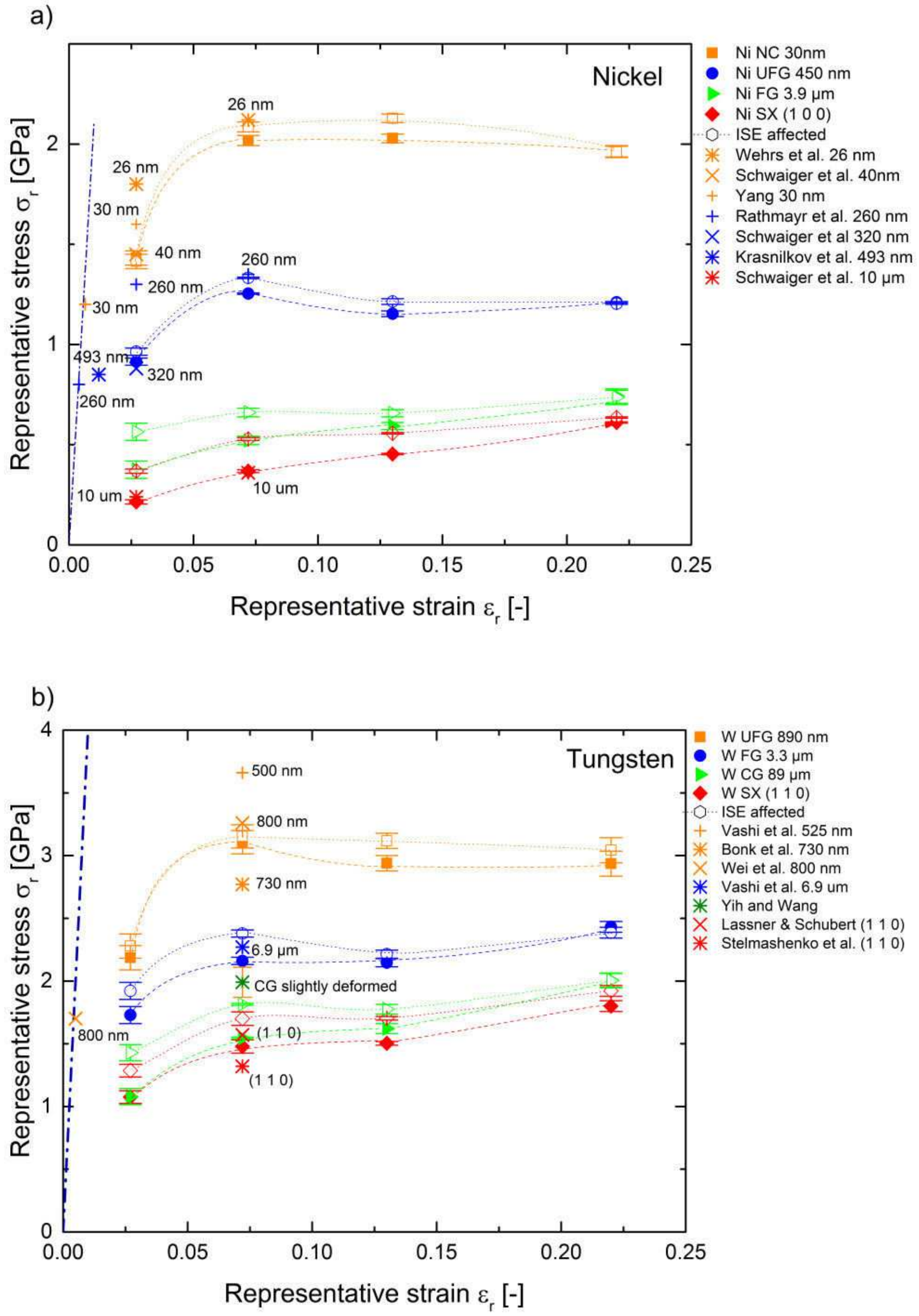

Figure 6. Comparison of flow stress values obtained in the present study by nanoindentation with literature values from uniaxial tests for a) Ni [44-48] and b) W [41, 49-53]. The average grain sizes are imprinted at the corresponding symbol.

B - Summary and conclusions

The present study demonstrates that a variety of mechanical properties can be obtained by nanoindentation measurements. Certainly, analysis has to be performed carefully and used parameters have to be reported to feasibly compare data to existing literature. For the comparison of hardness data not only the analysis procedure has to be known, but also tips have to be well calibrated. The actual representative cone angle has by far more validity than the specified angle, when the definitions of ε_r and σ_r proposed by Tabor are used [16]. Further, following conclusions can be drawn:

- When the standard Berkovich tip is used for nanoindentation, hardness values are in good agreement with conventional Vickers hardness tests (Figure 2). However, a series of corrections has to be applied in the analysis, since H is defined differently in these testing techniques. The knowledge of the actual tip shape is crucial since this will affect ε_r and consequently the measured hardness. Deep indentation depths should be favored to avoid influences of tip imperfections.
- Testing of Ni and W with various grain sizes allows to obtain HP parameter at four different strains. All determined values coincidence well with literature values although those are commonly obtained by uniaxial testing techniques. The profiles of σ_0 and k_{HP} show the expected trends for both materials in dependence of the strain and are slightly sensitive to an occurring indentation size effect.
- Using an approach with various sharp tips certainly allows to describe the flow behavior of metals, and due to the high hydrostatic component of the stress field even brittle materials can be tested at high strains. By accurate calibration of the tips, local indentation flow curves can be extracted and are in good accordance to literature values of uniaxial tests.

Summarized, nanoindentation is an outstanding technique to extract mechanical properties of metals, especially when material is limited, demanding to machine, or high lateral resolution is required. We clearly demonstrated that HP parameters as well as the flow behavior can be obtained utilizing the multiple sharp tip approach, and results can be evidently compared to data determined by uniaxial experiments. However, the physical background of the strain relation is not yet clarified but future work will be addressed to this topic. Certainly, finite element simulations concerning the influence of tip imperfections would optimally complement the present study will therefore be subject of prospective studies.

B - Acknowledgements

Funding of the Styrian and the Tyrolean Provincial Government, represented by Steirische Wirtschaftsförderungsgesellschaft mbH and Standortagentur Tirol, within the framework of the COMET Funding Programme (837900, MPPE A7.19) is appreciated. Further parts of this work were also funded by the Austrian Science Fund (FWF) via the project P25325-N20. All Ni samples were generously provided by DI Thomas Leitner and Prof. Reinhard Pippan (ESI Leoben).

B – Supplementary data

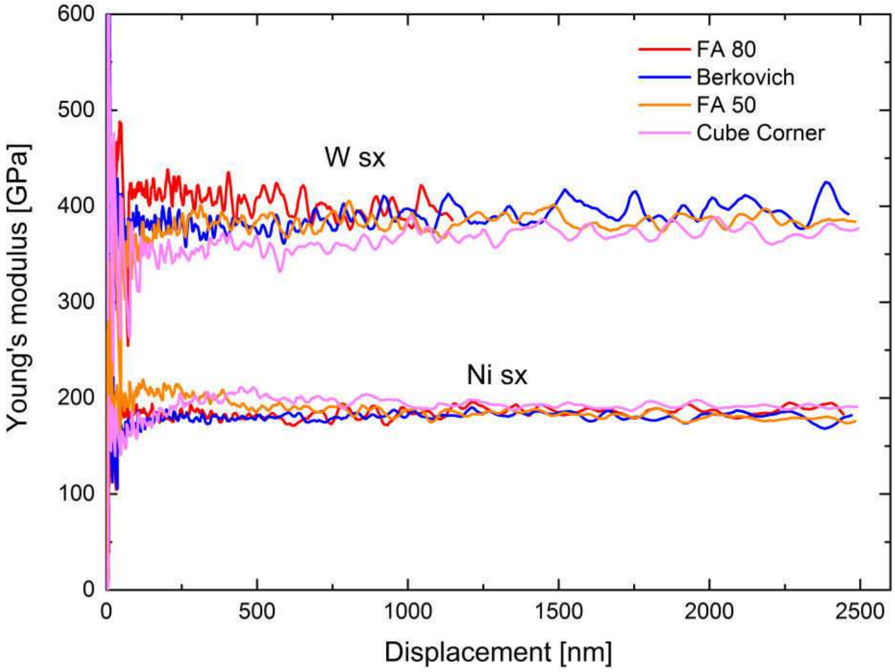

Figure A1. Young's modulus profiles of W SX and Ni SX for all used tip types. The horizontal trend indicates that the contact area is correctly determined and that there are no significant influences of pile-ups or sink-ins.

B - References

[1] R. L. Smith, G. E. Sandly, *Proc. Inst. Mech. Eng.* **1922**, *102(1)*, 623.

[2] F. Schulz, H. Hanemann, *Z. Metallkd.*, **1941**, 33, 124.

[3] R. Z. Valiev, Y. Estrin, Z. Horita, T. G. Langdon, M. J. Zehetbauer, Y. T. Zhu., *Mater. Res. Lett.* **2016,** *4(1)*, 1.

[4] W. C. Oliver, G. M. Pharr, *J. Mater. Res*. 1992, *7*, 1564.

[5] S. Basu, A. Moseson, M. W. Barsoum, *J. Mater. R*es. **2006**, *1(10)*, 2628.

[6] S. Pathak, S. R. Kalidindi, *Mater. Sci. Eng., R*. **2015**, *91*, 1.

[7] S. Shim, J. Jang, G.M. Pharr, *Acta Mater.* **2008**, *56(15)*, 3824.

[8] D. K. Patel, S. R. Kalidindi, *Acta Mater.* 2016, *112*, 295.

[9] K. Fu, L. Chang, B. Zheng, Y. Tang, H. Wang, *Mater. Des.* **2015**, *65*, 989.

[10] H. Chen, L.-X. Cai, *Acta Mater.* **2016**, *121*, 181.

[11] Y.-T. Cheng, C.-M. Cheng, *Mater. Sci. Eng., R.* **2004**, *44(4 - 5),* 91

[12] N. Chollacoop, M. Dao, S. Suresh, *Acta Mater.* **2003**, *51(13)*, 3713.

[13] K. L. Johnson, *J. Mech. Phys. Solids* **1970**, *18(2)*, 115.

[14] L. Riester, R. J. Bridge, K. Breder. *MRS Proc. – Symp. T.* **1998**, *522*, 45.

[15] L Prandtl, *Nachr. Gesell. Wissensch. Gött.* **1920,** 74.

[16] D. Tabor, *The Hardness of Metals*, OUP Oxford, **1951**.

[17] A. G. Atkins, D. Tabor, *J. Mech. Phys. Solids* **1965,** *13(3)*, 149.

[18] S.-D. Mesarovic, N. A. Fleck, *Proc. R. Soc. London, Ser. A* ***1999**, 455(1987),* 2707.

[19] Y.-T. Cheng, C.-M. Cheng, *Surf. Coat. Technol.* **2000**, *133*, 417.

[20] A. Clausner, F. Richter, *Eur. J. Mech. A Solids.* **2015**, *51*, 11.

[21] J. L. Hay, W. C. Oliver, A. Bolshakov, G. M. Pharr, *MRS Proc.* **1998**, *522*, 101.

[22] T.-H. Pham, J. J. Kim, S.-E. Kim, *Int. J. Mech. Sci.* **2015**, *90*, 151.

[23] H. E. Boyer, T. L. Gall, *Metals Handbook*, American Society for Metals, **1985**.

[24] T. Leitner, A. Hohenwarter, R. Pippan, *Mater. Sci. Eng., A* **2015,** *646*, 294.

[25] V. Maier, C. Schunk, M. Göken, K. Durst, *Phil. Mag.* **2015**, *95(16-18),* 1766.

[26] A. P. Zhilyaev, G. V. Nurislamova, B.-K. Kim, M.D. Baro, J.A. Szpunar, T.G. Langdon, *Acta Mater.* ***2003***, 51(3), 753.

[27] A. Khorashadizadeh, D. Raabe, M. Winning, R. Pippan, *Adv. Eng. Mater.* **2011**, 13(4), 245.

[28] D. B. Bober, A. Khalajhedayati, K. Mukul, T. J. Rupert, *Metall. Mater. Trans. A*, **2016**, 47(3), 1389.

[29] W. D. Nix, H. Gao, *J. Mech. Phys. Solids* **1998**, *46(3)*, 411.

[30] K. Durst, B. Backes, O. Franke, M. Göken, *Acta Mater.* **2006**, *54(9),* 2547.

[31] E. O. Hall, *Proc. Phys. Soc. London, Sec. B* **1951,** *64(9)*, 747.

[32] N. J. Petch, *J. Iron Steel Inst.* **1953**, *174*, 25.

[33] R. Armstrong, I. Codd, R. M. Douthwaite, N. J. Petch, *Phil. Mag*. **1962**, *7(73)*, 45.

[34] K. Durst, B. Backes, M. Göken, *Scripta Mater.* **2005**, *52(11),* 1093.

[35] N. A. Sakharova, J. V. Fernandes, J. M. Antunes, M. C. Oliveira, *Int. J. Solids Struct. **2009,*** 46(5), 1095.

[36] A. W. Thompson, *Acta Metal.* **1975**, *23(11)*, 1337.

[37] F. Ebrahimi, G. R. Bourne, M. S. Kelly, T. E. Matthews, *Nanostruct. Mater.* **1999,** *11(3)*, 343.

[38] X. Feaugas H. Haddou, *Metall. Mater. Trans. A* **2003**, *34(10)*, 2329.

[39] A. Godon, J. Creus, S. Cohendoz, E. Conforto, X. Feaugas, P. Girault, C. Savall, *Scripta Mater.* **2010**, *62(6),* 403.

[40] C. E. Carlton, P. J. Ferreira, *Acta Mater.* **2007**, *55(11)*, 3749.

[41] U. K. Vashi, R. W. Armstrong, G. E. Zima, *Metall. Trans.* **1970**, *1(6)*, 1769.

[42] K. Zhang, J. R. Weertman, J. A. Eastman, *Appl. Phys. Lett.* **2005**, *87(6).*

[43] W. Blum, Y. J. Li, *Scripta Mater.* **2007**, *57(5)*, 429.

[44] J. Wehrs, G. Mohanty, G. Guillonneau, A. A. Taylor, X. Maeder, D. Frey, L. Philippe, S. Mischler, J. M. Wheeler, J. Michler, *JOM* **2015**, *67(8)*, 1684.

[45] R. Schwaiger, B. Moser, M. Dao, N. Chollacoop, S. Suresh, *Acta Mater.* **2003**, *51(17)*, 5159.

[46] N. Krasilnikov, W. Lojkowski, Z. Pakiela, R. Valiev. *Mater. Sci. Eng., A* **2005**, *397(1-2),* 330.

[47] B. Yang, PhD thesis, Universität des Saarlandes, 66041 Saarbrücken, **2006**.

[48] G. B. Rathmayr, A. Hohenwarter, R. Pippan, *Mater. Sci. Eng., A* **2013**, *560*, 224.

[49] S. W. H. Yih, C. T. Wang. *Tungsten: sources, metallurgy, properties, and applications*, Plenum Publishing Corporation, **1979**.

[50] N. A. Stelmashenko, M. G. Walls, L. M. Brown, Y. V. Milman, *Acta Metall.* **1993**, *41(10),* 2855.

[51] E. Lassner, W.-D. Schubert, *Tungsten: properties, chemistry, technology of the element, alloys, and chemical compounds*, New York. Plenum Publishers, **1999**.

[52] Q. Wei, L. J. Kecskes, *Mater. Sci. Eng., A* **2008**, *491(1-2)*, 62.

[53] S. Bonk, J. Reiser, J. Hoffmann, A. Hoffmann, *Int. J. Refract. Met. Hard Mater* **2016**, *60*, 92.

Publication C

Dynamic nanoindentation testing: is there an influence on a material's hardness?

A. Leitner[1], V. Maier-Kiener[2], D. Kiener[1]

Materials Research Letters 5:7 (2017) 486-493

[1] Department Materials Physics, Montanuniversität Leoben, Austria
[2] Department Physical Metallurgy and Materials Testing, Montanuniversität Leoben, Austria

C - Abstract

Modern nanoindentation devices are capable of dynamic experimentations which allow to exploit instrumented hardness tests extensively. Beside the assets of recording mechanical properties continuously over displacement, there are ongoing debates whether the superimposed force alters the material’s hardness. We will show for a broad range of materials that significant hardness differences are noted between dynamic and static tests, even for large displacements. Those mainly result from a changing indentation strain-rate during the hold segment at peak load. This fact must be implicitly considered in studies using static indentation tests to guarantee comparability of obtained nanoindentation hardness values and derived quantities.

C - Introduction

Hardness as a mechanical property is a convenient parameter to assess a material’s strength, since it is intuitive that a harder material will be able to penetrate a softer material, but not vice versa [1]. Nowadays, it is possible to maximize the output of instrumented indentation experiments, since the contact stiffness and thereby also the material’s hardness and Young’s modulus can be obtained continuously over indentation depth [2–6]. This depth dependent data can further be useful to state the reliability of measurements or to correct for thermal drift during long-time test [7,8], since the used dynamic technique is less sensitive to thermal drift problems [5,9]. To continuously access the stiffness of the material it is unavoidable to manipulate the force signal by superimposing an oscillating force with diminutive amplitude where the phase shift between load and displacement signal will allow to calculate the elastic stiffness [2,3,10], often referred to as continuous stiffness measurement (CSM) or dynamic indentation testing. While the technical implementation of this oscillation is current state-of-the-art, there is still an ongoing debate on whether this superimposed signal influences the mechanical properties of materials. Therefore, several comprehensive studies investigated the impact of amplitude level and frequency on the obtained mechanical properties [10–16]. Differences in hardness values for low indentation depths with comparable large oscillation amplitudes have been noted several times [13,15,16]. They occur when the superimposed force amplitude is significant compared to the indentation depth and when measurements are executed with rather low oscillation frequencies, indicating partial loss of contact. However, discrepancies are also conceivable at high loads and displacements and should be examined to exclude contact issues. Still comparative and systematic studies performed on identical samples and nanoindentation devices are lacking in literature. Within the present study, we investigate the differences among nanoindentation testing methods with and without CSM with focus on deep indentations thus, excluding possible surface effects. We demonstrate for a broad selection of materials that the hardness difference is mainly dependent on the material inherent strain-rate sensitivity m of the tested sample rather than the used indentation technique. In future, this matter needs to be consistently considered in the data analysis of static nanoindentation tests.

C - Experimental

To assess the influence of lattice type and microstructure, materials listed in Table 1 were selected for the investigations. Additionally, this selection covers large intervals of hardness *H*, Young's modulus *E* and strain-rate sensitivity *m* values. Ultra-fine grained materials were fabricated by High Pressure Torsion [17–19] and nanocrystalline (NC) Ni by electrodeposition [20], while melt grown single crystals and coarse grained materials were tested as received from suppliers. The microstructures were investigated and analyzed by optical microscope imaging, electron backscatter diffraction or X-Ray diffraction. Additionally, fused quartz and glassy carbon (GC) were tested to examine whether the impact of CSM can also be noted on amorphous ceramic samples. Details of used specimens can be obtained from former studies [8,15,21,22].

Indentation tests were conducted on a Keysight G200 Nanoindenter equipped with CSM option and a diamond Berkovich indenter tip to obtain *H* and *E* by the conventional analysis firstly proposed by Oliver and Pharr [3]. For each material two different types of tests were executed. On the one hand, constant strain-rate CSM measurements with a frequency of 45 Hz and a displacement amplitude of 2 nm were performed to determine the mechanical properties continuously over displacement. The indentation strain-rate $\dot{\varepsilon}$ was set to 0.05 s^{-1}. On the other hand, tests with multiple unloading sequences (eight unloading regimes distributed over 2500 nm of indentation depth) without CSM, denoted as load controlled (LC) tests in this study, also allow to extract eight pairs of *E* and *H* within one single indent. The hold time at maximum load was set to 5 s, the time to load was set to 15 s, resulting in about same indentation strain-rate for all materials [23]. LC and CSM measurements were executed consecutively with the same tip area function to exclude any errors from different tip shapes and calibrations which could potentially falsify the investigated effect. Additionally, the mechanical properties obtained by CSM where analyzed at the same displacement as the corresponding LC measurements to avoid influences of indentation size effects [24]. Moreover, single load controlled experiments without CSM were executed for Cr SX and Ni SX to check whether thermal drift or multiple load-unload segments are a potential source of error. At least five indents were performed for each set of parameters. For all materials a maximum displacement of 2500 nm was used, with the exception of FQ, UFG Cr, UFG W and GaAs where the force limit of 660 mN was reached earlier ($h_{max,FQ}$ = 2400 nm, $h_{max,UFG\ Cr}$ = 2470 nm, $h_{max,UFG\ W}$ = 2000 nm, $h_{max,GaAs}$ = 2300 nm). Thermal drift did not exceed 0.1 nm/s for any considered indentation. Occurring hardness differences for different test methods were obtained at maximum common displacement. Strain-rate jump tests were conducted to determine *m,* following the work of Maier et al. [25]. An overview of the used samples and their properties is given in Table 1.

Table 1: Investigated material selection, covering face-centered cubic (FCC), body-centered cubic (BCC) and hexagonal closed packed (HCP) metals as well as fused quartz, glassy carbon and GaAs. The Young's moduli were obtained from CSM measurements, m-values from nanoindentation jump tests.

Material	***Lattice type***	***Microstructure***	***Young's modulus E***	***Strain-rate sensitivity m***
Au	FCC	SX (1 0 0)	75 ± 1 GPa	0.008 ± 0.001
Au	FCC	UFG 250 nm	79 ± 2 GPa	0.017 ± 0.002
Cu	FCC	SX (1 1 1)	121 ± 2 GPa	0.005 ± 0.001
Ni	FCC	SX (1 0 0)	196 ± 2 GPa	0.003 ± 0.002
Ni	FCC	NC 30 nm	205 ± 2 GPa	0.021 ± 0.001
V	BCC	UFG 200 nm	144 ± 1 GPa	0.013 ± 0.001
Ta	BCC	SX (1 0 0)	169 ± 1 GPa	0.045 ± 0.005
Fe	BCC	CG 100 µm	195 ± 2 GPa	0.015 ± 0.001
Cr	BCC	SX (1 0 0)	293 ± 5 GPa	0.050 ± 0.003
Cr	BCC	UFG 300 nm	291 ± 2 GPa	0.013 ± 0.001
W	BCC	SX (1 0 0)	397 ± 7 GPa	0.030 ± 0.002
W	BCC	UFG 890 nm	407 ± 9 GPa	0.024 ± 0.002
Zr	HCP	CG 45 µm	109 ± 1 GPa	0.026 ± 0.003
Zr	HCP	UFG	127 ± 2 GPa	0.024 ± 0.002
Ti	HCP	CG 55 µm	125 ± 1 GPa	0.025 ± 0.003
Ti	HCP	UFG	192 ± 3 GPa	0.014 ± 0.002
GaAs	Zinc blende	SX	114 ± 1 GPa	0.043 ± 0.003
Glassy C	-	amorphous	34 ± 1 GPa	0.014 ± 0.002
FQ	-	amorphous	72 ± 1 GPa	0.010 ± 0.001

C - Results & Discussion

Two representative hardness profiles of the different measurement types for Ni SX and Cr SX are displayed in Figure 1. Both materials show a distinct indentation size effect as expected for SX [24]. It can evidently be noted that while for Ni SX the hardness values for all test types coincide over the entire displacement range, a significant deviation between LC and CSM data appears for Cr SX. Multiple loading tests do not differ from single loading tests at maximum displacement, indicating that drift can be excluded as a potential source of error, as the multiple holding segments increase the test time and would amplify any drift influences.

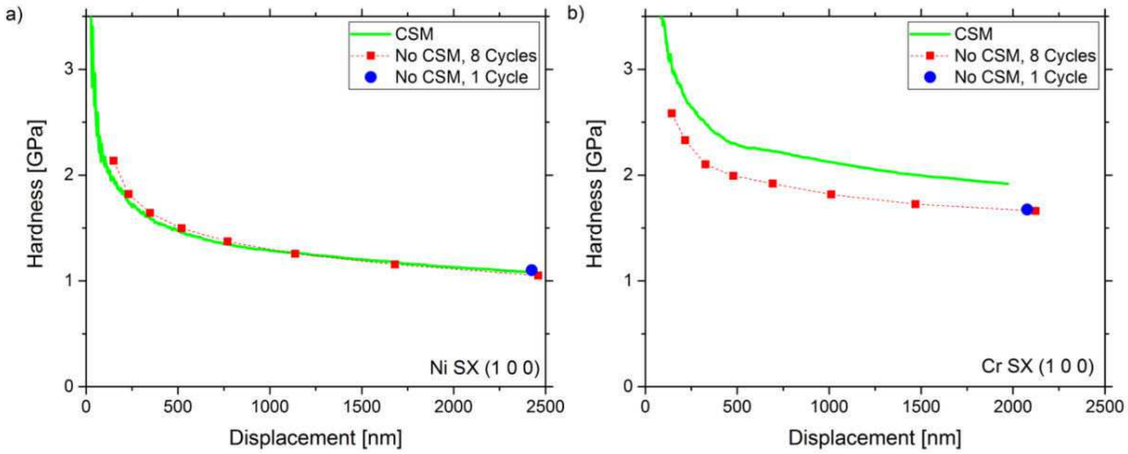

Figure 1. Comparison of hardness - displacement profiles for a) Ni SX and b) Cr SX for tests with and without CSM. Evidently, the different techniques result in significantly different *H* levels for Cr SX but not for Ni SX.

One could think that the crystal structure (FCC versus BCC in Figure 1) may be the decisive factor, but also measurements on FCC metals with refined microstructures show a significant hardness difference between CSM and LC tests. To analyze this behavior in more detail, we overlay the two load-displacement curves from CSM and LC measurements on top of each other, as shown in Figure 2. The plastic loading curves match well, thus the mismatch in hardness for Cr SX must originate from the holding regime. The increase in the displacement *Δh* during these hold segments is referred to as indentation creep, the amount of which in turn is linked to the strain-rate sensitivity of the materials. This suggests that the effect may result from a changing strain-rate during the hold segment, as the effect is less pronounced for rate-insensitive Ni SX in Figure 2 a). Before this circumstance is discussed in detail, the definition of the indentation strain-rate shall briefly be revisited.

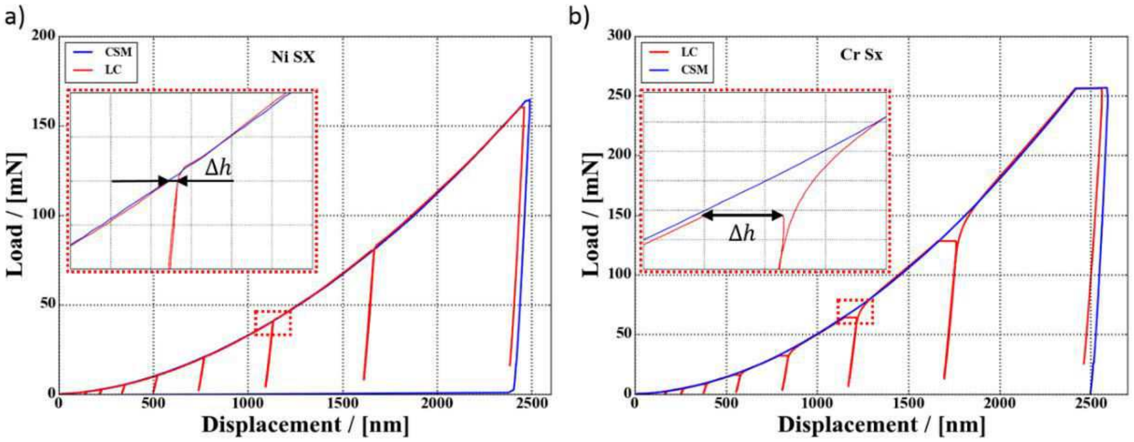

Figure 2. Load - displacement curves of LC (multiple unloading) and CSM measurements on Ni SX and Cr SX demonstrate that the hardness difference originates from the dwell segments of the LC tests (see the insets), while the plastic loading curves match up well.

Since the indentation strain is conventionally assumed to be only dependent on the tip geometry, self-similar pyramidal tips, such as the used Berkovich tip, introduce the same strain independent of the indentation depth. Hence, the strain-rate is not defined by the temporal increase of the strain itself but as the expansion of the self-similar plastic zone through the material. As this parameter is experimentally not accessible, alternatively the indentation strain-rate can be defined as [26]:

$$\dot{\varepsilon} = \frac{\dot{h}}{h} = \frac{1}{2} \cdot \left(\frac{\dot{P}}{P} - \frac{\dot{H}}{H} \right) \approx \frac{1}{2} \cdot \frac{\dot{P}}{P} \qquad (1)\ ,$$

where $\dot{h},\ \dot{P},\ \dot{H}$ are the time derivatives of the load, displacement and hardness, respectively. The fact that this study investigates differences at high displacements is essential for the accuracy of this work since tip imperfections, often noted for low depths, lead to deviations from the self-similar geometry and could unpredictably alter the physical strain-rate [27]. However, the approximation in the last step is strictly spoken only valid for materials with constant hardness over displacement or materials where the hardening rate $\dot{H}$ is negligible low compared to the corresponding hardness. Figure 3 shows the difference of the evaluated strain-rate during the hold segment by either the definition of displacement or definition of load, respectively. Particularly during the dwell segment, the approximation breaks down as the load is held constant and consequently the strain-rate converges to zero (see Figure 3). Nevertheless, the right part of equation (1) is generally used since this parameter is easier to trigger for common nanoindentation devices. During the hold segment the strain-rate will be dominated by the change of hardness or the change of displacement, respectively, clearly making the definition $\dot{P}/P$ unfeasible in this regime.

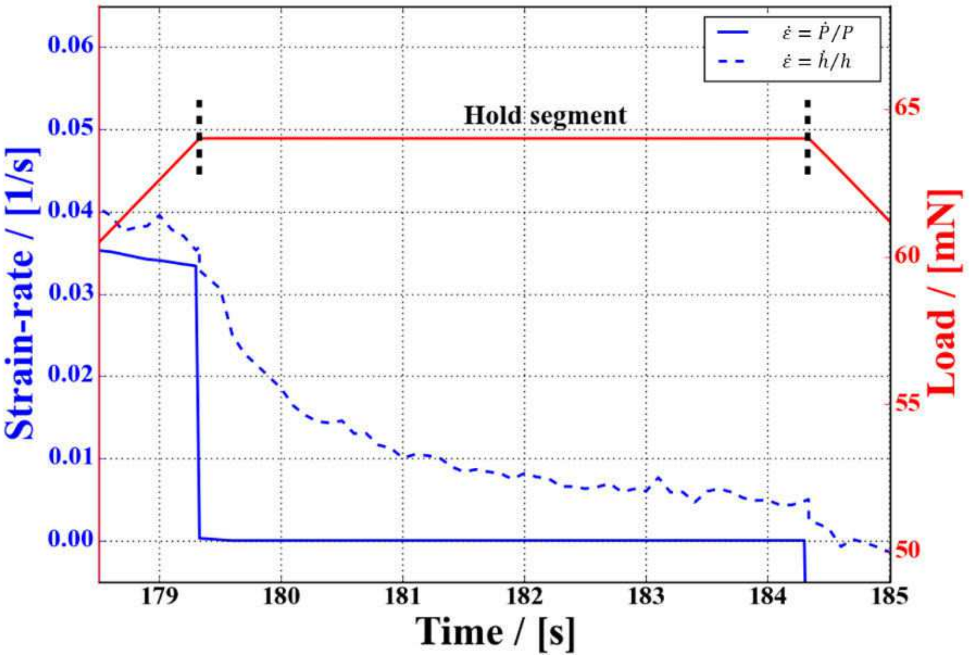

Figure 3. Development of the actual indentation strain-rate defined as $\dot{h}/h$, in contrast to the approximate solution $\dot{P}/P$ for a hold segment of a quasi-static indentation experiment. Evidently, the approximate $\dot{P}/P$ solution breaks down during constant load regimes.

As evident from Figure 3, the strain-rate at which the hardness value is evaluated from, has to be inevitably considered. Following the analysis of Oliver and Pharr [3], the material stiffness is required to compute the real area in contact to account for the elastic sink-in during indentation. For LC measurements, this requires the unloading curve and therefore the mechanical properties can only be determined at the point of unloading, which is assigned to the corresponding strain-rate at this point. As seen from Figure 3 and Figure 4, this strain-rate can be significantly different from the strain-rate during loading and naturally varies in dependence of the hold time. This behavior enables to obtain *m* in nanoindentation creep tests [7,26,28,29]. In contrast, the CSM technique allows to determine the hardness at the set $\dot{\varepsilon}$ value during loading. Figures 4 a)-c) give a detailed view of the strain-rate profiles for the conducted testing methods, showing that for the case of Cr SX the strain-rate difference turns out to be more than one order of magnitude for the 5 s hold segments.

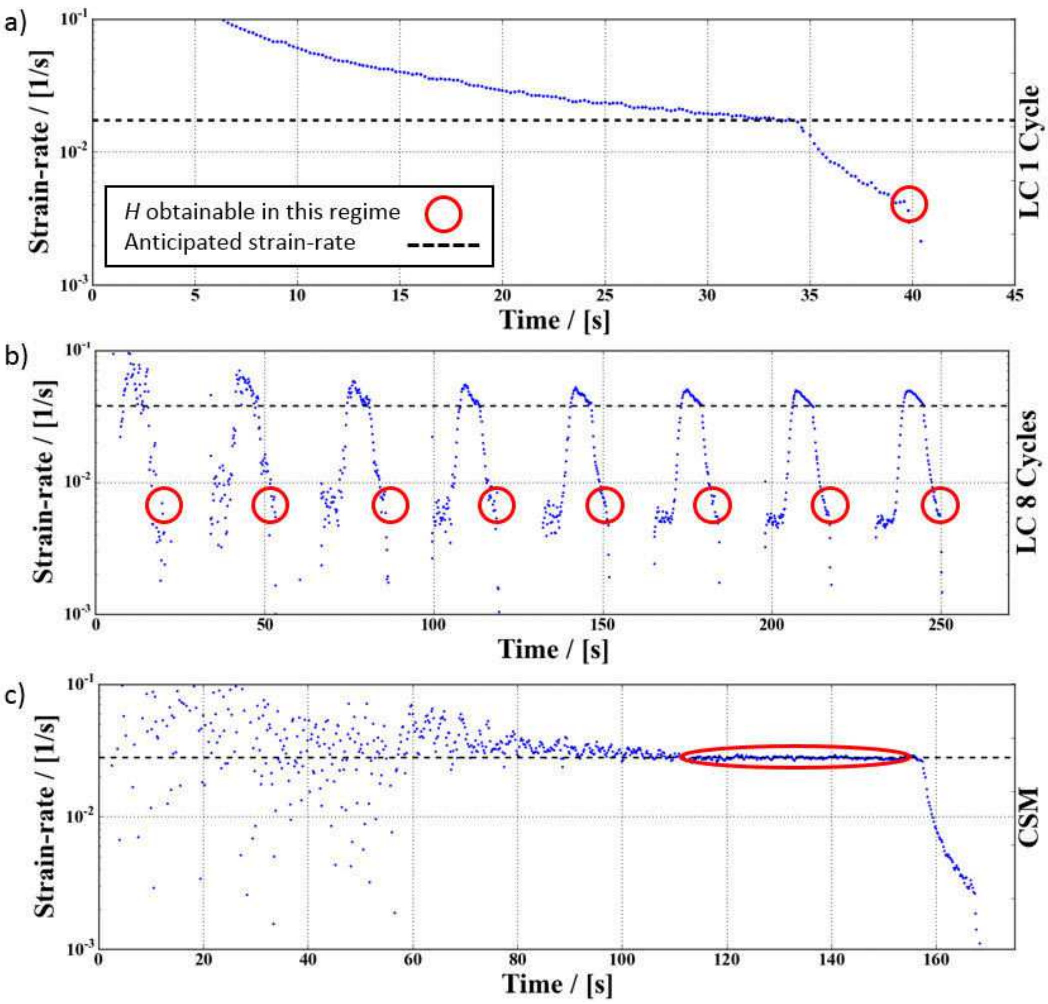

Figure 4. a)-c) Strain-rate profiles of three common nanoindentation techniques for Cr SX. The red circles indicate the range that can be used to obtain mechanical properties by the Oliver & Pharr analysis. Note that for dynamic (CSM, c)) testing the anticipated strain-rate is achieved, while for static (LC, a)-b)) tests it differs by one order of magnitude.

If we assume that the hardness deviations between the testing protocols emerge from the strain-rate changes, we can calculate the expected hardness difference if the strain-rate sensitivity is known. Using the common power-law for the strain-rate sensitivity dependent hardness [30–32] one derives:

$$\begin{aligned} H_1 &= K \cdot \dot{\varepsilon}_1{}^m \\ H_2 &= K \cdot \dot{\varepsilon}_2{}^m \end{aligned} \qquad \dot{\varepsilon}_1 > \dot{\varepsilon}_2 \tag{2}$$

$$\Delta H = \frac{H_1 - H_2}{H_1} = \frac{K \cdot (\dot{\varepsilon}_1{}^m - \dot{\varepsilon}_2{}^m)}{K \cdot \dot{\varepsilon}_1{}^m} = 1 - \left(\frac{\dot{\varepsilon}_2}{\dot{\varepsilon}_1}\right)^m \tag{3}$$

According to equation (3), this should lead to an increasing hardness difference between LC and CSM tests with increasing strain-rate sensitivity. This is evident in Figure 5 a), where the difference between CSM and LC hardness is shown in dependence of the strain-rate sensitivity of the materials. The closed symbols depict the experimentally measured hardness difference, while the open symbols represent calculated results from equation (3). Therefor actual strain-rates were determined at the depths used for the analysis with the according *m* values of Table 1. It is noted that the displayed data in Figure 5 a) is for a constant hold time of 5 s, meaning that the ratio $\dot{\varepsilon}_2/\dot{\varepsilon}_1$ varies depending on the material. The data follows the predicted behavior from equation (3), strain-rate insensitive such as FCC SX materials show only slight differences, while highly rate-dependent such as BCC or fine-grained materials show large differences. Cr SX was used to experimentally prove whether this strain-rate effect is decisive. The strain-rate during the 5 s hold regime of the LC test (Figure 3) was determined and resulted in a value of 0.005 s^{-1} at the point of unloading. Subsequently this strain-rate was set in a CSM test. Figure 5 b) shows fairly good agreement between the hardness - depth profiles for the LC experiments and the low strain-rate CSM experiments, which confirms the dominance of the described strain-rate effect. Considering the actual strain-rates from the load-displacement data rather than the preset values, the difference in hardness reduces to an average value of 2.5%. Still, CSM measurements show slightly but noticeable higher hardness values compared to LC measurements which might result from a weak hardness dependence of *m*, as known from nanoindentation creep experiments [7,8,29]. This fairly small systematic difference could also emerge due to differences in the loaded material structure between LC, where a stable microstructure is unloaded, and CSM, where the microstructural evolution is based on a dynamic equilibrium structure.

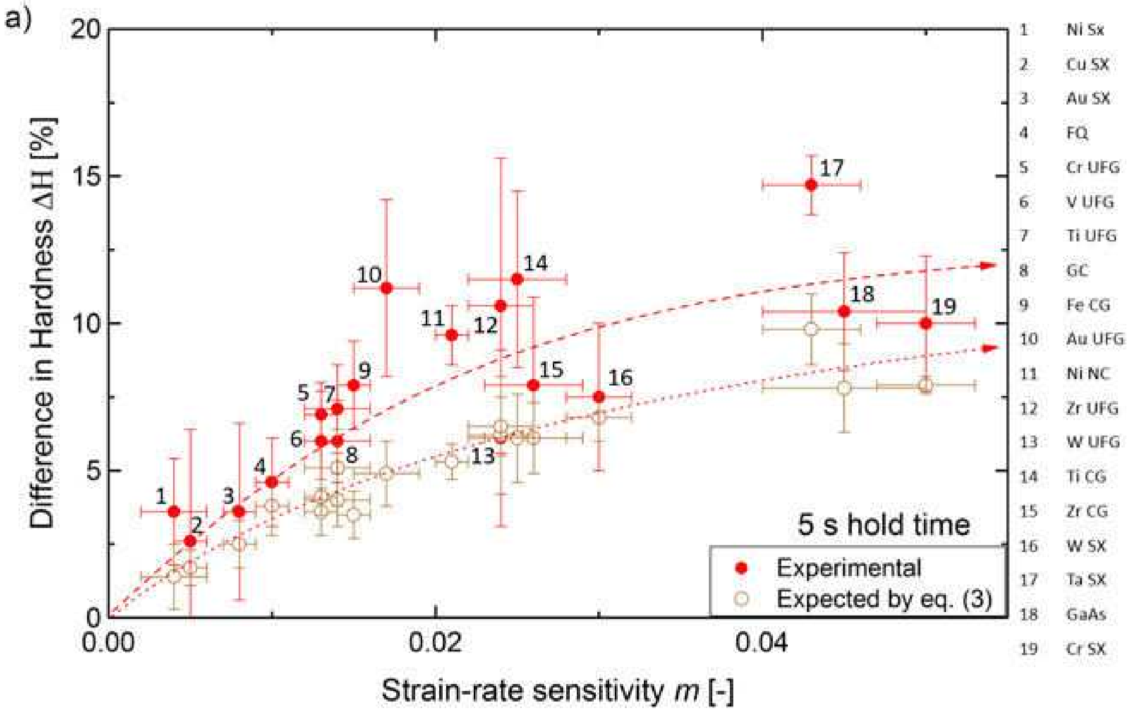

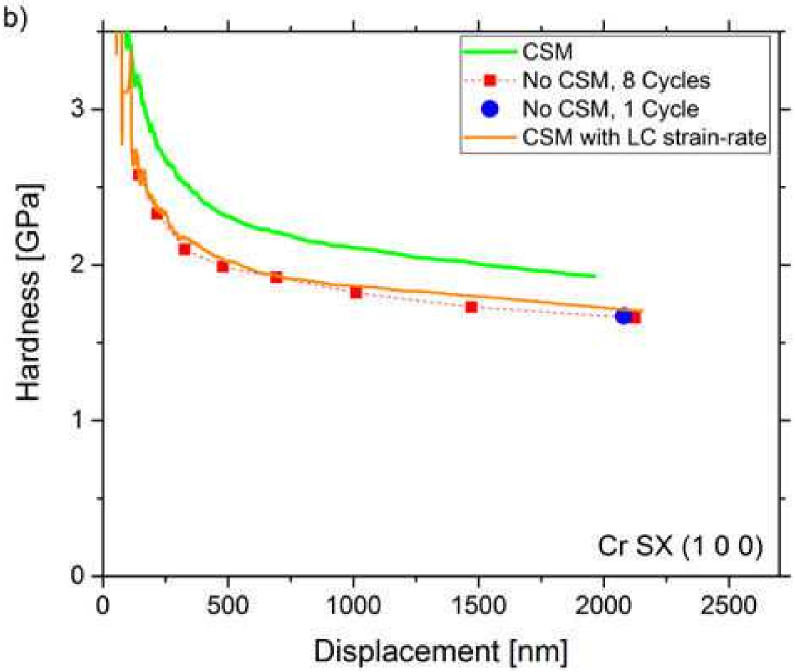

Figure 5. a) Experimental and theoretical hardness difference as expected from equation (3) between static and dynamic tests in dependence of the strain-rate sensitivity. b) Low strain-rate CSM experiments confirm that the hardness difference is mainly rooted in differing strain-rates used to determine the hardness.

C - Summary & conclusion

To the best knowledge of the authors, hardness differences between static LC and dynamic CSM tests are a matter of debate, but have never been systematically examined. Within this study, a broad spectrum of materials including FCC, BCC, HCP metals, semiconductor and amorphous materials has been investigated at high displacements, thus excluding any possible surface artefacts. As demonstrated here, LC results can significantly deviate from CSM measurements for strain-rate sensitive materials. We confirm that this effect is mainly attributed to the changing strain-rate during dwell segments of static LC tests rather than to any changes in the material's microstructure. Considering this matter considerably decreases the mismatch down to an average level of only 2.5%. It is tremendously important to consider this rate-effect, otherwise the hardness differences could misleadingly be ascribed to the force oscillation.

This finding implies broad-ranging consequences for indentation testing of rate-sensitive materials. It also exemplifies the challenges and requirements when comparing literature values from static nanoindentation testing techniques. Also, the determination of m by static nanoindentation constant strain-rate experiments is disputable. The specified strain-rates with the definition $\dot{P}/P$ for LC tests do not represent the actual occurring strain-rate as long as peak hold times are part of the measurement protocol, which is the standard implementation. In fact, such data only indicates the upper limit of the strain-rate. Therefore, we strongly recommend obtaining the actual indentation strain-rate at the end of the hold segment. This can effortlessly and accurately be determined from the load-displacement data and guarantees accurate and comparable results.

However, still there remains a hardness gap with slightly higher *H* values for CSM measurements which could conceivably be attributed to slightly differing microstructures between static and dynamic conditions or a slight hardness dependence *m*. In addition, the discussed effect has been investigated at rather large indentation depths, but does not necessarily depict the situation at shallow depths, where the displacement amplitude of the CSM signal is considerably large compared to the indentation depth [13,15,16]. In such a situation, the hardness value will be influenced additionally from changes in the contact stiffness, which will further complicate the identification of the underlying physical effects in a rate-sensitive material. Addressing this matter is, however, beyond the scope of the present work.

C – Acknowledgements

Funding of the Styrian and the Tyrolean Provincial Government, represented by Steirische Wirtschaftsförderungsgesellschaft mbH and Standortagentur Tirol, within the framework of the COMET Funding Programme (837900, MPPE A7.19) is appreciated. Furthermore, parts of this work were also funded by the Austrian Science Fund (FWF) via the project P25325-N20.

C - References

[1] Mohs F. Versuch einer Elementar-Methode zur naturhistorischen Bestimmung und Erkennung der Foßilien. Camesina; 1812.

[2] Pethica JB, Oliver WC. Mechanical Properties of Nanometre Volumes of Material: use of the Elastic Response of Small Area Indentations. MRS Proc. 1988;130:13–23.

[3] Oliver WC, Pharr GM. An improved technique for determining hardness and elastic modulus using load and displacement sensing indentation experiments. J. Mater. Res. 1992;7:1564–1583.

[4] Asif SAS, Wahl KJ, Colton RJ. Nanoindentation and contact stiffness measurement using force modulation with a capacitive load-displacement transducer. Rev. Sci. Instrum. 1999;70:2408–2413.

[5] Li X, Bhushan B. A review of nanoindentation continuous stiffness measurement technique and its applications. Mater. Charact. 2002;48:11–36.

[6] Oliver WC, Pharr GM. Measurement of hardness and elastic modulus by instrumented indentation: Advances in understanding and refinements to methodology. J. Mater. Res. 2004;19:3–20.

[7] Maier V, Merle B, Göken M, et al. An improved long-term nanoindentation creep testing approach for studying the local deformation processes in nanocrystalline metals at room and elevated temperatures. J. Mater. Res. 2013;28:1177–1188.

[8] Maier V, Leitner A, Pippan R, et al. Thermally Activated Deformation Behavior of ufg-Au: Environmental Issues During Long-Term and High-Temperature Nanoindentation Testing. JOM. 2015;67:2934–2944.

[9] Asif SAS, Pethica JB. Nano Scale Creep and the Role of Defects. MRS Proc. 1996;436.

[10] Hay J, Agee P, Herbert E. Continuous Stiffness Measurement during instrumented indentation testing. Exp. Tech. 2010;34:86–94.

[11] Cheng Y-T, Ni W, Cheng C-M. Nonlinear Analysis of Oscillatory Indentation in Elastic and Viscoelastic Solids. Phys. Rev. Lett. 2006;97:75506.

[12] Durst K, Franke O, Böhner A, et al. Indentation size effect in Ni-Fe solid solutions. Acta Mater. 2007;55:6825–6833.

[13] Cordill MJ, Moody NR, Gerberich WW. Effects of dynamic indentation on the mechanical response of materials. J. Mater. Res. 2008;23:1604–1613.

[14] Pharr GM, Strader JH, Oliver WC. Critical issues in making small-depth mechanical property measurements by nanoindentation with continuous stiffness measurement. J. Mater. Res. 2009;24:653–666.

[15] Cordill MJ, Lund MS, Parker J, et al. The Nano-Jackhammer effect in probing near-surface mechanical properties. Int. J. Plast. 2009;25:2045–2058.

[16] Siu KW, Ngan AHW. Oscillation-induced softening in copper and molybdenum from nano- to micro-length scales. Mater. Sci. Eng. A. 2013;572:56–64.

[17] Valiev RZ, Islamgaliev RK, Alexandrov I V. Bulk nanostructured materials from severe plastic deformation. Prog. Mater. Sci. 2000;45:103–189.

[18] Pippan R, Scheriau S, Hohenwarter A, et al. Advantages and Limitations of HPT: A Review. Mater. Sci. Forum. 2008;584–586:16–21.

[19] Zhilyaev AP, Langdon TG. Using high-pressure torsion for metal processing: Fundamentals

and applications. Prog. Mater. Sci. 2008;53:893–979.

[20] Bicelli LP, Bozzini B, Mele C, et al. A review of nanostructural aspects of metal electrodeposition. Int. J. Electrochem. Sci. 2008;3:356–408.

[21] Leitner T, Hohenwarter A, Pippan R. Revisiting fatigue crack growth in various grain size regimes of Ni. Mater. Sci. Eng. A. 2015;646:294–305.

[22] Fritz R, Maier-Kiener V, Lutz D, et al. Interplay between sample size and grain size: Single crystalline vs. ultrafine-grained chromium micropillars. Mater. Sci. Eng. A. 2016;674:626–633.

[23] Durst K, Maier V. Dynamic nanoindentation testing for studying thermally activated processes from single to nanocrystalline metals. Curr. Opin. Solid State Mater. Sci. 2015;19:340–353.

[24] Nix WD, Gao H. Indentation size effects in crystalline materials: A law for strain gradient plasticity. J. Mech. Phys. Solids. 1998;46:411–425.

[25] Maier V, Durst K, Mueller J, et al. Nanoindentation strain-rate jump tests for determining the local strain-rate sensitivity in nanocrystalline Ni and ultrafine-grained Al. J. Mater. Res. 2011;26:1421–1430.

[26] Lucas BN, Oliver WC. Indentation power-law creep of high-purity indium. Metall. Mater. Trans. A. 1999;30:601–610.

[27] Bucaille JL, Stauss S, Felder E, et al. Determination of plastic properties of metals by instrumented indentation using different sharp indenters. Acta Mater. 2003;51:1663–1678.

[28] Alkorta J, Martínez-Esnaola JM, Sevillano JG. Critical examination of strain-rate sensitivity measurement by nanoindentation methods: Application to severely deformed niobium. Acta Mater. 2008;56:884–893.

[29] Peykov D, Martin E, Chromik RR, et al. Evaluation of strain rate sensitivity by constant load nanoindentation. J. Mater. Sci. 2012;47:7189–7200.

[30] Tabor D. The Hardness of Metals. OUP Oxford; 1951.

[31] Hart EW. Theory of the tensile test. Acta Metall. 1967;15:351–355.

[32] Wei Q, Cheng S, Ramesh KT, et al. Effect of nanocrystalline and ultrafine grain sizes on the strain rate sensitivity and activation volume: fcc versus bcc metals. Mater. Sci. Eng. A. 2004;381:71–79.

Publication D

Essential refinements of spherical nanoindentation protocols for the reliable determination of mechanical flow curves

A. Leitner[1], V. Maier-Kiener[2], D. Kiener[1]

Submitted to a SCI journal

[1] Department Materials Physics, Montanuniversität Leoben, Austria
[2] Department Physical Metallurgy and Materials Testing, Montanuniversität Leoben, Austria

D - Abstract

Understanding and linking mechanical properties obtained by spherical indentation experiments to uniaxial data is extremely challenging. Since the first attempts in the early 20th century numerous advances gradually allowed to expand the output of indentation tests. Still, the extraction of flow curves from spherical nanoindentation has not yet been fully established, as tip shape problems and size effects impede a straight-forward implementation. Within this study, we show new calibration procedures originating from fundamental geometrical considerations to account for tip shape imperfections. This sets the base for strain-rate controlled tests, which in turn enables us to measure rate-dependent material properties either with constant strain-rate or by strain-rate jump tests. Finally, experimental evaluation of the constraint factor in consideration of the mechanical properties and induced strain enables the extraction of flow curves. Testing materials with refined microstructures ensures the absence of possible size-effects. This study contributes to a significant improvement of current experimental protocols and allows to move flow curve measurements from single spherical imprints one step closer to its implementation as a standard characterization technique for modern materials.

D - Introduction

Fast, comprehensive and reliable mechanical characterization of materials gains significance to keep pace with the rapid developments in engineering and material science disciplines. However, contrary to conventional materials, modern high-performance components, microelectronics or functional materials are often produced at a laboratory bench scale or by bottom-up techniques which must cope with local variations of mechanical properties. These structures owe their strength and functionality to specific local micro- and nanoscale features. Fundamentally understanding such materials often requires highly localized measurements, which are also important once higher-level simulation techniques are involved that necessitate stress-strain curves as an input. Hence, a micromechanical technique is required to comply with the needs of minimal material consumption, high local sensitivity and cost-effectiveness but at the same time maximum exploitation of data while maintaining high reliabilities.

Instrumented indentation with its long history [1–6] is well established nowadays and one of the most promising candidates to meet these requirements. Besides, it is available in almost any modern material research lab, main assets are straight-forward sample preparation and highly automatized procedures. Therefore nanoindentation has become a standard technique to measure the hardness H and the Young's modulus E of materials [2,7]. Since dynamic indentation setups became available, elastic and plastic properties can continuously be recorded over displacement [2,8–11] and allow to assess the reliability of tests on isotropic samples or to account for thermal drift influences during long term-tests [12]. Highly hydrostatic stress fields emerge underneath the indenter tip [13] and consequently also enable characterization of brittle materials at high strains.

The flip side of nanoindentation is mainly the occurrence of length scale effects such as geometry dependent indentation size effects which complicate the analysis [14–18]. Also, the fabrication of precise tip shapes is a challenging task. Considering that indentation tips should be extremely hard and stiff only a few ceramic materials can be used. Finally, in terms of flow curve extraction the complex multi-axial stress and strain field imposed by indentation [13,19,20] impedes a straight-forward analysis.

Revealing the flow behavior of materials can principally be attempted in two different ways. On the one hand, various self-similar indenter tips, such as pyramids or cones, with varying opening angle can be used to obtain discrete points along the stress-strain curve [20–25]. However, this study will focus on a nanoindentation approach utilizing spherical tips which cause a non-self-similar stress field under the tip and thus induce a continuously increasing representative strain with increasing indentation depth. Numerous advances have been made in the analysis of spherical indentation curves since Tabor stated in the early 1950s that the hardness can be related to the stress of uniaxial flow curves [21,26]. The present study will revisit spherical indentation approaches and essentially refine and extend existing procedures to lastly enable this technique to serve as an equivalent to elaborate micromechanical uniaxial testing methods such as micropillar compression [27]. For this purpose, new calibration procedures will be introduced which allow the depth-independent determination of the Young's modulus despite tip imperfections. Subsequently, the importance of constant strain-rate experiments will be highlighted, accompanied by a comparison of existing standard testing protocols. We will demonstrate that the presented refinements facilitate the reliable determination of rate-dependent properties by using both, a constant strain-rate approach or strain-rate jump tests, respectively. Finally, scaling the constraint factor in an experimentally informed manner by utilizing the ratio of unloading and loading slopes of nanoindentation load-displacement curves will provide a physically based concept to convert nanoindentation flow curves to flow curves that are in excellent agreement with uniaxial tests.

State-of-the-art nanoindentation analysis for spherical indentation

Numerous studies have been published in the past decades which perceptibly advanced spherical nanoindentation approaches [13,21,26,28–38]. Progresses shall briefly be summarized at this point. Nowadays, the Meyer's hardness is widely considered as appropriate definition of H, where the projected area is used [39] instead of the area in touch with the sample commonly used in Brinell tests. Furthermore, the elastic distortion contribution which can be significant in small scale tests, is accounted for and consequently allows to separate plastic and elastic regimes from load-displacement data at maximum load [2–4,6,13]. Still, elastic deformation during loading may change the corresponding area in contact, hence an effective radius can be used to take this issue into account [33,34]. Kalidindi and Pathak made use of dynamic indentation protocols where they evaluated the contact area A_c from the stiffness of isotropic samples (reduced modulus E^* is constant) [29–31] based on the equation derived by Sneddon [4]

$$E^* = \frac{\sqrt{\pi}}{2} \cdot \frac{S}{\sqrt{A_c}} \qquad \text{equation (1),}$$

with S as the stiffness, and thus could indicate tip shape problems. Additionally, they redefined the representative indentation strain to [29–31]

$$\varepsilon_i = \frac{4 \cdot h}{3 \cdot \pi \cdot a_c} \qquad \text{equation (2),}$$

with h as the total displacement and a_c as the contact radius, which can be derived from Hertz's law for elastic contact in contrast to the empirical relation from Tabor [21]

$$\varepsilon_i = 0.2 \cdot \frac{a_{(C)}}{R_{(eff)}} \qquad \text{equation (3),}$$

with $R_{(\mathrm{eff})}$ as the radius or effective radius [33,34] of the tip and $a_{(C)}$ as the contact radius or the radius of the residual impression. Both lead to a dependency of the opening angle with respect to a certain displacement. By applying a zero-point correction in the elastic regime to exclude effects from surface artefacts, one can obtain the effective point of initial contact, providing a correct elastic Hooke's line in the determined indentation stress-strain curves [29–31].

The determination of the representative indentation stress σ_r is challenging. A linear conversion between the mean pressure or hardness, respectively, and stress has been suggested by Tabor [21]

$$H = C^* \cdot \sigma_r \qquad \text{equation (4),}$$

where C^* is the constraint factor.

However, nowadays there is general agreement in literature [13,20,21,32,40–46] that C^* itself depends on the ratio E^*/σ and the indentation strain, and that it increases with increasing strain and E^*/σ values up to a plateau-value of around 3.

D - Testing setup & used samples

Nanoindentation experiments of the present study were performed on a Keysight G200 with integrated continuous stiffness measurement (CSM) unit. Dynamic measurements were carried out with a displacement amplitude of 2 nm oscillating at 45 Hz in order to minimize errors caused by the system's lock-in amplifier [47]. It is important to note that by using the CSM unit the hardness can be obtained over displacement and hence hardness values correspond to the set strain-rate. This is not the case for H values obtained with multiple unloading tests, where the strain-rate drops in the hold regime of each cycle and might falsify results of rate-sensitive materials [48]. All nanoindentation tips were obtained from Synton MDP LTD, Nidau, Switzerland. For reference measurements, a Berkovich diamond tip was used for 2500 nm deep indentations with a set strain-rate of 0.05 s^{-1} to determine hardness and Young's modulus according to the conventional analysis of Oliver and Pharr [2]. Berkovich strain-rate jump tests [49] were performed using strain-rates of 0.05 s^{-1}, 0.005 s^{-1} and 0.001 s^{-1} for displacement regimes of 500 nm each. Top-ground diamond cone tips with a half opening angle of 45° were used as spherical tips with specified radii R_{spec} ranging from 5 µm to 60 µm. Mentioned radii in the text refer to the R_{spec} of the corresponding tip. Strain-rate profiles for spherical tip experiments will be presented below. Thermal drift was measured in a post-test segment at 10% of the maximum load and did not exceed 0.2 nm/s for any indent. The data acquisition rate was set 5 Hz. At least six indents were performed for each parameter set, and in the following figures representative results will be shown.

Micropillars used for comparison of uniaxial flow characteristics were milled with a Ga focused ion beam with an aspect ratio of 2.5 to 3. Taper-free rectangular UFG W (3.5 x 3.5 µm²) and UFG Cr (3.5 x 3.5 µm²) were fabricated in a dual-beam SEM-FIB (Zeiss LEO 1540 XP, Oberkochen, Germany). Details and corresponding stress-strain curves were previously reported from by Fritz et al. [50,51]. Cylindrical NC Ni (Ø 4.5 µm) and UFG Cu (Ø 4.9 µm) were prepared by annular milling (Zeiss Auriga Platform, Oberkochen, Germany) and tested at the G200 nanoindenter using a diamond flat punch as tip (Ø 10) µm and utilizing a goniometer based stage as suggested by Uchic and Dimiduk to correct for misalignments [52]. No sample size effect is expected due to reduced grain sizes of theses samples combined with rather large pillar dimensions [53–55].

The suitability and requirements of tested materials shall briefly be discussed at this point. The presented tip calibration is universally applicable and not restricted to an internal length scale). The material selection for this part includes glassy carbon, fused quartz (FQ), fine-grained (FG, grain-size (GS): 1.05 µm ± 0.25 µm) 6014 Al-alloy, ultrafine-grained (UFG, GS: 0.28 µm ± 0.14 µm) copper, nanocrystalline (NC) (GS: 30 nm) nickel, UFG (GS: 0.3 µm ± 0.1 µm) chromium and UFG (GS: 0.89 µm ± 0.51 µm) tungsten. This selection includes amorphous, face-centered cubic (FCC) and body-centered cubic (BCC) materials of varying grain-size. For investigations of strain-rate effects the accumulative roll bonded (8 repeats) 6014 Al-alloy [56] was used since its enhanced strain-rate sensitivity *m* will contribute to clearly visible implications. Furthermore, constant strain-rate tests were conducted on a (1 0 0)-oriented GaAs wafer due to its homogeneity and pronounced pop-in effects [57,58].

Despite the undisputable benefits of spherical indentation, some challenges come along with its use as characterization technique, as the obtained properties also depend on the microstructural dimensions of the tested material. Size effects referring to the sphere radius for coarse grained structures complicate the extraction and flow curves and cannot easily be subtracted from the data. However, most modern materials make use of reduced internal length-scale which lead to enhanced strength while maintaining sufficient ductility [59–62]. In terms of flow curve extraction, this study aims to extract nanoindentation flow curves for ultra-fine grained and nanocrystalline materials where loaded volumes are representative already at shallow indentation depths. Hence, anisotropy and indentation size effects will only play a negligible role. NC Ni, UFG Cu, UFG Cr and UFG W, spanning in grain-size from ~30 nm to ~1 µm, were used for flow curve extraction experiments.

D - Novel methodical approaches

Subsequent paragraphs deal with refinements and extensions of current spherical nanoindentation protocols. New tip calibration approaches and strain-rate controlled experiments detailed here will serve as a solid base for the reliable extraction of spherical nanoindentation flow curves later.

Tip calibrations

Fabrication of spherical tips using hard and stiff materials, such as diamond or sapphire, is an ambitious task since these materials are predominantly anisotropic. Even though deviations from the specified shape are generally small, they may cause major problems in nanoindentation experiments. For instance, the correct tip shape will be needed to conduct constant strain-rate tests, as the strain depends on the ratio between displacement and contact radius according to equation (2). To overcome tip shape problems, one principle idea is to replace the specified radius with an effective radius to extend the applicability of the calibration to the elastic-plastic regime [33,34]. Back-calculating the contact area from the stiffness signal (see equation (1)) is an appropriate approach but requires a priori knowledge of E^* and adds perceptible noise to the data [12,29–31,63].

Analysis of 3D profiles recorded by a laser confocal microscope (Olympus LEXT OLS4100, Tokyo, Japan) reveals the non-perfect tip shape of a new spherical tip (Figure 1a). An SEM image (see inlay of Figure 1b) of the spherical tip shows that the body is rather an ellipsoid than a spherical segment which should be considered in the analysis. Hence, the use of a single number for the radius of a tip is insufficient. Still, Rspec will be referred to keep the tips assignable, but only serves as a rough qualitative number of the tip dimension which will not be used in any analysis. Alike sharp indenter tips, one preferably calibrates each tip to obtain individual area functions using an elastically isotropic material such as fused quartz. For sharp tips, this can accurately be done using the series [2]

$$A_c(h_c) = \sum_{i=0}^{i} B_i \cdot h_c^{1/2^{i-1}} \qquad \text{equation (5).}$$

Considering a perfect tip, the geometry constants B_1 to B_i become zero and $B_0 = 3 \cdot \sqrt{3} \cdot tan^2(\alpha)$, where α is the complementary angle between the normal vector of the pyramid face and the loading direction. This function type is notably useful for sharp tips since the terms after the lead term will mainly account for tip imperfections at shallow depths which is the most problematic regime for sharp tips. Nevertheless, it turns out that this approach is not as reliable for spherical tips because these tips differ in their sphericity. Hence, the shape can also crucially deviate at large displacements, which is the reason why a geometry based area function should be favored. Basic geometrical considerations allow to express the area as a function of the displacement, using following equations with a as the radius of the projected area, R as the sphere radius and h as displacement:

$$A = a^2 \cdot \pi \qquad \text{equation (6),}$$

$$a^2 = 2 \cdot R \cdot h - h^2 \qquad \text{equation (7).}$$

Combining these equations, and considering the real area in contact instead of the total displacement [2], indicated by the index c, this leads to

$$A_c(h_c) = B_0 \cdot {h_c}^{B_1} - B_2 \cdot h_c^2 \qquad \text{equation (8),}$$

which properly describes a perfect sphere if $B_0 = 2 \cdot R \cdot \pi$, $B_1 = 1$ and $B_2 = \pi$. To describe imperfect tips, the constants B_i can be varied using a non-linear least square method. Note that the variation of one exponent is important to vary the sphericity of the tip shape. Another fundamental asset of using this type of function is that starting values for the parameters B_i in these non-linear least square methods have a physical meaning as they refer to the radius of the idealized tip. Consequently, this leads to faster convergence and high numeric stability of the procedure. Still, fitting parameters may slightly differ depending on the least-square method. In this study, a Levenberg-Marquardt algorithm [64,65] (routine implemented in the Python package SciPy) was used for this purpose and consistently provides satisfying results resulting in coefficients of determination greater than 0.985 for any conducted calibration. Generally, as the tip shape itself differs from that of a sphere, the current analysis based on Sneddon's studies should be favored [4] which is analogue to the widely accepted calibration method proposed by Oliver and Pharr [2]. Compared to Hertzian analysis [33,34,66] there is no need to extend the analysis to the plastic regime where the curvature of the residual indent has to be approximated.

Furthermore, one should not forget that spherical tips are often made from a cone as semifinished part. If the total opening angle of the base-cone is 90°, as it is the case in this study, a spherical shape can only be provided up to a displacement of $h = R \cdot \left(1 - \frac{1}{\sqrt{2}}\right)$, indicated in Figure 1b. At this point the slope of the sphere tangent matches the cone half angle and for larger displacements indentation strain will not increase anymore.

Correct calibrations are confirmed by horizontal profiles of the Young's modulus over displacement. Figure 1b shows a comparison between doubtful results obtained using the specified radius, and parameters from the new calibration procedure, which is well in agreement with literature values for fused quartz [2]. Even if the specified radius would be replaced by a slightly smaller radius this would only lead to a parallel translation of the green curve and still exhibit the strong unphysical gradient in modulus at shallow depths. Elastic distortions or material pile ups around the indent may occur depending on the material. Regrettably, one cannot entirely exclude this effect, but Figure 1c clearly demonstrates that *E*-values, spanning from 35 GPa to 400 GPa, are conform with reference values obtained by Berkovich tests and literature data [2,67,68], thus pile-up and sink-in behavior seem to be of minor importance.

Once the real tip shape is known, due to this improved calibration the influence of different strain-rates can be investigated as will be done in the following section.

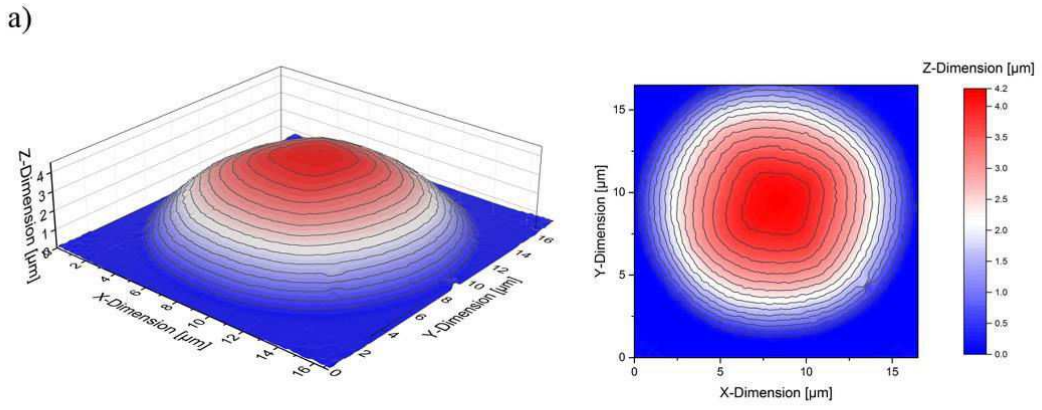

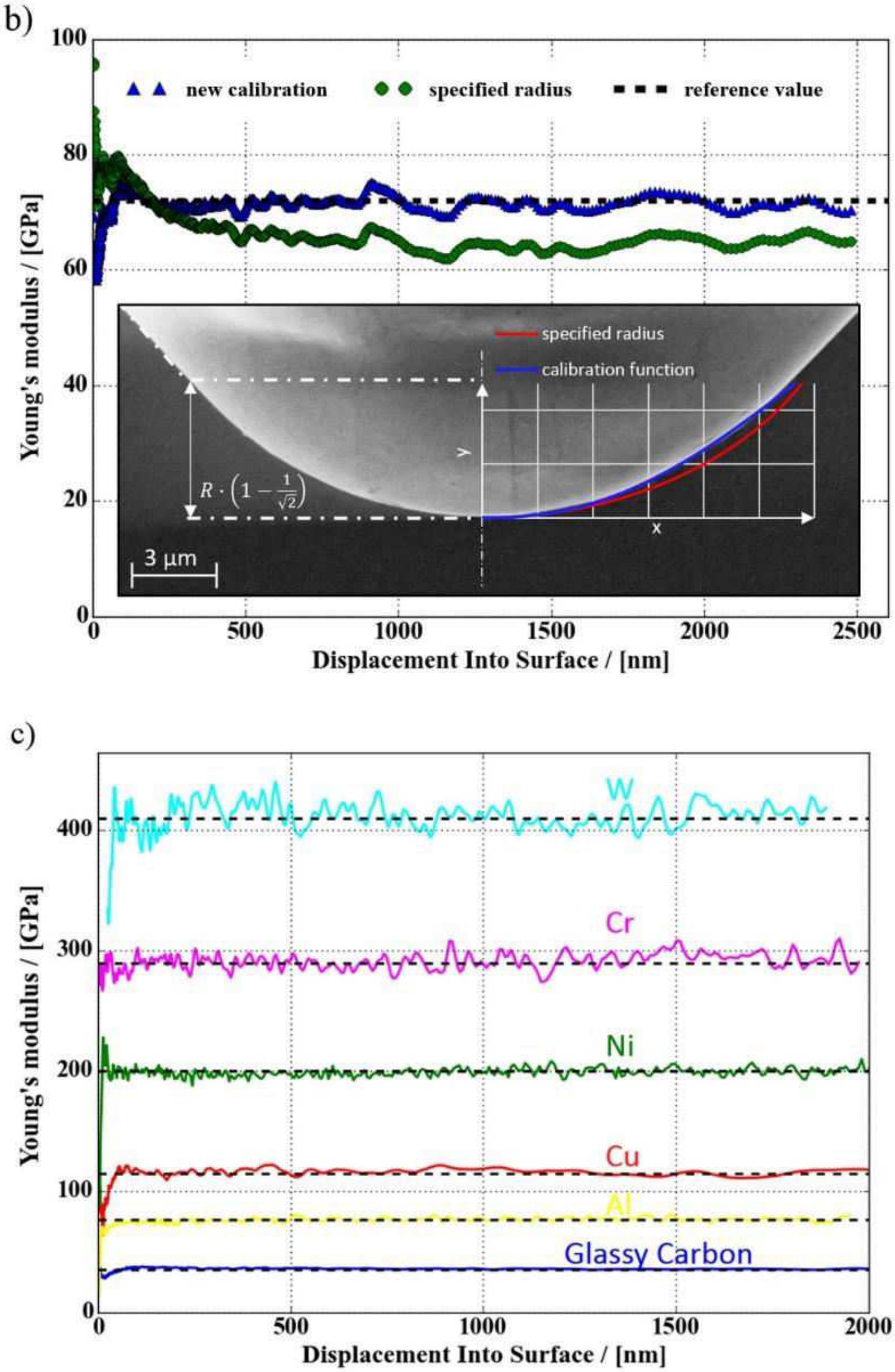

Figure 1. a) 3D profile of a spherical tip obtained by a laser confocal microscope reveals the non-perfect tip shape. b) Profile of the Young's modulus of FQ over displacement using the specified tip radius (green circles) to calculate the contact area and by the described new calibrated area function (blue triangles). The inset SEM micrograph of a spherical tip (20 µm radius) shows the limit of the spherical shape and that in contrast to a perfect sphere the new area function matches the tip contours well. c) Horizontal profiles of the Young's modulus on various isotropic materials indicate valid measurements for samples with a broad spectrum of *E* ranging from 35 GPa (Glassy Carbon) to 400 GPa (W). The black dashed lines represent reference Berkovich values for the tested materials.

Strain-rate controlled experiments in spherical indentation

In most modern high-performance metals deformation is not simply governed by athermal dislocation plasticity, but rate-dependent mechanisms are responsible for high strength properties. Thus, controlling the strain-rate in experiments is crucial to obtain useful flow curves. For nanoindentation tests the definition of the strain or strain-rate, respectively, is not straightforward and certainly depends on the used tip. The definition of the strain for spherical tips has been discussed several times in the past, however, the definition used by Pathak and Kalidindi [29–31] seems currently to be the most convincing one. In their spherical nanoindentation study, they could demonstrate that the expected Hooke's line can be measured for W and Al single crystals prior to pop-in events. The advantage of only considering the elastic regime is clearly that the hardness is conform with the stress in the material, since the hydrostatic pressure contributes to elastic deformation.

The strain is given by equation (2). Naturally, the load-time profile in nanoindentation tests must be adapted to this definition to guarantee a correct strain-rate. Nanoindentation devices are often load-controlled, hence controlling via the time derivative of equation (2) can be challenging. Feldner et al. first addressed the problem of a varying strain-rate during spherical indentation [37]. They used equation (1) & (2) combined with the assumption of an elastic contact and a perfect sphere to end up in a strain-rate proportional to $\dot{P}/P^{2/3}$, with $\dot{P}$ the time derivative of the load. This parameter is similar to that used in sharp indentation experiments ($\dot{\varepsilon} = \dot{P}/P$) to tune the strain-rate [37,69] and easily controllable with the used indentation device. Even though this reduces the strain-rate induced error, the assumptions impair the success of the approach.

Within this study, we successfully implemented strain-rate controlled experiments according to the strain definition of equation (2) over a few orders of magnitude by tuning the proportional-integral-derivative parameters of the integrated PID-control. The proposed area function in beneficial in this context as a simple form will favor a fast PID-feedback. Achievable strains and strain-rates depend on the radius and area function of the sphere, thus by our definition also tip imperfections are considered for a correct strain-rate. Figures 2a-c display strain, strain-rate and hardness profiles for different testing methods measured with a 5 µm radius tip according to specifications. Constant strain-rate experiments at 0.002 s^{-1} have been performed accompanied by a linear increase of strain over time (Figure 2a) and a constant strain-rate in Figure 2b. Using the definition for sharp indenter tips ($\dot{P}/P$ = const.) and a set strain-rate 0.05 s^{-1} leads to a continuous increase of the strain-rate over displacement, while the strain-rate of constant load-rate (cLR) experiments using 0.75 mN/s are monotonically decreasing. Figure 2c shows the corresponding hardness profiles which go along with the strain-rate profiles of Figure 2b. One can see in the magnified inset that the cLR hardness curve at first intersects the profile which uses the strain-rate definition of sharp tips ($\dot{P}/P$ = const.) at about 500 nm (arrow 1) and subsequently the profile of constant strain-rate (cSR) tests at around 1500 nm (arrow 2) just as it happens for the strain-rates in Figure 2b. As one might expect, when tested at the same strain-rate the flow stresses match. Figure 2c thereby evidences that work hardening behavior obtained from spherical indentation will significantly be falsified if the strain-rate is not adequately considered for rate sensitive materials making the implementation of cSR tests crucial for any spherical indentation study dealing with rate-sensitive materials such as bcc or nanocrystalline metals. However, only for the cSR data this value is constant throughout the test. Note that the inputs for load-rate, sharp tip strain-rate and spherical tip strain-rate have been chosen to come down to similar testing times. Independent of the absolute input values all trends would remain the same.

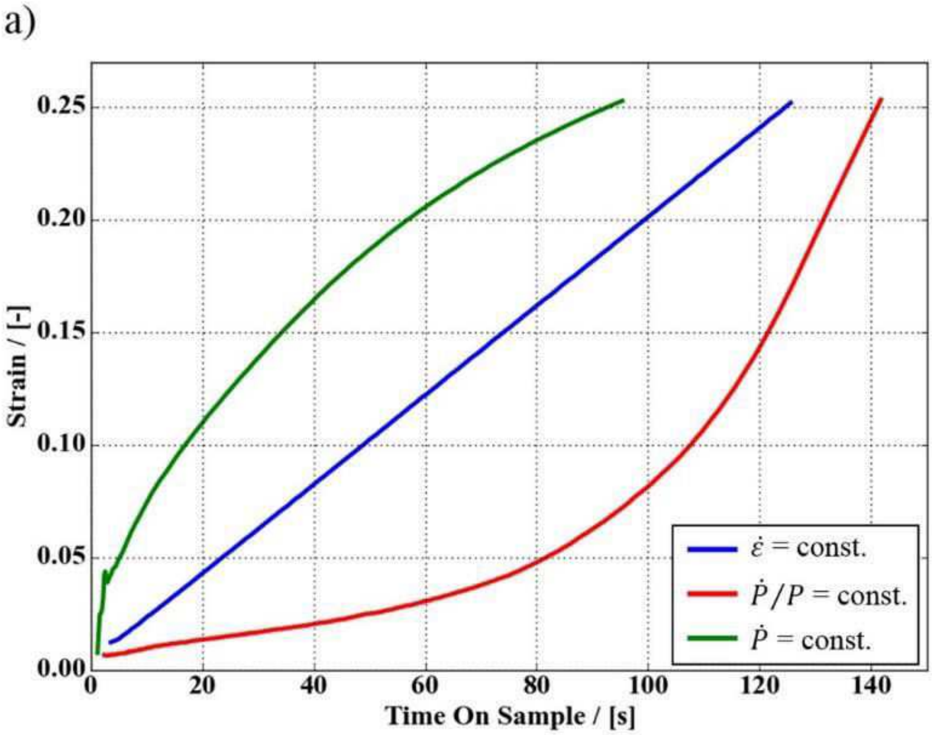

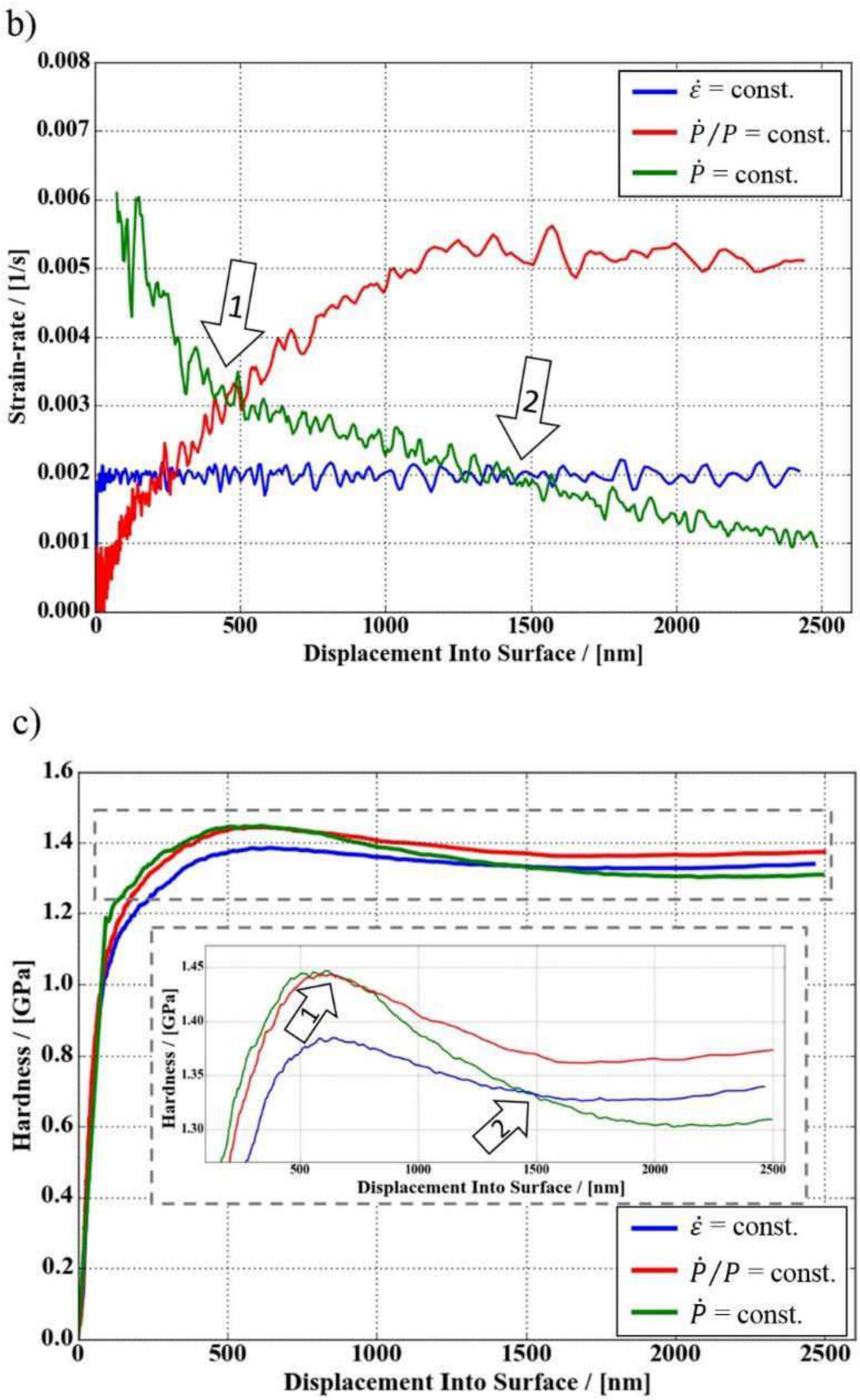

Figure 2. a & b) Temporal profiles of the indentation strain show the linear increase for cSR tests (blue) yielding to constant strain-rate while cLR (green) and $\dot{P}/P$ (red) experiments end up in a continuously decreasing and increasing strain-rate, respectively. c) Resulting hardness curves of the 6014 Al-alloy demonstrate the strong dependence of the strain-rate for spherical tests. Intersects of the hardness match the intersects of the strain-rates in b).

Once the strain-rate is properly considered, spherical indentation experiments turn out to be extraordinarily stable and reliable. Note the marginal deviations in Figure 3a which displays the hardness curves of three indentations performed with a 10 µm radius tip on NC Ni at a strain-rate of 0.0005 s^{-1}, resulting in testing times of about 360 s. The well-known tip size effect of coarse grained materials is attributed to geometric necessary dislocations which need to be created to accommodate the tip in the material. This model assumes that dislocation loops form around the penetrating tip [14,18]. For the materials with small grain sizes this effect can be excluded as the length of dislocation loops by far exceeds the microstructural dimensions also at shallow depths. Figure 3b demonstrates that for NC Ni, where representative volumes are tested instantaneously, tip size effects are negligible since spherical tips with radii of 10 µm, 20 µm and 50 µm lead to matching hardness profiles.

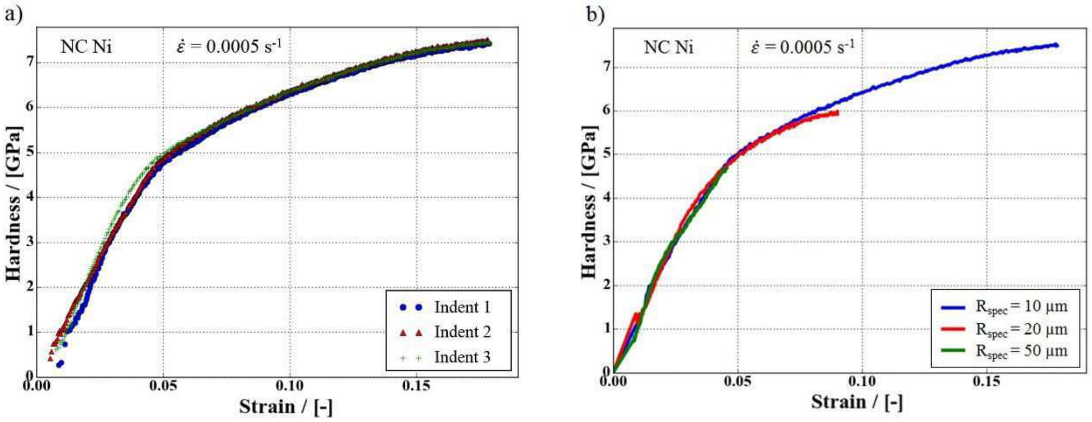

Figure 3. a) Hardness curves of three different indents on NC Ni illustrate the high reliability of the technique. b) Hardness-strain profiles obtained on NC Ni with three different indenter tip radii using a strain-rate of 0.0005 s^{-1} verifies that mechanical properties can be determined independent of the used radius.

Rate-dependent properties

Understanding spherical indentation and controlling the strain-rate enables the method to characterize samples regarding thermally activated mechanisms. Considering equation (4) and assuming *C** constant at a representative strain, one can proof the equivalence between the logarithmic hardness and representative stress difference, respectively:

$$\begin{aligned}\Delta \ln H = \ln H_2 - \ln H_1 &= \ln(\sigma_2 \cdot C^*) - \ln(\sigma_1 \cdot C^*) \\ &= \ln(\sigma_2) + \ln(C^*) - \ln(\sigma_1) - \ln(C^*) = \Delta \ln \sigma\end{aligned}$$

equation (9),

which finally allows to calculate the strain-rate sensitivity *m* according to [70,71]

$$m = \frac{\Delta \ln \sigma_r}{\Delta \ln \dot{\varepsilon}} = \frac{\Delta H}{\Delta \ln \dot{\varepsilon}}$$

equation (10).

Different approaches can be used to determine the strain-rate sensitivity or activation volume of a material. On the one hand, various indents with different constant strain-rates can be executed, which is time consuming but allows to determine *m* in dependence of the imposed strain. To verify this method, a GaAs wafer was used in this study since the properties of this material are well suited to double-check the reliability. The sample features an enhanced strain-rate sensitivity but is additionally highly homogeneous and contains few defects. Hence, distinct pop-ins are expected, which will indicate the start of plastic deformation [57,58]. Up to this point, the deformation will be purely elastic and consequently the hardness or stress values, respectively, should not differ in dependence of the used strain-rate. Additionally, stress-strain profiles should accord to Hook's line and comply with the Young's modulus measured by the CSM signal or with measurements from standard Berkovich indentation. After the point of yield, a significant difference in hardness is expected, depending on the strain-rate. Figure 4a demonstrates cSR tests conducted with a 5 µm radius tip on GaAs. Just as expected above, the indentation data exhibits all the features mentioned above for indents performed with 0.01 s^{-1}, 0.001 s^{-1} and 0.0005 s^{-1}. Consistent Hooke lines also ensure dependable analysis of *m* since strain-offsets could significantly change results. Figure 4b shows that the strain-rate sensitivity determined using the 0.01 s^{-1} and 0.0005 s^{-1} data is constant over strain. Hence, Berkovich nanoindentation jump tests, ascribed to a representative strain of around 7%, can be well compared to spherical experiments, all of which resulting in the same *m*-value of 0.043 ± 0.003. Notably, for the sphere only values starting from 14% strain can be used since the rapid pop-in process causes slight deviations from the anticipated strain-rate before.

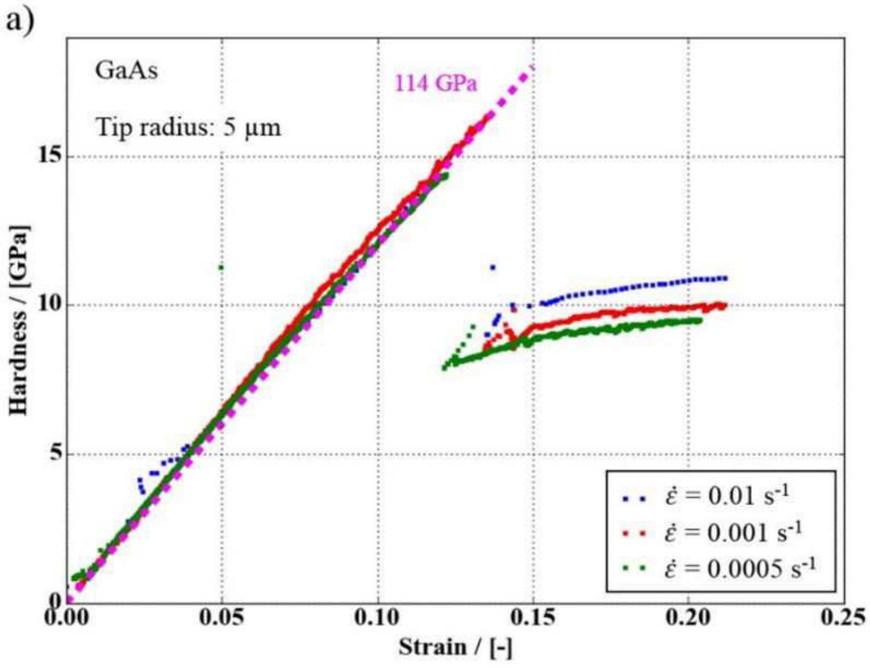

b)

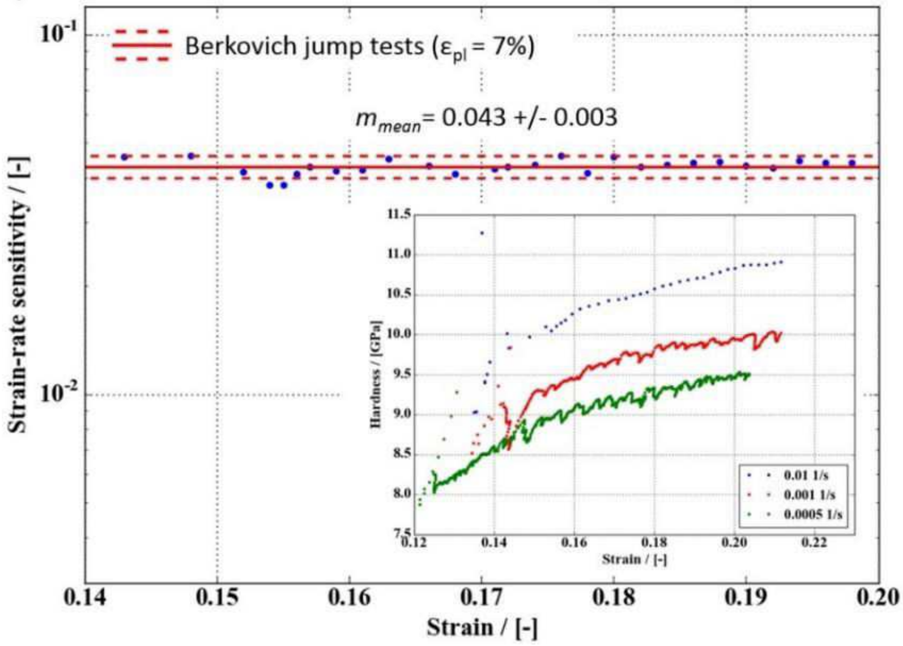

Figure 4. a) Hardness over indentation strain for experiments on GaAs. During the elastic loading prior to pop-in events the hardness is equal to the stress, thus Hooke’s line with the corresponding Young’s modulus of 114 GPa is imprinted as a dashed line. In the plastic regime after pop-in, magnified in the inset in b), a distinct rate-dependence can be noted. Analysis of *m* over strain shows a strain-independent value of 0.043, conform with Berkovich jump tests ascribed to a representative strain of 7%.

Elaborate test schedules are necessary to gain rate-dependent properties using the cSR method at different rates. However, strain-rate jump tests can now also be implemented for spherical indentations as already demonstrated by Feldner et al., even though they had a challenging situation since they calculated the contact radius from the stiffness assuming a constant modulus [37]. This goes along with distinct noise of the stiffness signal and complicates the analysis of the strain-rate jumps. Within this study, using the new calibration procedure, we can avoid this problem and extend the technique also to material with unknown or varying elastic properties. Figure 5 shows a hardness-strain plot for an ARB FG Al-alloy (6014) which, as common for refined FCC metals, shows a pronounced strain-rate sensitivity. The GaAs SX sample is not suited for this testing method as the pop-in occurring at rather high strains impedes the use of multiple strain-rate regimes required for the analysis. Red dots indicate the strain-rate during the tests while the red dashed line highlights the levels of the anticipated strain-rates of 0.005 s^{-1}, 0.001 s^{-1} and 0.0005 s^{-1}, which are constantly achieved. Solely during slowing down the strain-rate slight undershoots can be noted. Analysis of nine jump tests, only considering the last three jumps each, ends up in 27 hardness/strain-rate pairs which lead to an *m*-value of 0.024 ± 0.004, conform to values obtained by reference Berkovich jump tests of 0.024 ± 0.002.

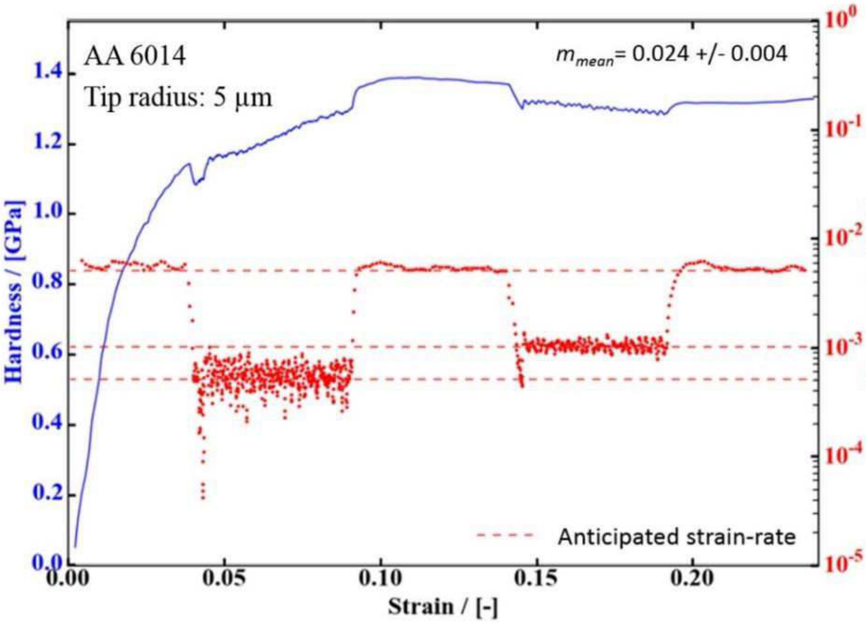

Figure 5. Spherical indentation strain-rate jump tests for an ARB Al alloy (6014). The strain-rate profiles (red dots) clearly demonstrate that the anticipated strain rates (red dashed lines) are reached for every segment of 5% strain.

D - Flow curve extraction

After ensuring reliable measurements by knowing the actual tip shape and controlling the strain-rate, the implication is to transform the hardness-strain profiles to stress-strain curves also in the plastic regime. This demanding task has been attempted several times before, also including FEM simulation supported methods [13,20,21,32,40–46]. The international organization of standardization (ISO) addressed this topic in a comprehensive technical report [72], even though aspects such as tip imperfections and strain-rate effects are not considered and the suggested methods to link indentation to uniaxial properties always rely on computational techniques. Extensive experimental approaches on samples with small internal length-scales, where size effects are insignificant, are seldom. And ideally, uniaxial compression tests should be performed on the identical sample for comparison. The main difficulty towards unambiguous flow curves from indentation is the conversion from hardness to a representative indentation stress value even though it has often been demonstrated that this constraint factor C^* is in the order of 3 for metals. As mentioned above, the constraint factor varies dependent on elastic (E^*) and plastic properties (yield stress σ_y) as well as the indentation strain. The value of the representative strain varies depending on the used definition (Tabor [21] or Kalidindi and Pathak [29]), but scales with $\cot \Theta$, where Θ is the opening angle of the tip at a certain displacement (details see Appendix A). Table 1 gives an overview of C^* dependencies in literature for both spherical and sharp indenter tips, neglecting effects from work hardening or friction.

Table 1: Dependencies of the indentation constraint factor used in previous studies.

Authors	**Dependency of C***
Tabor [20]	$\boldsymbol{C^{*} = const.}$
Johnson [13]	$\boldsymbol{C^{*} = f(\frac{E^{*}}{\sigma_y} \cdot \cot\theta)}$
Fleck and Mesarovic [31]	$\boldsymbol{C^{*} = f(\frac{E^{*}}{\sigma_y} \cdot \frac{2 \cdot \cot\theta}{1+\cot^2\theta})}$
Hay et al. [40]	$\boldsymbol{C^{*} = f(\frac{E^{*}}{H} \cdot \cot\theta)}$
Park and Pharr [22]	$\boldsymbol{C^{*} = f(\frac{E^{*}}{\sigma_y} \cdot \frac{2 \cdot \cot\theta}{1+\cot^2\theta})}$
Mata et al. [43]	$\boldsymbol{C^{*} = f(\frac{E^{*}}{\sigma_y} \cdot \cot\theta)}$
Kang [45]	$\boldsymbol{C^{*} = f(\frac{E^{*}}{\sigma_y} \cdot \frac{2 \cdot \cot\theta}{1+\cot^2\theta})}$
Chen and Vlassak [66]	$\boldsymbol{C^{*} = f(\frac{E^{*}}{\sigma_y} \cdot \cot\theta)}$
Rodriguez et al. [44]	$\boldsymbol{C^{*} = f(\frac{E^{*}}{\sigma_r})}$

In some studies, differentiation whether the constraint factor links the hardness to the stress at the representative strain or to the initial yield stress of a material is not obvious. Most of the approaches require an a priori knowledge of the yield stress of the sample, which would certainly be a shortcoming of the used spherical indentation approach. Only Hay et al. [41] and Rodriguez et al. [45] linked *C** to the representative stress or hardness, respectively. The parameter used by Hay et al. [41] is particularly appealing, as it is directly related to the plastic and elastic work introduced and clearly distinguishes the elastic and plastic regime. Furthermore, it can be experimentally obtained from indentation measurements if CSM is used by calculating the ratio of the contact stiffness *S* and the slope of the load/contact depth curve n_L, called μ in this study

$$\mu = \frac{S}{n_L} = \frac{E_r}{H} \cdot \frac{\cot\theta}{\pi} \qquad \text{equation (11).}$$

See Appendix B for details. This parameter was also identified by Johnson to be proportional to the plastic zone size occurring during indentation [13]. It can be converted to the dimensionless parameter (see appendix A)

$$\mu' = \frac{E_r}{\sigma} \cdot \frac{a_c}{R} \qquad \text{equation (12),}$$

which has been identified to have a major impact on the value of *C** [13,32,44,46,73].

Uniaxial tests will now be used to determine a genuine function for *C**=f(μ) for spherical indentation experiments on pillars. This function can be determined by matching the indentation flow curve to the uniaxial pillar flow curve. For this purpose, the stress-strain curve from pillar compression tests and hardness-strain curves from spherical indentation tests were subdivided in strain increments $\Delta\varepsilon$ of 0.001 and used for the calculation of *C** according to equation (4). A 10 µm radius tip and NC Ni has been used for this procedure, since deformation will then mainly take place in the elastic-plastic transition regime, but also reaches the fully plastic regime at high strains. Considering the elastic/plastic work ratio μ yields in the profile depicted in Figure 6, which is in accordance to the expected shape from FEM studies [32,73] and can be subdivided in four regimes as firstly suggested by Park and Pharr [73]. Using μ instead of μ' reduces the purely elastic state (I) to a single point at μ=0.5 and *C**=1. Increasing the strain puts the deformed volume in the transition regime which is at first elastically dominated (pseudo Hertzian (II), see [73]) and then abruptly changes to a plastically dominated behavior (III). Finally, at large strains, favored by high *E/σ* values, a fully plastic regime can be observed (IV) where *C** becomes constant and from which Tabor's proposal of a *C**=const. might originate from. The profile can be split and expressed as an empiric function:

$$C^*(\mu) = \begin{cases} 1 \quad , & \mu = 0.5 \qquad (I) \\ 2.12 \cdot \ln(\mu + 0.5)^{1.25} + 1, & 0.5 < \mu < 1.45 \qquad (II) \\ 0.55 \cdot \ln(\mu) + 2.08, & 1.45 \leq \mu < 4.5 \qquad (III) \\ 2.91 \quad , & x \geq 4.5 \qquad (IV) \end{cases} \qquad \text{equation (13).}$$

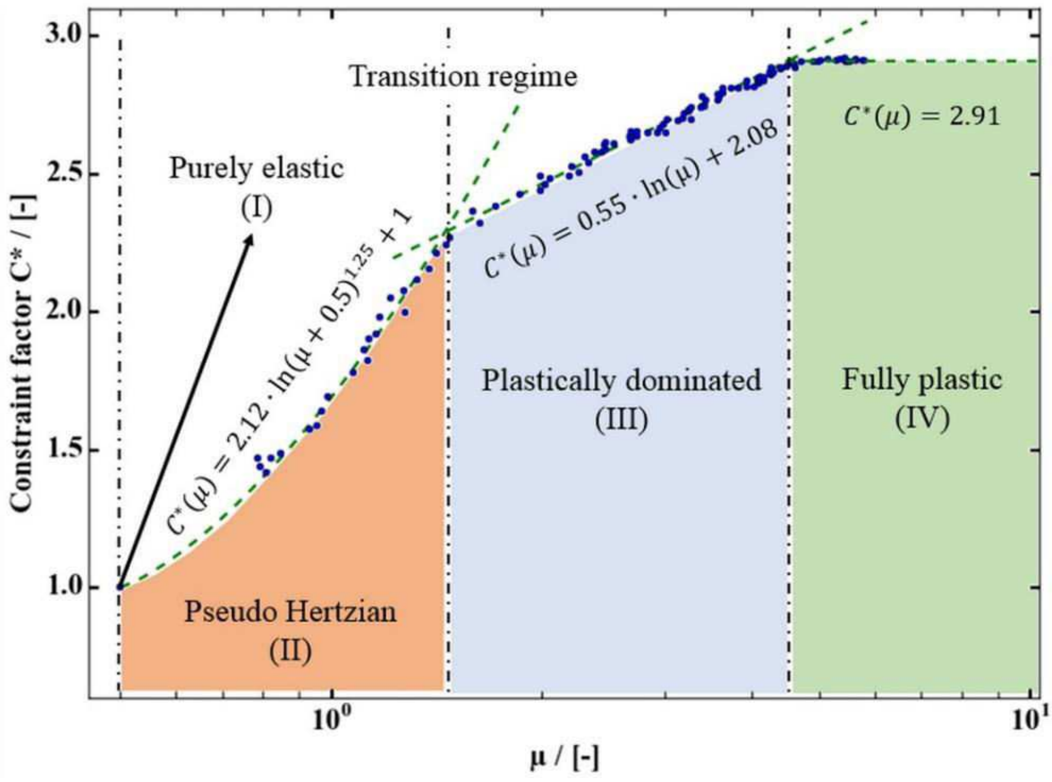

Figure 6. Experimental dependency of the constraint factor *C** on μ (blue circles) determined by the comparison of uniaxial and spherical indentation flow curves on NC Ni. Fitting functions (dashed line) according to equation (13) for the four different observable deformation regimes.

By this function, one can determine the constraint factor profile for each indent, since μ can directly be evaluated from the nanoindentation device. Studies showed that for materials with similar work hardening behavior and frictional properties, the same function will be applicable [32,73]. The used materials (NC Ni, UFG Cu, UFG Cr, UFW W) will fulfil these qualifications. Figure 7a-d shows the comparison of flow curves obtained by pillar compression tests (green solid line) and spherical indentation experiments with variable *C** (blue triangles). Additionally, stress-strain curves using the original approach of Tabor with a constant constraint factor of 2.8 [21] are imprinted (red crosses), which clearly underestimate the yield level and overestimate the work-hardening of the materials. Obviously, the match in Figure 7a is self-explanatory since these curves were used to obtain the function for *C**. However, also Figures 7b-d show excellent agreement, which make the assumptions seem justified once materials with reasonably similar mechanical character are tested. Interestingly, also instabilities during compression, as occurrent for UFG W in Fig 7d were individual grains yield, are picked up in spherical indentation experiments. Notably, the difference between the red and blue curves is more significant for materials where E/σ is low. Here values for *C** will refer to low values of μ and consequently noticeably deviate from the constant value of 2.8 (see Figure 6). Tabor might have unintentionally avoided this problem, since he tested coarse grained mild steel and copper that both feature high values of *E/σ* > 400. Additionally, one must not forget that Tabor calculated the hardness by dividing the load by the area of the residual imprint, which will slightly deviate from the projected area at maximum load.

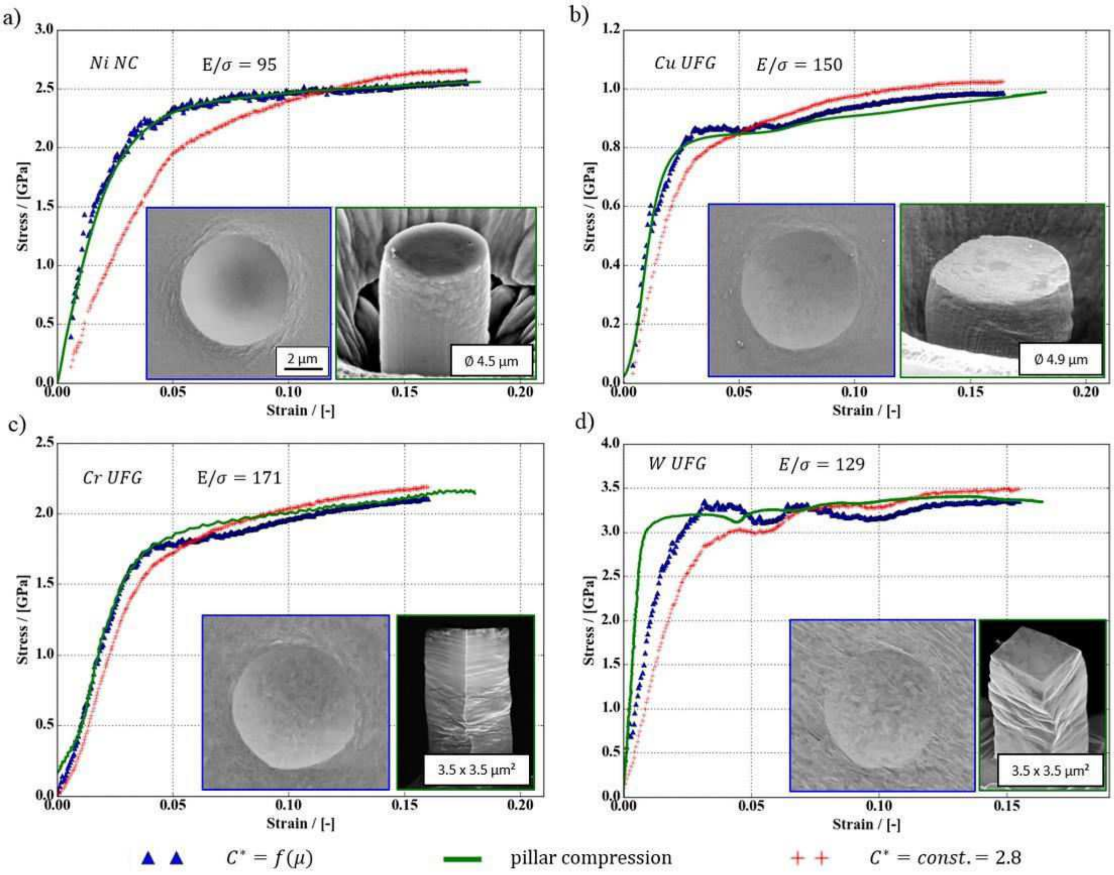

Figure 7. Comparison between uniaxial micropillar compression tests (green solid line) and spherical indentation flow curves using a constant constraint factor of 2.8 (red crosses) and a variable constraint-factor (blue triangles) for NC Ni, UFG W, UFG Cr and UFG Cu. Insets show SEM micrographs of spherical impressions (scale-bar of a) applies to all indentations) and post-mortem pillars of the corresponding material.

D - Summary and conclusion

Few experimental techniques feature the enormous efficiency and capability for the substantial characterization of materials as is the case for spherical nanoindentation. Despite these outstanding perspectives current instrumented indentation methods do not have the precision which is required for excellence in material science and quality management. Within this study we present a wide variety of significant advances which should be adapted to existing nanoindentation protocols.

i. The calibration of spherical tips has been reinvestigated. Based on the geometry of a sphere, a novel non-linear function type is suggested to calculate the contact area in dependence of the contact depth, which allows to account for deviant sphericity also at large displacements. The accuracy of the introduced highly stable fitting procedure was validated on a broad spectrum of materials with Young's moduli ranging from 35 GPa to 400 GPa. This approach also impedes the problem of signal noise which occurs if the stiffness is used to back-calculate the current contact area function.

ii. Adequately controlling the strain-rate is challenging for spherical indentation since the strain will be influenced by tip shape imperfections and an assumed constant radius is a deficient approximation for rate-dependent modern high-performance materials. Tuning the PID-parameters of the used nanoindentation device allows to exactly achieve set strain-rates and eliminates impacts of the actual tip shape. Comparison to constant load-rate and constant strain-rate tests used for pyramidal tips show that these strain-rate profiles would significantly falsify the appearance of hardness curves.

iii. Performing experiments with constant strain-rates shows that materials with refined microstructures, ensuring the instantaneous sampling of a representative volume, do not feature a tip size effect and exhibit formidable reproducibility.

iv. Properly controlling the strain-rate opens the door to extract the strain-rate sensitivity either by constant strain-rate experiments or by spherical nanoindentation jump tests. Values are in excellent agreement with data obtained by sharp tip indentation and do not show a strain dependence.

v. A novel approach to account for a physically realistic varying constraint factor (C^*) considering yield stress, Young's modulus and indentation strain is presented, using the ratio of the unloading and loading slope (μ) of the load/contact displacement curves. Matching flow curves from uniaxial pillar compression and spherical indentation on NC Ni leads to an empiric relation $C^*=\mathrm{f}(\mu)$ which is in accordance to previous FEM studies.

vi. Using the presented refinements leads to excellent agreement of flow curves obtained by uniaxial compression and spherical indentation for the tested materials NC Ni UFG Cu, UFG Cr and UFG W.

The presented advancements of spherical indentation testing and analysis will prospectively expand the possibilities of this technique. Apparently, a reasonable tip shape function and strain-rate controlled experiments contribute to a significantly improved utility of indentation tests. However, particularly the conversion from hardness to representative stress must be used with caution, as it could not yet be thoroughly physically explained. The application is restricted to materials with small internal length-scales and similar mechanical character to avoid tip size-effects and vastly different work hardening behavior. Besides, the properties of the tribological system of indenter tip and sample must be consistent. Consideration of these influences to extend the feasibility of the approach and supporting the transformation from µ' to µ by FEM studies will be subjects of future studies.

D – Acknowledgements

Funding by the Austrian Federal Government (837900), in particular from the Bundesministerium für Verkehr, Innovationund Technologie and the Bundesministerium für Wirtschaft, Familie und Jugend, represented by Österreichische Forschungsförderungsgesellschaft mbH and the Styrian and Tyrolean Provincial Government, represented by Steirische Wirtschaftsförderungsgesellschaft mbH and Standortagentur Tirol, within the framework of the COMET Funding Programme (MPPE, A7.19) is appreciated. Furthermore, parts of this work were also funded by the Austrian Science Fund (FWF) via the project P25325-N20.

D – Appendix

1.

The conventional definition of strain from the classical Tabor approach and the novel definition of Kalidindi and Pathak are closely related. Both are dependent on the current opening angle θ (see Figure A1).

Tabor related definition	Definition by Kalidindi and Pathak
$\varepsilon_i = \frac{a_c}{R}$	$\varepsilon_i = \frac{4 \cdot h}{3 \cdot \pi \cdot a_c}$
$A_c = {a_c}^2 \cdot \pi$	$\frac{h}{a_c} = \cot\theta'$
$a_c = h_c \cdot \tan\theta$	$\frac{\cot\theta'}{\cot\theta} = \frac{h}{h_c}$
$R^2 = {a_c}^2 + (R - h_c)^2$	$\cot\theta' = \frac{h}{h_c} \cdot \cot\theta$
$R = \frac{{a_c}^2 + {h_c}^2}{2 \cdot h_c}$	$\varepsilon_i = \frac{4 \cdot h \cdot \cot\theta}{3 \cdot \pi \cdot h_c}$
$\frac{a_c}{R} = \frac{2 \cdot h_c \cdot a_c}{{a_c}^2 + {h_c}^2} = \frac{2 \cdot \cot\theta}{1 + \cot^2\theta}$	
$\varepsilon_i = f(\cot\theta)$	$\varepsilon_i = f(\cot\theta)$

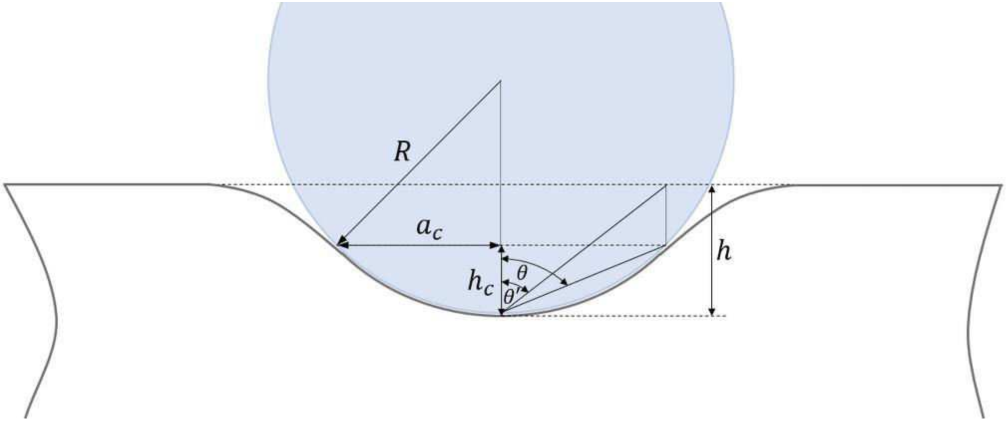

Figure A1. Schematic loading of a spherical tip with radius R.

2.

The ratio of unloading slope, which is the contact stiffness *S*, and loading slope n_L, referred to as μ in this study, in indentation experiments is of interest to identify the character of plastic deformation, since it is directly related to the ratio of induced plastic and elastic work during indentation. The subsequent derivation shows that μ is in directly related to the elastic (*E**) and plastic (*H*) properties as well as to the indentation strain ε_i which scales with cot Θ (see appendix A).

$$\mu = \frac{S}{n_L}$$

$$S = \frac{2 \cdot E \cdot \sqrt{A_c}}{\sqrt{\pi}} = 2 \cdot E^* \cdot h_c \cdot \tan\theta$$

$$P = H \cdot {a_c}^2 \cdot \pi = H \cdot {h_c}^2 \cdot \tan^2\theta \cdot \pi$$

$$n_L = \frac{dP}{dh_c} = 2 \cdot H \cdot h_c \cdot \tan^2\theta \cdot \pi$$

$$\mu = \frac{S}{n_L} = \frac{2 \cdot E^* \cdot h_c \cdot \tan\theta}{2 \cdot H \cdot h_c \cdot \tan^2\theta \cdot \pi} = \frac{E^*}{H} \cdot \frac{\cot\theta}{\pi}$$

Due to elemental elastic contact mechanics based on Hertz, the contact depth h_c and elastic sink-in depth h_s are related to each other by:

$$h_c = h_s = \frac{1}{2} \cdot h$$

During elastic deformation, the unloading slope is equivalent to the loading slope, hence the slope of the contact loading is 0.5. Experiments with a 50 µm radius tip on fused quartz, where no plastic deformation is expected, demonstrates this behavior (Figure B1 a). On GaAs, one notes that until the pop-in event there is only elastic deformation, showing μ on a level of 0.5, which instantaneously increases after the pop-in (Figure B1 b). For Al, tested with a 5 µm tip, plasticity is observable immediately (Figure B1 c). Contrarily, for sharp self-similar tips and isotropic materials, µ shows a horizontal profile over displacement as H, E^* and cot Θ will remain constant in the self-similar indentation process. Varying the opening angle will shift the profiles in parallel (Figure B1 d).

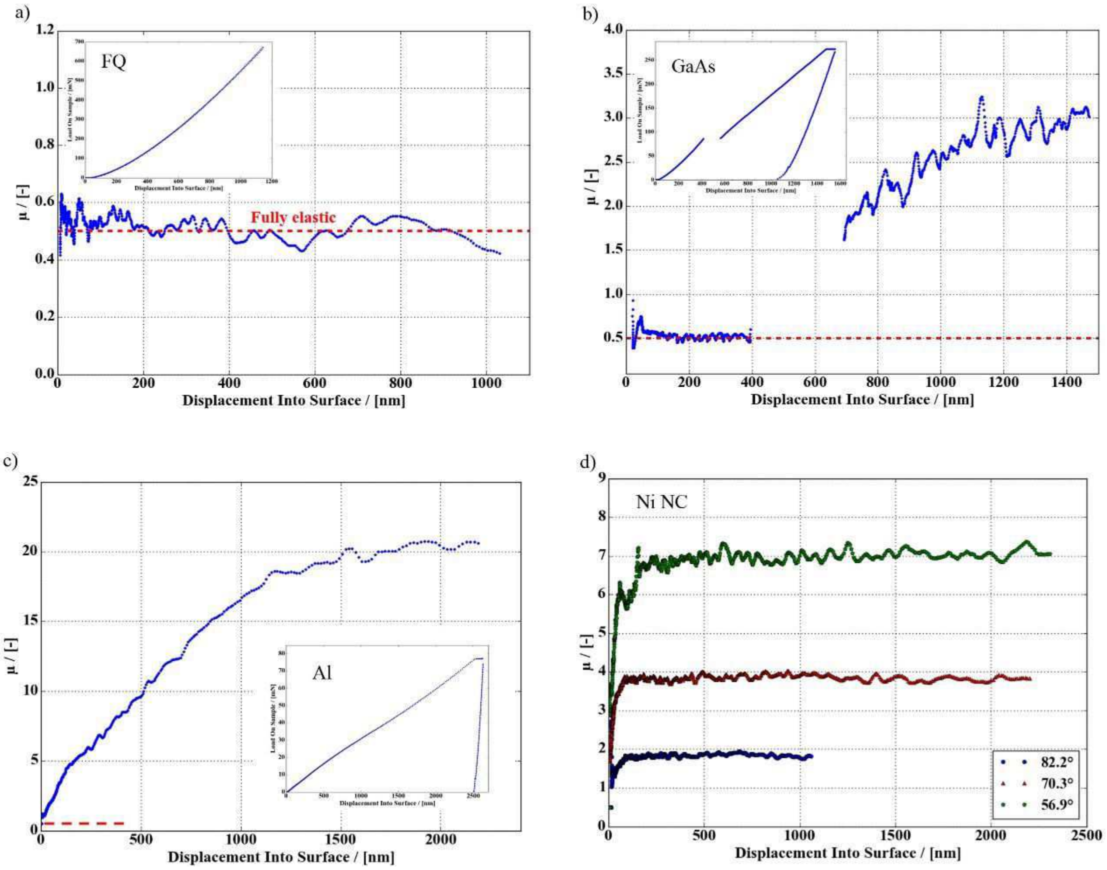

Figure B1. a) Profile of µ over displacement. a) For a purely elastic indent on FQ with a 60 µm sphere μ is horizontal at a level of 0.5. Loading and unloading curve in the inset are coincidence. b) GaAs clearly demonstrates the transition from elastic to plastic deformation after the pop-in event. c) A spherical indent on Al shows plasticity instantaneously. d) μ is constant over displacement for self-similar pyramidal tips. A variation of the opening angle leads to a shift of the value of μ.

D - References

[1] J.B. Pethica, R. Hutchings, W.C. Oliver, Hardness measurement at penetration depths as small as 20 nm, Philos. Mag. A. 48 (1983) 593–606. doi:10.1080/01418618308234914.

[2] W.C. Oliver, G.M. Pharr, An improved technique for determining hardness and elastic modulus using load and displacement sensing indentation experiments, J. Mater. Res. 7 (1992) 1564–1583. doi:10.1557/JMR.1992.1564.

[3] N.A. Stilwell, D. Tabor, Elastic Recovery of Conical Indentations, Proc. Phys. Soc. 78 (1961) 169–179. doi:10.1088/0370-1328/78/2/302.

[4] I. Sneddon, The relation between load and penetration in the axisymmetric Boussinesq problem for a punch of arbitrary profile, Int. J. Eng. Sci. 3 (1965) 47–57. doi:10.1016/0020-7225(65)90019-4.

[5] J.L. Loubet, J.M. Georges, O. Marchesini, G. Meille, Vickers Indentation Curves of Magnesium Oxide (MgO), J. Tribol. 106 (1984) 43–48. doi:10.1115/1.3260865.

[6] M.F. Doerner, W.D. Nix, A method for interpreting the data from depth-sensing indentation instruments, J. Mater. Res. 1 (1986) 601–609. doi:10.1557/JMR.1986.0601.

[7] A.C. Fischer-Cripps, Nanoindentation, Springer New York, 2002. doi:10.1007/978-1-4419-9872-9.

[8] J.B. Pethica, W.C. Oliver, Mechanical Properties of Nanometre Volumes of Material: use of the Elastic Response of Small Area Indentations, MRS Proc. 130 (1988) 13–23. doi:10.1557/PROC-130-13.

[9] S.A.S. Asif, K.J. Wahl, R.J. Colton, Nanoindentation and contact stiffness measurement using force modulation with a capacitive load-displacement transducer, Rev. Sci. Instrum. 70 (1999) 2408–2413. doi:10.1063/1.1149769.

[10] X. Li, B. Bhushan, A review of nanoindentation continuous stiffness measurement technique and its applications, Mater. Charact. 48 (2002) 11–36. doi:10.1016/S1044-5803(02)00192-4.

[11] W.C. Oliver, G.M. Pharr, Measurement of hardness and elastic modulus by instrumented indentation: Advances in understanding and refinements to methodology, J. Mater. Res. 19 (2004) 3–20. doi:10.1557/jmr.2004.19.1.3.

[12] V. Maier, B. Merle, M. Göken, K. Durst, An improved long-term nanoindentation creep testing approach for studying the local deformation processes in nanocrystalline metals at room and elevated temperatures, J. Mater. Res. 28 (2013) 1177–1188. doi:10.1557/jmr.2013.39.

[13] K.L. Johnson, The correlation of indentation experiments, J. Mech. Phys. Solids. 18 (1970) 115–126. doi:10.1016/0022-5096(70)90029-3.

[14] W.D. Nix, H. Gao, Indentation size effects in crystalline materials: A law for strain gradient plasticity, J. Mech. Phys. Solids. 46 (1998) 411–425. doi:10.1016/S0022-5096(97)00086-0.

[15] G.M. Pharr, J.H. Strader, W.C. Oliver, Critical issues in making small-depth mechanical property measurements by nanoindentation with continuous stiffness measurement, J. Mater. Res. 24 (2009) 653–666. doi:10.1557/jmr.2009.0096.

[16] S. Qu, Y. Huang, G.M. Pharr, The indentation size effect in the spherical indentation of iridium : A study via the conventional theory of mechanism-based strain gradient plasticity, Int. J. Plast. 22 (2006) 1265–1286. doi:10.1016/j.ijplas.2005.07.008.

[17] K. Durst, M. Göken, G.M. Pharr, Indentation size effect in spherical and pyramidal indentations, J. Phys. D. Appl. Phys. 41 (2008) 1–5. doi:10.1088/0022-3727/41/7/074005.

[18] J.G. Swadener, E.P. George, G.M. Pharr, The correlation of the indentation size effect measured with indenters of various shapes, J. Mech. Phys. Solids. 50 (2002) 681–694. doi:10.1016/S0022-5096(01)00103-X.

[19] L. Prandtl, Über die Härte plastischer Körper, Nachrichten von Der Gesellschaft Der Wissenschaften Zu Göttingen. (1920) 74–85. doi:10.1007/978-3-662-11836-8_7.

[20] A.G. Atkins, D. Tabor, Plastic indentation in metals with cones, J. Mech. Phys. Solids. 13 (1965) 149–164. doi:10.1016/0022-5096(65)90018-9.

[21] D. Tabor, The Hardness of Metals, OUP Oxford, 1951.

[22] J.L. Bucaille, S. Stauss, E. Felder, J. Michler, Determination of plastic properties of metals by instrumented indentation using different sharp indenters, Acta Mater. 51 (2003) 1663–1678. doi:10.1016/S1359-6454(02)00568-2.

[23] S. Shim, J. Jang, G.M. Pharr, Extraction of flow properties of single-crystal silicon carbide by nanoindentation and finite-element simulation, Acta Mater. 56 (2008) 3824–3832. doi:10.1016/j.actamat.2008.04.013.

[24] A. Leitner, V. Maier-Kiener, D. Kiener, Extraction of Flow Behavior and Hall–Petch Parameters Using a Nanoindentation Multiple Sharp Tip Approach, Adv. Eng. Mater. 19 (2017) 1–9. doi:10.1002/adem.201600669.

[25] Y.-T. Cheng, C.-M. Cheng, Can stress-strain relationships be obtained from indentation curves using conical and pyramidal indenters?, J. Mater. Res. 14 (1999) 3493–3496. doi:10.1557/JMR.1999.0472.

[26] J.S. Field, M.V. Swain, A Simple Predictive Model for Spherical Indentation, J. Mater. Res. 8 (1993) 297–306. doi:10.1557/JMR.1993.0297.

[27] M.D. Uchic, D.M. Dimiduk, J.N. Florando, W.D. Nix, Sample Dimensions Influence Strength and Crystal Plasticity, Science (80-.). 305 (2004) 986–989. doi:10.1126/science.1098993.

[28] S. Basu, A. Moseson, M.W. Barsoum, On the determination of spherical nanoindentation stress-strain curves, J. Mater. Res. 21 (2006) 2628–2637. doi:10.1557/jmr.2006.0324.

[29] S.R. Kalidindi, S. Pathak, Determination of the effective zero-point and the extraction of spherical nanoindentation stress – strain curves, Acta Mater. 56 (2008) 3523–3532. doi:10.1016/j.actamat.2008.03.036.

[30] S. Pathak, J. Shaffer, S.R. Kalidindi, Determination of an effective zero-point and extraction of indentation stress – strain curves without the continuous stiffness measurement signal, Scr. Mater. 60 (2009) 439–442. doi:10.1016/j.scriptamat.2008.11.028.

[31] S. Pathak, S.R. Kalidindi, Spherical nanoindentation stress-strain curves, Mater. Sci. Eng. R Reports. 91 (2015) 1–36. doi:10.1016/j.mser.2015.02.001.

[32] S.-D. Mesarovic, N.A. Fleck, Spherical indentation of elastic-plastic solids, Proc. R. Soc. London A Math. Phys. Eng. Sci. 455 (1999) 2707–2728. doi:10.1098/rspa.1999.0423.

[33] A.J. Bushby, N.M. Jennett, Determining the Area Function of Spherical Indenters for Nanoindentation, Mater. Res. Soc. Symp. Proc. 649 (2000) 1–6. doi:10.1557/PROC-649-Q7.17.

[34] A.J. Bushby, Nanoindentation using spherical indenters, Nondestruct. Test. Eval. 17 (2001) 213–234. doi:10.1080/10589750108953112.

[35] L. Hong, N. Fujisawa, M. V Swain, Elastic modulus and stress – strain response of human enamel by nano-indentation, Biomaterials. 27 (2006) 4388–4398. doi:10.1016/j.biomaterials.2006.03.045.

[36] D.K. Patel, S.R. Kalidindi, Correlation of spherical nanoindentation stress-strain curves to simple compression stress-strain curves for elastic-plastic isotropic materials using finite element models, Acta Mater. 112 (2016) 295–302. doi:10.1016/j.actamat.2016.04.034.

[37] P. Feldner, B. Merle, M. Göken, Determination of the strain-rate sensitivity of ultrafine-grained materials by spherical nanoindentation, J. Mater. Res. 49 (2017) 1466–1473. doi:10.1557/jmr.2017.69.

[38] B.-W. Choi, D.-H. Seo, J.-Y. Yoo, J. Jang, Predicting macroscopic plastic flow of high-performance, dual-phase steel through spherical nanoindentation on each microphase, J. Mater. Res. 24 (2009) 816–822. doi:10.1557/jmr.2009.0109.

[39] E. Meyer, Untersuchungen über Härteprüfung und Härte, Zeitschrift Verein Dtsch. Ingenieure. 52 (1909).

[40] Y. Tirupataiah, G. Sundararajan, On the Constraint Factor Associated with the Indentation of Work-Hardening Materials with a Spherical Ball, Metall. Trans. A. 22A (1991) 2375–2384. doi:10.1007/BF02665003.

[41] J.L. Hay, W.C. Oliver, A. Bolshakov, G.M. Pharr, Using the ratio of loading slope and elastic stiffness to predict pile-up and constraint factor during indentation, MRS Proc. 522 (1998) 101–106. doi:10.1557/PROC-522-101.

[42] X. Chen, J.J. Vlassak, Numerical study on the measurement of thin film mechanical properties by means of nanoindentation, J. Mater. Res. 16 (2001) 2974–2982. doi:10.1557/JMR.2001.0408.

[43] A. Clausner, F. Richter, Determination of yield stress from nano-indentation experiments, Eur. J. Mech. - A/Solids. 51 (2015) 11–20. doi:10.1016/j.euromechsol.2014.11.008.

[44] M. Mata, O. Casals, J. Alcalá, The plastic zone size in indentation experiments: The analogy with the expansion of a spherical cavity, Int. J. Solids Struct. 43 (2006) 5994–6013. doi:10.1016/j.ijsolstr.2005.07.002.

[45] M. Rodríguez, J.M. Molina-Aldareguia, C. González, J. Llorca, Determination of the mechanical properties of amorphous materials through instrumented nanoindentation, Acta Mater. 60 (2012) 3953–3964. doi:10.1016/j.actamat.2012.03.027.

[46] S. Kang, Y. Kim, K. Kim, J. Kim, D. Kwon, Extended expanding cavity model for measurement of flow properties using instrumented spherical indentation, Int. J. Plast. 49 (2013) 1–15. doi:10.1016/j.ijplas.2013.02.014.

[47] B. Merle, V. Maier-Kiener, G.M. Pharr, Influence of modulus-to-hardness ratio and harmonic parameters on continuous stiffness measurement during nanoindentation, Acta Mater. 134 (2017) 167–176. doi:10.1016/j.actamat.2017.05.036.

[48] A. Leitner, V. Maier-Kiener, D. Kiener, Dynamic nanoindentation testing: Is there an influence on a material's hardness?, Mater. Res. Lett. 5 (2017) 486–493. doi:10.1080/21663831.2017.1331384.

[49] V. Maier, K. Durst, J. Mueller, B. Backes, H.W. Höppel, M. Göken, Nanoindentation strain-rate jump tests for determining the local strain-rate sensitivity in nanocrystalline Ni and ultrafine-grained Al, J. Mater. Res. 26 (2011) 1421–1430. doi:10.1557/jmr.2011.156.

[50] R. Fritz, D. Wimler, A. Leitner, V. Maier-Kiener, D. Kiener, Dominating Deformation Mechanisms in Ultrafine-grained Chromium across Length Scales and Temperatures, Acta

Mater. 140C (2017) 176–187. doi:10.1016/j.actamat.2017.08.043.

[51] R. Fritz, A. Leitner, V. Maier-Kiener, R. Pippan, D. Kiener, Interface-dominated Strength Scaling Behaviour in Ultrafine-grained Tungsten Samples, Submitted. (2017).

[52] M.D. Uchic, D.M. Dimiduk, A methodology to investigate size scale effects in crystalline plasticity using uniaxial compression testing, Mater. Sci. Eng. A. 400–401 (2005) 268–278. doi:10.1016/j.msea.2005.03.082.

[53] D. Jang, J.R. Greer, Size-induced weakening and grain boundary-assisted deformation in 60 nm grained Ni nanopillars, Scr. Mater. 64 (2011) 77–80. doi:10.1016/j.scriptamat.2010.09.010.

[54] M.W. Kapp, A. Hohenwarter, S. Wurster, B. Yang, R. Pippan, Anisotropic deformation characteristics of an ultrafine- and nanolamellar pearlitic steel, Acta Mater. 106 (2016) 239–248. doi:10.1016/j.actamat.2015.12.037.

[55] R. Fritz, V. Maier-Kiener, D. Lutz, D. Kiener, Interplay between sample size and grain size: Single crystalline vs. ultrafine-grained chromium micropillars, Mater. Sci. Eng. A. 674 (2016) 626–633. doi:10.1016/j.msea.2016.08.015.

[56] T. Hausöl, H.W. Höppel, M. Göken, Tailoring materials properties of UFG aluminium alloys by accumulative roll bonded sandwich-like sheets, J. Mater. Sci. 45 (2010) 4733–4738. doi:10.1007/s10853-010-4678-y.

[57] H.S. Leipner, D. Lorenz, A. Zeckzer, H. Lei, P. Grau, Nanoindentation Pop-In Effect in Semiconductors, Phys. B Condens. Matter. 308–310 (2001) 446–449. doi:10.1016/S0921-4526(01)00718-9.

[58] S.A.S. Asif, J.B. Pethica, Nanoindentation creep of single-crystal tungsten and gallium arsenide, Philos. Mag. A. 76 (1997) 1105–1118. doi:10.1080/01418619708214217.

[59] E.O. Hall, The Deformation and Ageing of Mild Steel: Discussion of Results, Proc. Phys. Soc. Sect. B. 64 (1951) 747. doi:10.1088/0370-1301/64/9/303.

[60] N.J. Petch, The cleavage strength of polycrystals, J. Iron Steel Inst. 174 (1953) 25–28.

[61] X. Li, K. Lu, Playing with defects in metals, Nat. Mater. 16 (2017) 700–701. doi:10.1038/nmat4929.

[62] L. Lu, X. Chen, X. Huang, K. Lu, Revealing the Maximum Strength in Nanotwinned Copper, Science (80-.). 323 (2009) 607–610. doi:10.1126/science.1167641.

[63] B. Merle, V. Maier, M. Göken, K. Durst, Experimental determination of the effective indenter shape and ε-factor for nanoindentation by continuously measuring the unloading stiffness, J. Mater. Res. 27 (2012) 214–221. doi:10.1557/jmr.2011.245.

[64] D.W. Marquardt, An Algorithm for Least-Squares Estimation of Nonlinear Parameters, J. Soc. Ind. Appl. Math. 11 (1963) 431–441. doi:10.1137/0111030.

[65] K. Levenberg, A method for the solution of certain non-linear problems in least squares, Q. Appl. Math. 2 (1944) 164–168. doi:10.1090/qam/10666.

[66] H. Hertz, Über die Berührung fester elastischer Körper, J. Für Die Reine Und Angew. Math. 92 (1882) 156–171. doi:10.1515/crll.1882.92.156.

[67] H. Majjad, S. Basrour, P. Delobelle, M. Schmidt, Dynamic determination of Young's modulus of electroplated nickel used in LIGA technique, Sensors Actuators, A Phys. 74 (1999) 148–151. doi:10.1016/S0924-4247(98)00306-9.

[68] H.E. Boyer, T.L. Gall, eds., Metals Handbook, American Society for Metals, 1985.

[69] B.N. Lucas, W.C. Oliver, Indentation power-law creep of high-purity indium, Metall. Mater. Trans. A. 30 (1999) 601–610. doi:10.1007/s11661-999-0051-7.

[70] E.W. Hart, Theory of the tensile test, Acta Metall. 15 (1967) 351–355. doi:10.1016/0001-6160(67)90211-8.

[71] Q. Wei, S. Cheng, K.T. Ramesh, E. Ma, Effect of nanocrystalline and ultrafine grain sizes on the strain rate sensitivity and activation volume: fcc versus bcc metals, Mater. Sci. Eng. A. 381 (2004) 71–79. doi:10.1016/j.msea.2004.03.064.

[72] ISO, TR 29381 Metallic materials - Measurement of mechanical properties by an instrumented indentation test - Indentation tensile properties, 2008.

[73] Y.J. Park, G.M. Pharr, Nanoindentation with spherical indenters : finite element studies of deformation in the elastic – plastic transition regime, Thin Solid Films. 448 (2004) 246–250. doi:10.1016/S0040-6090.